Title
CHAOS AND TURBULENCE IN AN ELECTRON-HOLE PLASMA IN GERMANIUM

Author
Held, G.A.

Publication Date
1985-11-01

Lawrence Berkeley Laboratory
UNIVERSITY OF CALIFORNIA

Materials & Molecular Research Division

CHAOS AND TURBULENCE IN AN ELECTRON-HOLE PLASMA IN GERMANIUM

G.A. Held
(Ph.D. Thesis)

November 1985

Prepared for the U.S. Department of Energy under Contract DE-AC03-76SF00098

DISCLAIMER

LBL-20626

CHAOS AND TURBULENCE IN AN ELECTRON-HOLE PLASMA IN GERMANIUM

Glenn Allen Held

Ph.D. Thesis

November 1985

Materials and Molecular Research Division
Lawrence Berkeley Laboratory
and
Department of Physics
University of California
Berkeley, CA 94720

This work was supported by the Director, Office of Energy Research, Office of Basic Energy Sciences, Materials Sciences Division of the U.S. Department of Energy under Contract No. DE-AC03-76SF00098.

for Ellen

Table of Contents

ABSTRACT

Spontaneous current oscillations in an electron-hole plasma in germanium in parallel dc electric and magnetic fields are known to be the result of an unstable helical density wave. We find that when this instability is excited by an increasing electric field, there is a transition to turbulence similar to that observed in fluids. It is demonstrated that this turbulent behavior is chaotic; the observed dynamics include both period doubling and quasiperiodic transitions to chaos. This represents the first clear evidence of a universal transition to low-dimensional chaos in any plasma.

A number of techniques are employed to characterize the transitions to chaos. Analog techniques include the measurement of power spectra and the generation of real-time phase portraits, return maps, and bifurcation diagrams. Fractal dimensions, a quantitative measure of chaos, are computed from digitized time series of the total plasma current.

Following a quasiperiodic route, the resulting chaotic state is found to be characterized by a strange attractor of fractal dimension between 2 and 3. By fabricating probe contacts along the length of the crystal, we study the spatial structure of these instabilities, finding that these "weakly" turbulent instabilities correspond to temporally chaotic, yet essentially spatially coherent plasma density waves.

However, when more strongly excited, these plasma density waves

undergo a partial loss of spatial coherence. The onset of the loss of spatial coherence is characterized by a sudden jump in the dimension of the attractor -- from less than three for spatially coherent states to an indeterminately large value (>8) after the onset of spatial disorder.

Experiments on the coupling of a periodic instability of frequency f_1 to an external perturbation of frequency f_2 are reported. For weak perturbations, the result is a quasiperiodic state. As the amplitude of the external excitation is increased, frequency lockings are observed. When the ratio f_2/f_1 is fixed at an irrational number, a quasiperiodic transition to chaos is observed. This transition is approximately modeled by maps of the invariant circle.

Finally, a rate-equation model, which includes nonlinear coupling between unstable and damped plasma density waves is presented.

CHAPTER I. INTRODUCTION

Spontaneous current oscillations in an electron-hole plasma in Ge in parallel dc electric and magnetic fields are known to be the result of an unstable helical density wave.[1] When this instability is strongly excited by an increasing electric field, there is a transition to turbulence similar to that observed in fluids.[2,3] The present work demonstrates that this turbulent behavior is chaotic; the observed dynamics include period doubling and quasiperiodic transitions to low-dimensional chaos, frequency locking, and a partial loss of spatial coherence, indicating the spatial breakdown of the helical density wave. The possibility that plasmas could exhibit chaotic behavior has been discussed theoretically.[4] This work provides the first evidence of a period doubling and a quasiperiodic transition to chaos in any plasma.

The first three sections of this chapter comprise a discussion of the basic concepts associated with chaotic dynamics. The fourth section is a review of the linear theory of helical instabilities in semiconductor plasmas, applicable prior to the onset of turbulence.

1.1. Chaotic Dynamics

The dynamics of a nonlinear physical system may appear random or noisy when, in fact, the system is exhibiting chaotic behavior involving only a few degrees of freedom.[2] The behavior of such a system is most easily discussed in terms of its dynamics in some phase space. The coordinates of the

phase space may be any set of variables which, when taken together, uniquely identify the state of the system; the temporal evolution of the system thus corresponds to motion along a trajectory in phase space.

A system is chaotic when it evolves in phase space along trajectories which satisfy the property that nearby trajectories diverge from one another exponentially in time. The rates at which these trajectories diverge (or converge), measured along some locally orthogonal axes, are known as Lyapunov exponents.[5] Chaotic behavior is characterized by at least one positive Lyapunov exponent.

A dissipative system occupies a volume of phase space which contracts as a function of time; trajectories converge to a limit set referred to as an attractor. If the system is chaotic, then this limit set is known as a strange attractor.[6,7] Typically, a strange attractor consists of an infinite number of folded surfaces contained within a bounded region of phase space. Trajectories constrained to move along such an attractor simultaneously diverge from one another and remain within a bounded volume of phase space. A Poincaré section (i.e., a cross section of the attractor) will often reveal the multiple foldings and rich structure which typify strange attractors. An example is shown in figure 1.1. This figure shows a cross sectional view of the chaotic attractor which results from solving Duffing's equation,[8] an ordinary differential equation which is known to exhibit chaos.

The dimension of a strange attractor is fractional.[9] For example, an attractor which consists of an infinite number of 2-dimensional surfaces

XBB 848-5684

Figure 1.1. Poincaré section of Duffing's equation,

$$\ddot{x} - ax + bx^3 = -g\dot{x} + F\cos\omega t \ ,$$

where $a = 1.0$, $b = 10.0$, $g = 0.12$, $F = 0.56$, and $\omega = 0.93$. The vertical and horizontal axes refer to $\dot{x}$ and x respectively, plotted whenever $(\omega t)_{\mathrm{mod}2\pi} = 0$. This figure was provided by J. P. Crutchfield.

confined within a finite 3-dimensional volume of phase space (such as the attractor whose Poincaré section is shown in figure 1.1) would have a fractal dimension between two and three; the precise value would depend on the density of these surfaces. The fractal dimension is an approximate measure of the number of degrees of freedom needed to characterize the behavior of the system. If the fractal dimension of an attractor is less than three, then three coordinates (using an appropriate set of basis vectors) will uniquely identify the state of the system at any instant of time. In this sense chaotic behavior is low-dimensional and therefore similar to regular motion (where the number of degrees of freedom is equal to the number of incommensurate frequencies).

However, in contrast with regular motion, nearby trajectories confined to a strange attractor will diverge exponentially in time. Therefore, any uncertainty in the characterization of the system will also grow exponentially with time. If one could "exactly" measure three independent phase space coordinates at one instant of time (still assuming an attractor of fractal dimension less than three) then the subsequent evolution of the system would be completely determined. However, an infinitesimal uncertainty in these three coordinates will grow exponentially in time, resulting in what is often referred to as "sensitive dependence on initial conditions."[7] This sensitive dependence assures that the near recurrence of a particular state of the system (characterized by the three coordinates) will not result in near periodicity and, consequently, the power spectra of measurable quantities will be broadband;[10] any predictions concerning these quantities must be statistical.

1.2. Transitions to Chaos

Experience indicates that the transition from regular to chaotic motion typically follows one of several "universal" routes.[2,11] These include the period doubling, quasiperiodic, frequency locking and intermittent routes to chaos. Perhaps the best known of these is the period doubling transition to chaos. In this scenario, an initially periodic system follows a cascade of period doublings to chaos as a control parameter λ is increased. The logistic equation

$$x_{n+1} = \lambda\, x_n\, (1-x_n) \tag{1.1}$$

is an example of a simple, iterative equation which follows a period doubling transition to chaos as λ is increased. A bifurcation diagram, or plot of λ vs. $\{ x_n \}$, where $\{ x_n \}$ is the set of steady-state iterates (which comprise the attractor) is shown in figure 1.2. The cascade of period doublings, as well as noise-free periodic windows within the chaotic regime may be observed in such a diagram. Feigenbaum[12] has shown that the value of the control parameter at the onset of period 2^n ,λ_n, scales as $\lambda_c - \lambda_n \propto \delta^{-n}$ for large n, where λ_c is the value of the control parameter at the onset of chaos and $\delta = 4.669...$ is a universal constant. Other universal constants are known to characterize spacings between successive iterates[12], spectral power density[13] and the effects of additive noise.[14] Metropolis, Stein, and Stein[15] demonstrated that these windows must occur in the same, specific sequence for all 1-dimensional mappings with a single maximum.

While some theoretical work has been done on the intermittent,[16,17] frequency locking,[18] and quasiperiodic transitions to chaos, none of these scenarios is understood as completely as the period doubling route. The quasiperiodic transition to chaos -- the emergence of two or more incommensurate frequencies followed by the onset of chaos -- is perhaps the least well understood. The only detailed theoretical treatment of this transition necessarily assumes that the ratio of the two incommensurate frequencies is equal to the golden mean ($\approx$1.62).[19] This is seldom observed experimentally. In fact, experimentally, a hybrid of these universal transitions (such as a quasiperiodic bifurcation followed by a period doubling cascade of one of the incommensurate frequencies) is often observed.[20]

1.3. Experimental Observations of Chaos

The recent theoretical developments in chaotic dynamics[7,11] have resulted in the experimental observation of chaos in a wide range of physical systems.[2,21] In many instances, the physical system may be adequately modeled by coupled ordinary differential equations. These systems have a well-defined, finite number of degrees of freedom and, when such a system is chaotic, its evolution is confined to a strange attractor of dimension less than this total number of degrees of freedom. That is, not all of the potential degrees of freedom are "active." The Belousov-Zhabotinski chemical reaction is an example of such a finite-dimensional chaotic system. A number of condensed matter systems also fall into this category. These include: Josephson junctions,[22]

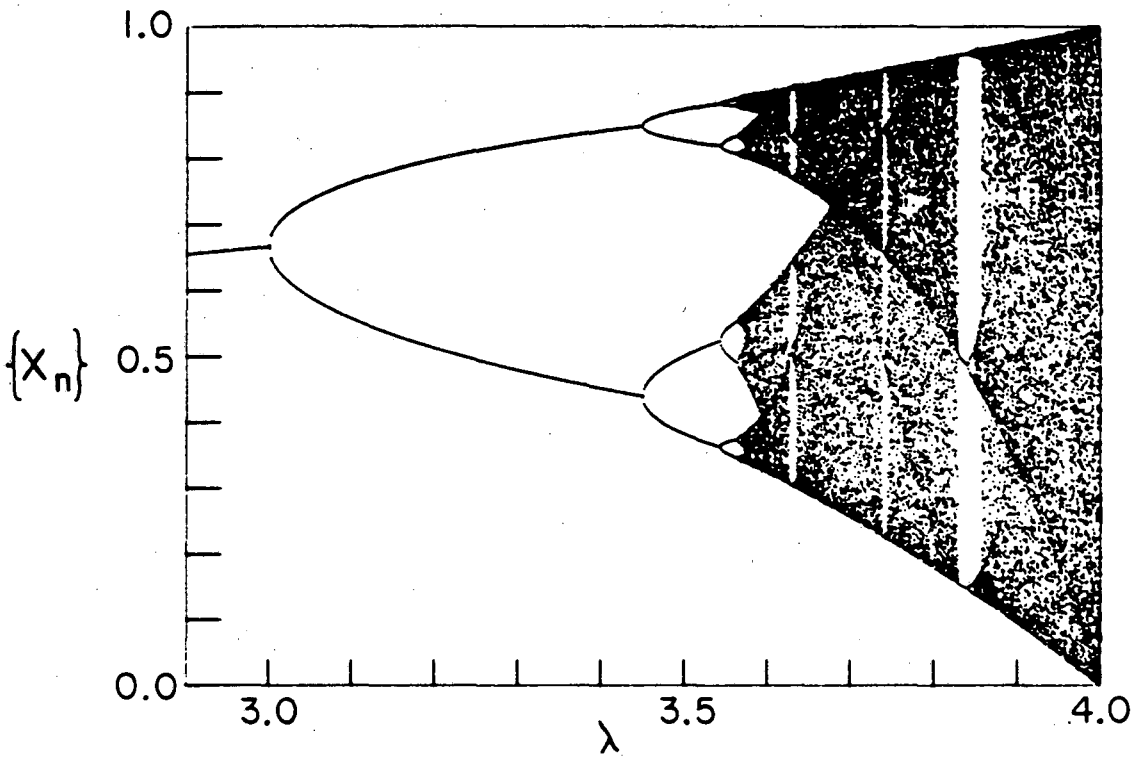

XBL 8510-4184

Figure 1.2. A bifurcation diagram of the logistic map [equation (1.1)]. The attractor set $\{ x_n \}$ is plotted versus the control parameter λ. Eighty iterations are plotted after an initial 500 iterations for each increment of the control parameter. The control parameter was incremented 500 times in the interval shown.

driven p-n junctions,[23] and far infrared photoconductors.[24]

Hydrodynamic systems, which are described by partial differential equations and therefore have (effectively) an infinite number of degrees of freedom, have also been shown to undergo transitions to chaotic states characterized by only a few active degrees of freedom.[2] Rayleigh-Bénard convection and Couette-Taylor flows, as well as the present work on electron-hole plasmas are examples of nonlinear continuum media that exhibit low-dimensional chaos.

A number of experimental probes are useful in identifying and characterizing low-dimensional chaotic behavior. Perhaps the single feature most useful in characterizing a transition to chaos is the power spectrum of the time series of an experimentally observable variable (for example, the velocity of fluid flow in a hydrodynamic system). From the power spectrum one can detect the onsets of spontaneous oscillations, period doubling, quasiperiodicity, and the broadband spectral "noise" characteristic of chaotic behavior.

When a system follows one of the universal routes to chaos (for example, a cascade of period doublings is followed by a broadband power spectrum), one may strongly infer that the resulting broadband state is indeed chaotic. However, observation of only power spectra does not enable one to rigorously distinguish between deterministic chaos and stochastic noise; both result in broadened spectral peaks.[10] To firmly establish that the observed behavior is chaotic, one must examine the structure of the attractor itself. This requires methods of data reduction designed specifically to identify and characterize low-dimensional chaotic attractors. These include the construction of phase

portraits, Poincaré sections, return maps, and bifurcation diagrams. In those cases where the chaotic behavior is characterized by an attractor of dimension greater than approximately 2.5, even these methods of analysis cannot distinguish between chaos and stochastic noise; the fractal structure of the attractor becomes too dense to be discerned through visual inspection of a 2-dimensional projection of a Poincaré section. In such instances, one must calculate quantitative measures of chaos such as the fractal dimension, Lyapunov exponents, and metric entropy of the attractor. Techniques for calculating fractal dimensions are discussed in Chapter III; calculations of other measures of chaos are described elsewhere.[25,26,27]

1.4. Helical Instabilities in Semiconductor Plasmas

The onset of spontaneous current oscillations in a Ge crystal placed in parallel dc electric and magnetic fields was first reported by Ivanov and Ryvkin.[28] This instability, the so-called "oscillistor" effect, was subsequently observed in other semiconductors as well.[29,30] Larrabee and Steele[31,32] reported a detailed experimental study of this instability in Ge rods. In particular, they noted that the spontaneous oscillations would develop only if both electrons and holes were present in the crystal. Specifically, when they electrically injected both electrons and holes into a sample, they observed spontaneous oscillations in the absence of optical illumination. However, when only majority carriers were injected electrically (i.e., ohmic contacts were formed on both ends of the sample) oscillations were only observed in

the presence of optical pumping (which generated the necessary minority carriers). The oscillistor effect is observed when the applied electric and magnetic fields are either parallel or antiparallel to within approximately 5°. Early reports[33] suggesting that exactly parallel fields applied along a perfectly cylindrical sample would not exhibit these oscillations were found to be in error.[1] It is possible that chaotic behavior was observed during some of these early experiments but was not recognized as such, owing to the lack of the mathematical framework now available.

Glicksman[34] developed a theoretical model attributing the observed current oscillations to an unstable screw-shaped helical travelling wave within the electron-hole plasma. This model was based on a model developed by Kadomtsev and Nedospasov[35] to explain a similar instability observed in gaseous plasmas. An illustration of this travelling helical density wave, after Hoh and Lehnert,[36] is shown in figure 1.3. The helical structure within the cylinder corresponds to a region of enhanced electron and hole density.

The helical nature of this instability was subsequently confirmed experimentally by Hurwitz and McWhorter[1] and Misawa.[37] Hurwitz and McWhorter utilized electrical probe contacts to measure variations in the plasma density within their crystals, whereas Misawa used microwave scattering. Both experiments found radial and lengthwise variations in plasma density which supported the existence of a helical instability such as that depicted in figure 1.3.

Further theoretical treatments of these instabilities were carried out by Hurwitz and McWhorter[1] and Schulz.[38] All of these treatments dealt with

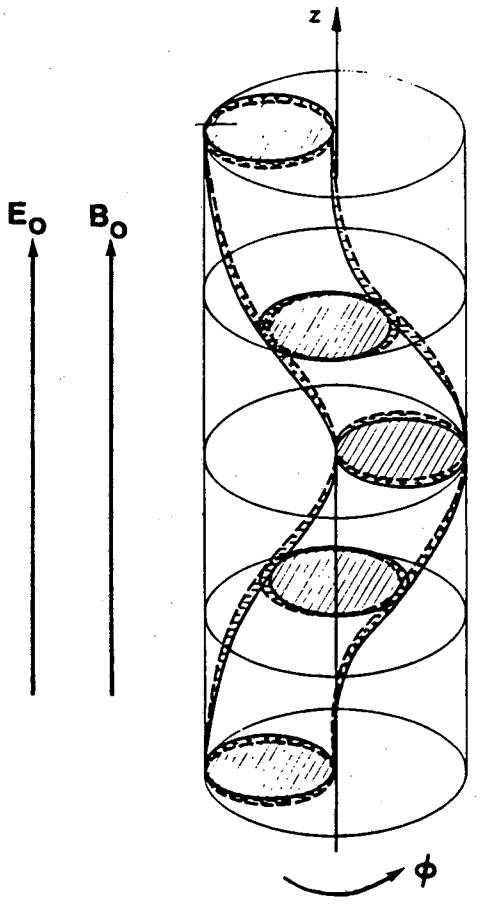

Figure 1.3. Model of helical plasma density wave in semiconductor cylinder, after Hoh and Lehnert.[36] Electric field E_0 and magnetic field B_0 are applied along the z-axis. The helix contained within the cylinder represents the region of enhanced electron and hole density.

linear perturbations of steady-state, non-oscillatory current flow. The basic equations governing this system, a review of the linear analysis which predicts instabilities such as the one depicted in figure 1.3, and a discussion of the possible nonlinear interactions which must be considered in any explanation of the chaotic behavior which we observe are included in Appendix A of the present work.

References. Chapter I

1. C. E. Hurwitz and A. L. McWhorter, Phys. Rev. **134**, A1033 (1964).

2. for example, H. L. Swinney, Physica (Utrecht) **7D**, 3 (1983).

3. A. Brandstäter *et al.* , Phys. Rev. Lett. **51**, 1442 (1983).

4. for example, J.-M. Wersinger, J. M. Finn, and E. Ott, Phys. Fluids **23**, 1142 (1980).

5. for example, A. J. Lichtenberg and M. A. Lieberman, *Regular and Stochastic Motion* (Springer Verlag, New York, 1983), p. 17.

6. D. Ruelle and F. Takens, Comm. Math. Phys. **20**, 167 (1971).

7. for example, E. Ott, Rev. Mod. Phys. **53**, 643 (1981).

8. Duffing's equation is included in the caption of figure 1.1. This figure is courtesy of J. P. Crutchfield.

9. for example, J. D. Farmer, E. Ott, J. A. Yorke, Physica (Utrecht) **7D**, 153 (1983).

10. H. L. Swinney and J. P. Gollub, to appear in Physica **D**.

11. for example, J.-P. Eckmann, Rev. Mod. Phys. **53**, 643 (1981).

12. M. J. Feigenbaum, Los Alamos Science, **Summer**, 4 (1980); J. Stat. Phys. **19**, 25 (1978).

13. M. Nauenberg and J. Rudnick, Phys. Rev. **B 24**, 493 (1981).

14. for example, J. P. Crutchfield, J. D. Farmer, and B. A. Huberman, Phys. Rep. **92**, 47 (1982).

15. N. Metropolis, M. L. Stein, and P. R. Stein, J. Comb. Theory, Ser. **A 15**, 25 (1973).

16. P. Manneville and Y. Pomeau, Phys. Lett. **75A**, 1 (1979); Y. Pomeau and P. Manneville, Comm. Math. Phys. **74**, 189 (1980).

17. E. Hirsch, B. A. Huberman, and D. J. Scalapino, Phys. Rev. **A 25**, 519 (1982).

18. D. G. Aronson, M. A. Chory, G. R. Hill and R. P. McGehee, Comm. Math. Phys. **83**, 303 (1982); in *Nonlinear Dynamics and Turbulence,* edited by G. I. Barrenblatt, G. Iooss and D. D. Joseph (Pittman, London, 1982).

19. M. J. Feigenbaum, L. P. Kadanoff, and S. J. Shenker, Physica (Amsterdam) **5D**, 370 (1982); D. Rand, S. Ostlund, J. Sethna, and E. Siggia, Physica (Amsterdam) **8D**, 303 (1983).

20. J. P. Gollub and S. V. Benson, J. Fluid Mech. **100**, 449 (1980).

21. for example, *The Physics of Chaos and Related Problems,* edited by S. Lundqvist, Phys. Scr. **T9**, (1985).

22. R. F. Miracky, J. Clarke, and R. H. Koch, Phys. Rev. Lett. **50**, 856 (1983).

23. P. S. Linsay, Phys. Rev. Lett. **47**, 1349 (1981); J. Testa, J. Perez and C. Jeffries, Phys. Rev. Lett. **48**, 714 (1982).

24. S. W. Teitsworth, R. M. Westervelt and E. E. Haller, Phys. Rev. Lett. **51**, 825 (1983).

25. A. Wolf, J. B. Swift, H. L. Swinney and J. A. Vastano, Physica **16D**, 285 (1985).

26. J. P. Crutchfield and N. H. Packard, Int. J. Theor. Phys. **21**, 433 (1982); Physica **7D**, 201 (1983).

27. P. Grassberger and I. Procaccia, Phys. Rev. **A 28**, 2591 (1983).

28. I. L. Ivanov and S. M. Ryvkin, Zh. Tekh. Fiz. **28**, 774 (1958) [Sov. Phys. Tech. Phys. **3**, 722 (1958)].

29. for a review see, R. Bowers and M. C. Steele, Proc. of the IEEE **52**, 1105 (1964).

30. J. Bok and R. Veilex, Compt. Rend. **248**, 2300 (1958).

31. R. D. Larrabee and M. C. Steele, J. Appl. Phys. **31**, 1519 (1960).

32. R. D. Larrabee, J. Appl. Phys. **34**, 880 (1963).

33. F. Okamoto, T. Koike and S. Tosima, J. Phys. Soc. Japan **17**, 804 (1962).

34. M. Glicksman, Phys. Rev. **124**, 1655 (1961).

35. B. B. Kadomtsev and A. V. Nedospasov, J. Nucl. Energy **1**, 230 (1960).

36. F. C. Hoh and B. Lehnert, Phys. Rev. Lett. **7**, 75 (1961).

37. T. Misawa and T. Yamada, Jpn. J. Appl. Phys. **2**, 19 (1963).

38. M. Shulz, Phys. Status Solidi **25**, 521 (1968).

CHAPTER II. EXPERIMENTAL APPARATUS AND PROCEDURES

2.1. Sample Preparation

The samples used in these experiments were all cut from large, single crystals of Ge grown by E. E. Haller and W. L. Hansen at the Lawrence Berkeley Laboratory. The method of production is described in detail elsewhere.[1] Table 2-1 lists the dimensions, growth environment, and some physical properties of our samples. Most of the experimental work was performed on 1 x 1 x 10 mm^3 samples cut from a single crystal of n-Ge with a net donor concentration of 3.7 x 10^{12} cm^{-3} (i.e., samples 1A - 1E); these samples tended to exhibit the greatest wealth of nonlinear behavior.

Our electron-hole (e-h) plasma is generated either by double injection or optical pumping. In those samples where double injection is utilized, a Li-diffused n^+ contact and a B-implanted p^+ contact were formed on opposite ends of the crystal. In those samples where minority carriers are generated by optical excitation, either n^+ or p^+ contacts (on n-Ge and p-Ge samples, respectively) were formed on both ends of the sample. In each case, a palladium film was evaporated onto the contacts and a gold film was sputtered onto the palladium.

P-implanted n^+ contacts were formed on two opposite 1 x 10 mm^2 faces of sample 1E (in addition to the current injecting contacts on the 1 x 1 mm^2

faces). A gold film was then sputtered onto these contacts. Using photolithography, we etched onto these two faces a pattern of eight pairs of contacts, 0.5 mm wide and spaced 1 mm along the length of the sample. The voltage across a pair of these contacts is a measure of the local variation in the plasma density.[2]

After all contacts on a given sample were formed, the sample was etched for approximately 30 seconds in 3:1 HNO_3:HF and subsequently quenched with methanol. Prior to etching, sample 1E was etched in KI:I_2 for approximately 1 minute so as to etch the pattern of probe contacts into the gold film covering the 1 x 10 mm^2 faces. During all of the etches, the current injecting contacts were protected with pycine; the pattern of P-implanted contacts on sample 1E was protected with photoresist. All samples were placed in dry air for 72 hours to allow the surfaces to passivate. Wires were indium soldered to the end (current injecting) contacts, and (with some difficulty) were attached with conducting epoxy to the P-implanted (spatial probe) contacts.

2.2. Experimental Apparatus

When taking data, the sample is cooled to 77K in liquid nitrogen and connected in series with a 100Ω resistor and a variable dc voltage V_0, which generates the dc electric field E_0. A magnetic field B_0 is applied parallel ($\pm 3°$) to the length of the sample. The electron-hole plasma is generated by V_0, via double injection, in those samples with p^+ and n^+ contacts on opposite ends.

Table 2-1. Germanium Crystal Samples

Sample	Boule[a]	Growth Direction	Growth Atmosphere	Dislocations (etch pit density) (cm^{-2})	Impurities N_D–N_A (cm^{-3})
1A 1B 1C 1D 1E	400-4.0	<111>	Ar	5000	3.7×10^{12} (P)
2	112-22.5	<100>	H_2+N_2	$\approx 10^2$	-2.3×10^{14} (Ga)
3	437-5.0	<111>	H_2	0	2×10^{10}
4	150-5.4	<100>	H_2	0	-2×10^{11}
5	464-4.1	<100>	H_2	6×10^3	3×10^{12} (P,As)

Table 2-1 (continued)

Sample	Dimensions mm x mm x mm	End Contacts	Special Comments
1A	1 x 1 x 10	B-Li	high C, grown
1B	1 x 3 x 10	B-Li	in graphite crucible
1C	1 x 1 x 10	Li-Li	
1D	1 x 1 x 10	P-Li	
1E	1 x 1 x 10	B-Li	1E has side contacts
2	1 x 1 x 10	B-Li	[Ga] $\approx 3 \times 10^{14}$ cm^{-3} O, Si, P; ≈ 8 Ω–cm
3	1 x 1 x 10	B-Li	very high [Si] $\approx 10^{16}$ cm^{-3} high purity, N_A, $N_D \leq 10^{11}$ cm^{-3}
4	1 x 1 x 10	B-B	[O], [Si] $\approx 10^{14}$ cm^{-3} high purity, N_A, $N_D \leq 10^{11}$ cm^{-3}
5	12.5 mm diam. x 1 cm right cylinder	B-Li	low [Al] $\approx 10^{10}$ cm^{-3} [Ga] $\approx 1.6 \times 10^{10}$ cm^{-3} [B] $\approx 2.2 \times 10^{11}$ cm^{-3}

[a]This is notation for crystals grown at LBL by W. L. Hansen and E. E. Haller.

A 10 mWatt Spectra-Physics He-Ne laser was used to generate minority carriers, via optical pumping, in those samples with ohmic contacts on both ends (samples 1C and 4).

The applied voltage V_0, the applied magnetic field B_0 and the angle between the two fields θ, comprise our control parameters; typically $\theta = 0 \pm 3°$. In practice, we fix B_0 and θ and sweep V_0, while recording the dynamical variables which characterize the plasma behavior. These include the current passing through the sample, I(t), the voltage across the sample, V(t), and in the case of sample 1E, the voltages across the pairs of probe contacts $V_i(t)$. The methods by which data are collected and examined are discussed in the following sections of this chapter. An illustration of the basic sample configuration, with probe contacts, is shown in figure 2.1.

In Chapter V we discuss the results of coupling the natural (spontaneous) plasma instabilities with an externally excited plasma mode. The external mode is generated through the application of a sinusoidal voltage across one of the pairs of probe contacts. The strongest coupling results when the probe pair nearest the p^+ contact is driven externally. The external excitation is of the form $V_1 \sin\omega t$, and, when such an excitation is present, the control parameters include V_1 and ω, as well as V_0, B_0, and θ.

The samples are mounted onto a flat brass sample holder which attaches to the bottom of a microwave dewar insert.[3] The insert is then lowered into a dewar, the dimensions of which are described elsewhere.[4] The sample is held onto the sample holder with clips formed from spring wire and the sample is

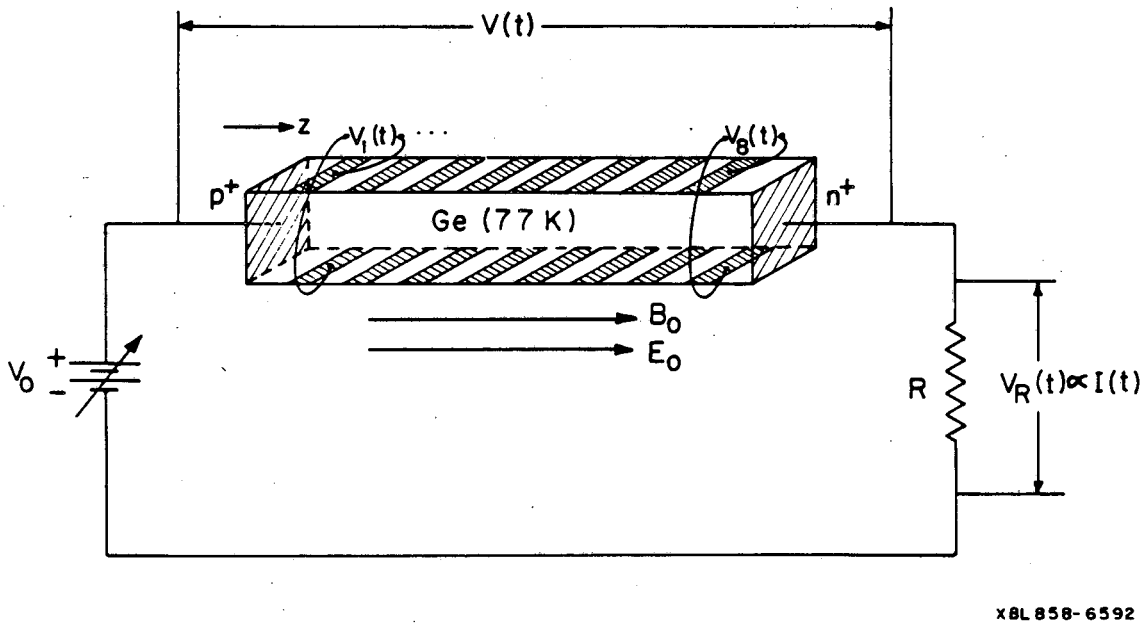

Figure 2.1. Illustration of basic experimental configuration. Ge crystal is in electric field E_0 and magnetic field B_0 at temperature $T \approx 77$ K. Electrons and holes injected from n^+ and p^+ contacts, respectively, generate plasma of density $\approx 10^{13}$ cm^{-3}. On increasing V_0 helical plasma density waves form and become chaotic. Plasma monitored by current I(t), voltage between end contacts V(t), and voltages $V_i(t)$ from eight pairs of n^+ side probes, each 0.5 mm wide, spaced by 1 mm along z-axis.

electrically insulated from the holder with 0.25 mil mylar; the thin mylar film provides both good electrical insulation and adequate thermal conduction between the sample and the brass holder. All wires making electrical contact with the sample are soldered onto binding posts on the sample holder. Figure 2.2 is a photograph of sample 1E mounted on the sample holder. Electrical connection between the sample holder and the outside of the dewar is made with shielded twisted pair cables.

The sample is centered between the pole pieces of the split coil magnet, which can be rotated in the horizontal plane. The magnetic field is measured with a rotating coil gaussmeter and has an upper limit of 19 kGauss. Optical pumping is achieved through a window on the bottom of the dewar.

2.3. Analog Data Collection

The voltage across the sample V(t) and the current passing through the sample I(t) (which is proportional to the voltage across the series resistance $V_R(t)$) are the principal dynamical variables utilized in our studies of temporal behavior. Time series of these variables were recorded with a Biomation 805 waveform recorder, and also with with a Tektronix (Tek) 468 digital storage oscilloscope. The basic periodicity (or lack of thereof) is readily observable by visual examination of these real time signals. However, we find that power spectra provide a more precise means of identifying the harmonic and subharmonic content of the signals and also of determining the onset of nonperiodic behavior. Power spectra were recorded with a Nelson Ross

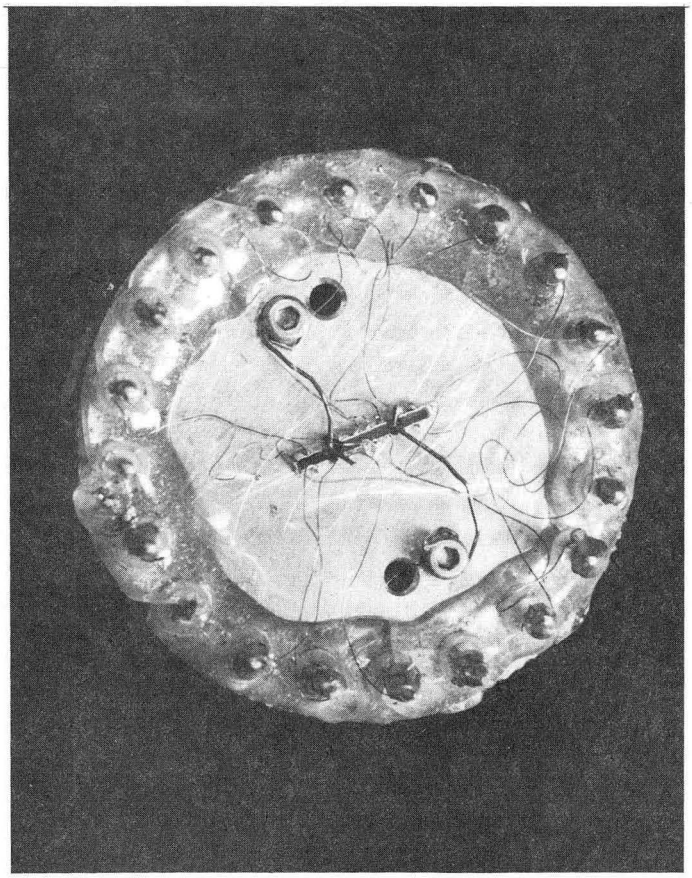

XBB 850-8394

Figure 2.2. Photograph of sample 1E attached to sample holder.

PSA013 scanning spectrum analyzer and a Hewlett Packard (HP) 3585A scanning spectrum analyzer. Fast Fourier transforms of real time series taken with a DEC LSI-11/23 computer were also calculated. The scanning spectrum analyzers have the advantage that alias peaks do not present a problem. The Nelson Ross displays the power spectrum on an oscilloscope, which must then be photographed. The HP 3585A interfaces to our LSI-11/23 computer via an IEEE-488 interface connector, allowing the power spectra to be stored digitally and plotted on an HP plotter.

A plot of the phase portrait, V(t) vs. I(t), provides a geometric visualization of the attractor. However, to see the fractal structure within the strange attractor, one must look at a cross-section of the phase portrait, i.e., a Poincaré section. To obtain a Poincaré section, it is necessary to consider the locus of points $(V(t_n)\ ,\ I(t_n))$ at some discrete set of times $\{\ t_n\ \}$. Formally[5], these times must be chosen such that the set of points $(V(t_n)\ ,\ I(t_n))$ comprise a plane in phase space perpendicular to the trajectories which are followed by the evolving system. If the system under study were driven with an external oscillator, $A\sin\omega t$, then $\{\ t_n\ \}$ could be chosen to be the set of times at which the phase of the oscillator, $(\omega t)_{\mathrm{mod}\ 2\pi}$, equaled some particular value -- for example, $(\omega t)_{\mathrm{mod}\ 2\pi} = 0$. Both experimental[6] and theoretical[7] Poincaré sections have been observed in this fashion.

However, if the system is not externally driven (such as the case of most of our experiments), the observation of a Poincaré section is more difficult. In those instances where a strong fundamental peak rises above the broadband

"noise" in the power spectrum, we have been able to strobe the system at a specific phase of this fundamental frequency. Specifically, we filter out frequencies above the fundamental frequency of I(t) and then strobe I(t) at the local current maxima. We then plot a return map, I_{n+1} vs. I_n, where $\{ I_n \}$ is the set of local current maxima (see Chapter III, figures 3.4 and 3.5). The return map is topologically equivalent to a Poincaré section.[8]

A block diagram of the circuitry used to generate a return map from the time series I(t) is shown in figure 2.3. First, the current is filtered to remove harmonic distortion. The filters used are Ithaco 4302 dual 24dB/octave filters and a Krohn-Hite 3550 band-pass filter. The filter settings are shown in figure 2.4. Figures 3.1 and 3.2 of Chapter III show the filtered and unfiltered current I(t). It is clear from these figures that the filtered signal has a single maxima per cycle of the fundamental frequency whereas the unfiltered signal has many. Thus it is essential that the derivative of the filtered signal be used to clock the return map circuitry.

The differentiating circuit is shown in detail in figure 2.5. The filtered signal is amplified and then differentiated using Tektronix type "O" plug-in op-amps. These op-amps have a 25 MHz bandwidth and the differentiated signal crosses zero within 0.05 μs of a local maxima of a 200 kHz signal. The differentiated signal is fed into a fast LM306 comparator, the output of which swings between ground and 5 volts depending on whether the differentiated signal is greater or less than zero volts. The output of the LM306 is fed into

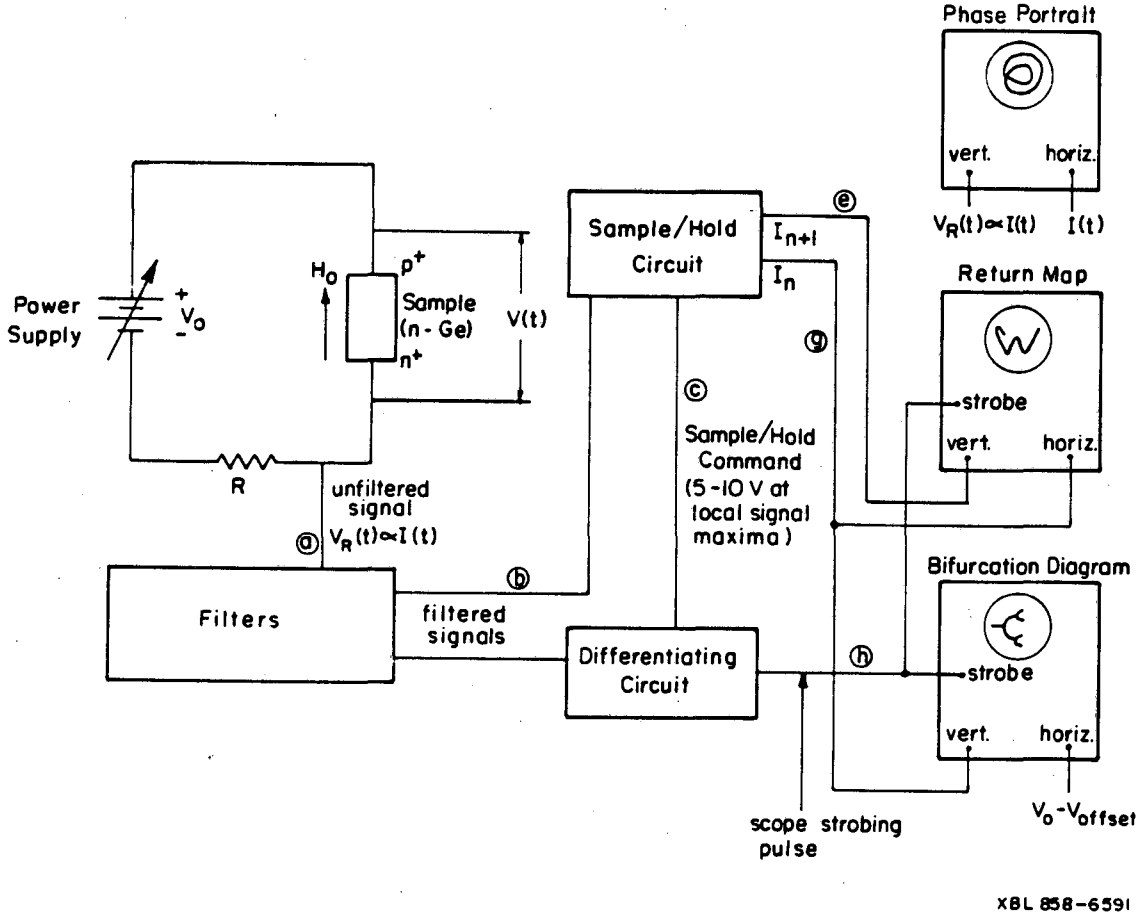

Figure 2.3. Block diagram of analog circuitry required to generate return maps, phase portraits, and bifurcation diagrams from the real time current I(t). Voltage signals at the points labeled (a), (b), (c), (d), (e), (g) and (h) are depicted in figure 2.7. Details of the filters, differentiating circuit and sample/hold circuit are shown in figures 2.4, 2.5 and 2.6, respectively.

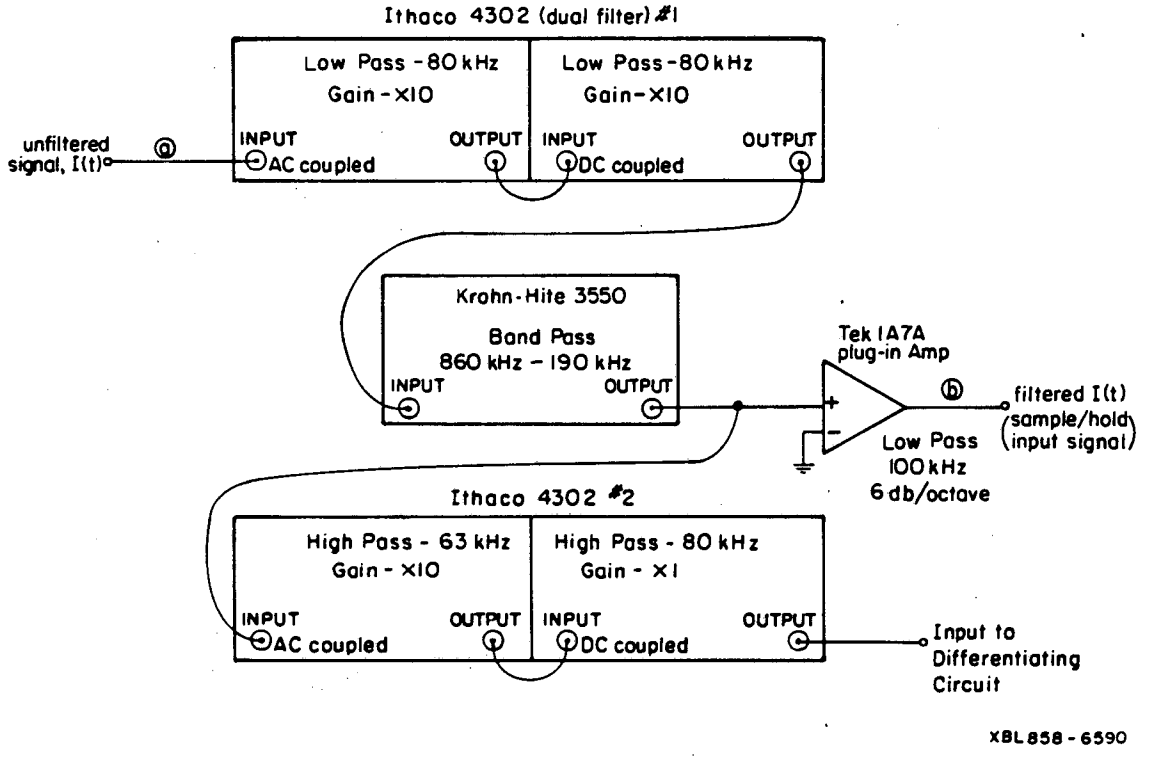

Figure 2.4. Detail of filters of figure 2.3. The voltage signals at points labeled (a) and (b) are depicted in figure 2.7.

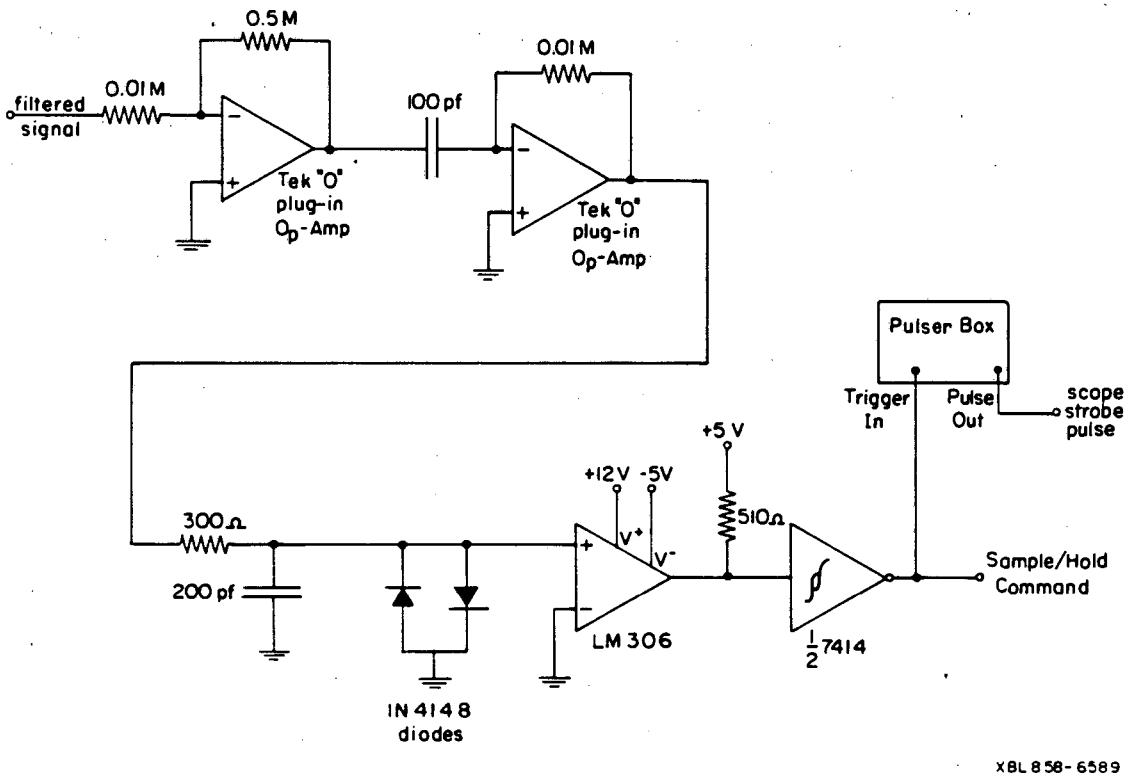

Figure 2.5. Detailed schematic of differentiating circuit of figure 2.3.

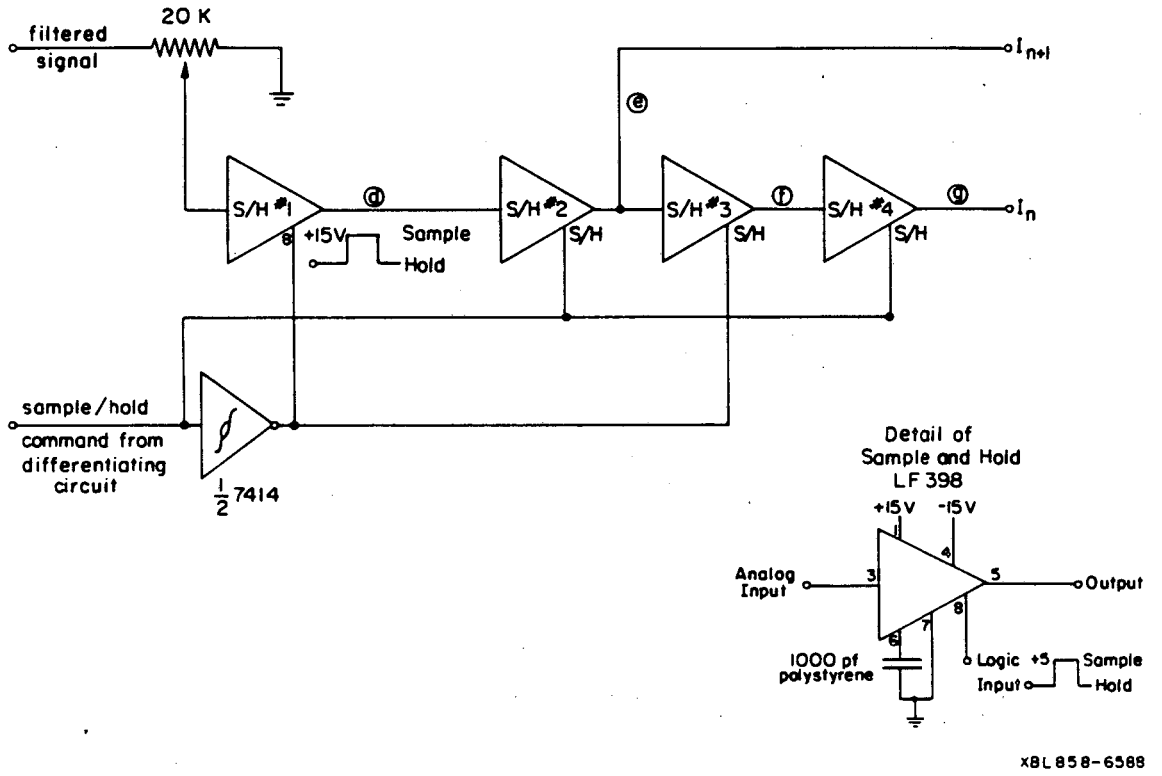

Figure 2.6. Detailed schematic of sample/hold circuit of figure 2.3. The voltage signals at points labeled (d), (e), (f) and (g) are depicted in figure 2.7.

a 7414 Schmidt trigger (TTL) inverter. The output of this entire circuit follows a 200 kHz signal to within 2%. That is, the 7414 output swings from 0 to 5 volts within 0.1 μs of a local maxima in the input signal.

The TTL output of the differentiating circuit is used to clock the sample/hold circuit shown in figure 2.6.[9] The filtered current I(t) is input to the first LM398 sample and hold amplifier (S/H #1). The output of S/H #1 is held at the value of a local maxima, which is then fed into a second LM398 (S/H #2). S/H #2 is clocked by the inverse of the signal which clocks S/H #1. Therefore, S/H #2 continues to hold the value of the local maxima, while S/H #1 returns to its sampling phase. This process can be extended another full cycle by placing two more sample and holds into the series; each LM398 delays the signal by a half-cycle. This process is depicted in figure 2.7. At any given time, the output of S/H #2 is the most recent local maxima, I_{n+1}, while the output of S/H #4 (delayed 360° from S/H #2) is the previous local maxima, I_n. When these signals are fed into the vertical and horizontal inputs of an oscilloscope, respectively (and the scope is z-modulated so that the CRT is illuminated only when the outputs of S/H #2 and S/H #4 have stabilized) a return map is projected onto the CRT. LM398 sample and hold amplifiers, used in conjunction with 1000 pf polystyrene hold capacitors, have an acquisition time to 0.1% of 4 μs; they produce accurate return maps for signals with fundamental frequencies as large as 200 kHz. Analog Devices AD582's (a comparably priced sample and hold) do not respond quickly enough to generate a return map from a 200 kHz signal.

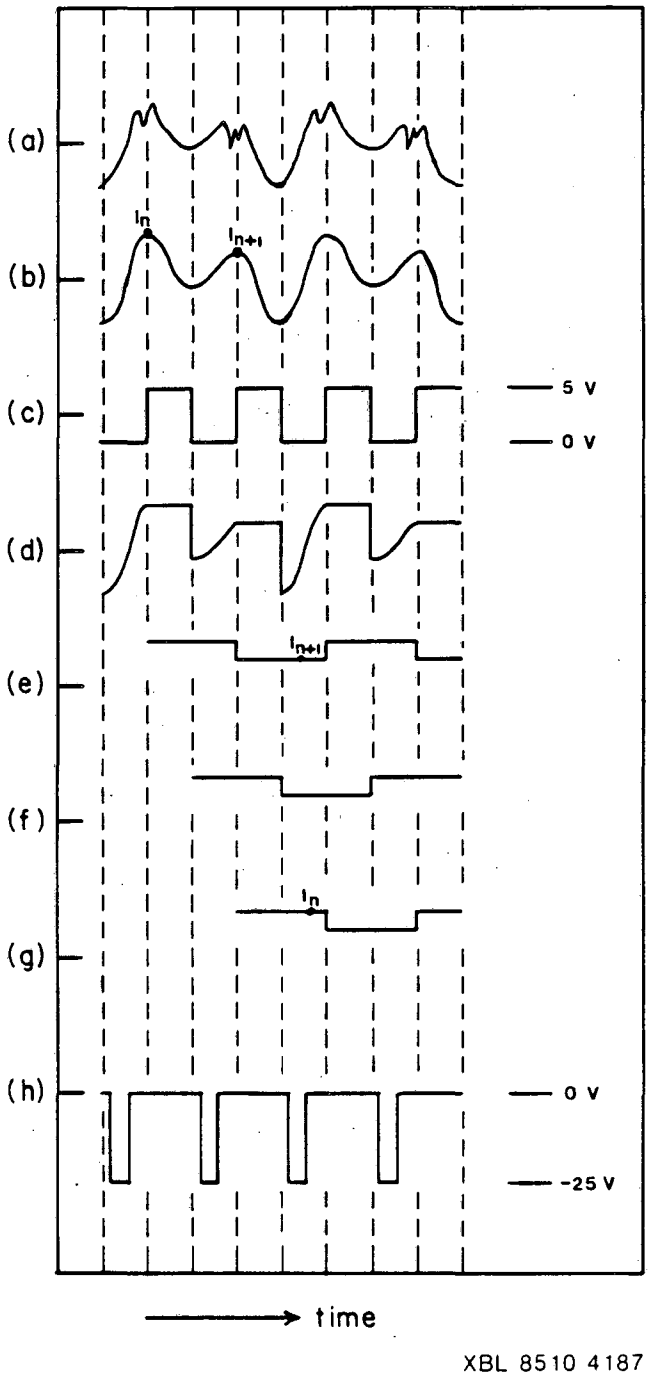

Figure 2.7. Depiction of voltage signals at points labeled (a) - (h) in figures 2.3, 2.4 and 2.6 for a hypothetical current I(t). This figure illustrates the workings of the analog circuitry of figures 2.3 - 2.6.

To generate bifurcation diagrams, only slight modifications of the return map circuitry are required. The output of S/H #4, I_n, is fed into the vertical input of an oscilloscope, and the applied dc voltage V_0 (less some offset) is used as the horizontal input to the scope. The scope is z-modulated so that the CRT is illuminated when the output of S/H #4 has stabilized. Thus, for a fixed value of V_0, a vertical series of points (each point representative of a local current maxima) appear on the CRT. As V_0 is increased, the series of points moves to the right; the number of points changes with the periodicity of the current I(t), while the spacing between points changes with the relative heights of the local maxima, I_n. A bifurcation diagram is generated by taking a timed exposure of the CRT while sweeping V_0. These diagrams (see, for example, Chapter III, figure 3.3) provide a good overview of the entire transition from periodicity to chaos; the sequences of period doubling bifurcations, regions of chaos and noise-free periodic windows may all be seen in a single figure.

2.4. Digital Data Collection

Fractal dimensions, spatial correlation functions, and other quantities which characterize chaotic instabilities are all calculated from digitized time series of the dynamical variables of the chaotic system. The methods by which we collect digitized time series are described in this section. The methods of calculating fractal dimensions and spatial correlation functions from these time series are discussed in Chapters III and IV. The computer

programs used in collecting data and calculating these quantities are included in Appendix B.

All of our digitized data is collected and stored with a DEC LSI-11/23 microcomputer. The LSI-11/23 has serial ports, an IEEE-488 interface, analog/digital (A/D) and digital/analog (D/A) converters, and is thus capable of controlling other instruments (for example, HP 3585A spectrum analyzer, Tek 468 storage oscilloscope, and HP 7470A plotter), collecting and displaying digitized signals, performing simple calculations (for example, fast Fourier transforms and spatial correlation calculations) and transmitting data to more powerful computers when more extensive computations are required. A summary of the modules which comprise this computer system is shown in table 2-2.

Calculations of fractal dimensions require a long time series (typically 10^3 – 10^6 data points) of an independent variable of the system. Our Data Translation DT3382 A/D module is capable of collecting up to 98000 data points at 5 μs intervals and storing the data in random access memory. It is also capable of writing the data directly to a Winchester disk. In this mode the sampling rate is 67 kHz, but time series of up to 2 x 10^7 data points may be collected in a single sweep. The DT3382 A/D has 12 bit resolution and a dynamic range of 20 volts.

Table 2-2. Components of Data Aquisition Computer System

Slots(s)	Module	Function
1	DEC KDF11-A	LSI-11/23 CPU with Memory Management and Floating Point Unit
2	Motorola MMS1132	256 kByte Random Access Memory
3,4	Data Translation DT3382	250 kHz, 12-bit A/D Converter
5	National Inst. GPIB11V-1	IEEE-488 Interface
6	DEC DLV11-J	Four Serial Ports
7	DEC KWV11-C	Timer and Counters
8,9	Connector	
10	DSD 440	Floppy Disk Drive Controller
11	ADAC 1412DA	D/A Converter
12	DEC DRV11	8-bit Parallel Port
13,14	Data Translation DT3388	100kHz, 8 Channel Simultaneous 12-bit A/D Converters
15	Andromeda WDC11-DW	40 MByte Winchester Disk Controller
16,17	Connector	
24	DEC TEV11	Termination Module

When collecting time series data we utilize two different sampling methods, which we refer to as commensurate and incommensurate strobing. When a dynamic variable has a strong fundamental frequency, it is possible to collect the data at some particular phase of the fundamental frequency (just as it is possible to construct a return map from data taken at that particular phase); this is commensurate strobing. In practice, the data is digitally sampled at each local maxima of the time series, or at some fixed time delay after each local maxima. The TTL pulse which instructs the computer to sample is the same as the signal which clocks S/H #2 and S/H #4 in the return map electronics discussed in the previous section. When data is collected by this method, we may immediately display a return map derived from the digitized data, and thus verify that the instrumentation is operating correctly. This is accomplished by sending the digitized pairs of points (I_n , I_{n+1}), to the computer's D/A module, which in turn transmits appropriately scaled output voltages to the x- and y-inputs of a Tek 611 storage oscilloscope. The "pulse trigger" of the D/A module triggers the z-input of the scope and the return map is observed on the CRT.

When collecting data by incommensurate strobing, a computer controlled quartz oscillator (on the KWV11-C module) sets the data sampling frequency. This frequency is completely unrelated to any natural frequencies of the plasma. Thus, when data are collected in this fashion, all phases of the fundamental plasma frequency are eventually sampled, if indeed such a frequency even exists (it does not exist when the plasma is highly excited).

Incommensurate strobing samples the entire attractor, whereas commensurate strobing samples only a cross-section. We therefore expect (and observe) that the fractal dimension of the commensurately strobed data (i.e., the cross-section) will be less than the fractal dimension of the incommensurately strobed data (i.e., the entire attractor) by unity. The advantage of incommensurate data collection is that it does not require the extensive filtering, differentiating, and comparator circuitry of figure 2.3. Further, it does not require the existence of a strong fundamental frequency in the power spectrum of the plasma instabilities. It is therefore of more general usefulness than the method of commensurate strobing.

Studies of spatial coherence require the simultaneous sampling of spatially separated, independent variables. To calculate spatial correlation functions, we must record time series of the voltages across two pairs of probe contacts, $V_i(t)$ and $V_j(t)$, measured simultaneously. This is accomplished through two alternate methods. In the first method the data is digitized by the DT3382 A/D module and in the second the data is collected with the Tek 468 storage oscilloscope.

In the first method, the voltages across two pairs of probe contacts, $V_i(t)$ and $V_j(t)$, are each fed into Tektronix AM502 differential amplifiers. The output of these two differential amplifiers are passed through matching 2.3 kHz high-pass RC filters (to remove low frequency drifts) and then fed into Teledyne-Philbrick 4860 sample and hold amplifiers. The computer controlled clock triggers a pulse which puts both sample and holds into hold mode long

enough (6 μs) for both $V_i(t)$ and $V_j(t)$ to be sampled by the DT3382 A/D converter. In this fashion, the two voltages $V_i(t)$ and $V_j(t)$ may be sampled simultaneously at rates of up to 100 kHz. In determining spatial correlation functions, it is critical that the differential amplifiers as well as the sample and holds not introduce mismatched phase shifts into the signals $V_i(t)$ and $V_j(t)$. The phase shifts of the AM502's were matched to within 1° up to 500 kHz; the 4860's are ultra-fast sample and hold amplifiers (16 MHz bandwidth) with no measurable mismatch in phase shifts at 500 kHz. Further, they have a droop rate of 0.05 μV/μs, and are thus able to hold a signal for the 6 μs necessary for both channels to be sampled. This method of sampling is therefore effective when collecting spatial correlation data which has no significant frequency components above, say, 500 kHz. Much of our data (the "weakly turbulent" data of Chapter III) falls into this regime. However, when highly excited by large applied fields, the plasma instabilities exhibit significant frequency components in the 1 – 1.5 MHz range.

Spatial data is collected for highly turbulent instabilities as follows: the voltages across two pairs of probe contacts $V_i(t)$ and $V_j(t)$ are each fed into Tektronix AM502 differential amplifiers. The outputs of these amplifiers are passed through 2.3 kHz high-pass RC filters and fed into channels A and B of a Tek 468 storage oscilloscope. The scope samples each input at 12.5 MHz and converts the voltages to 8 bit integers, which are subsequently transmitted to the LSI-11/23 computer. The oscilloscope collects 256 data points per channel in a single sweep and must transmit this data before performing

another sweep; this requires approximately 4 seconds. Thus, the collection of, say, 5120 pairs of data points, would consist of 20 sweeps each separated by approximately 4 seconds. It would clearly be desirable to instead perform a single, long sweep (this is not possible with the available equipment). However, the two methods of collecting spatial data are observed to yield comparable results (for low frequency instabilities), indicating that the 4 second delay between each sweep of 256 data points does not introduce any significant errors; the properties of the system do not change over this time scale.

References. Chapter II

1. W. L. Hansen and E. E. Haller, IEEE Trans. Nucl. Sci. **21**, 251 (1974); E. E. Haller and W. L. Hansen, IEEE Trans. Nucl. Sci. **21**, 279 (1974).

2. C. E. Hurwitz and A. L. McWhorter, Phys. Rev. **134**, A1033 (1964).

3. A microwave Dewar insert was used because it was readily available and provided a means of placing the mounted sample into the Dewar in the center of the magnetic field. The microwave capabilities of the insert were in no way utilized.

4. Elga Pakulis, Ph.D. Thesis, University of California, Berkeley (1982).

5. for example, A. J. Lichtenberg and M. A. Lieberman, *Regular and Stochastic Motion* (Springer Verlag, New York, 1983), p. 17.

6. for example, C. Jeffries and J. Perez, Phys. Rev. **A 26**, 2117 (1982).

7. for example, D. Ruelle in *La Recherche* No. 108 (Févner, 1980).

8. N. H. Packard, J. P. Crutchfield, J. D. Farmer, and R. S. Shaw, Phys. Rev. Lett. **45**, 712 (1980).

9. The circuit of figure 2.6 is based on a similar circuit designed by George Gibson.

CHAPTER III. RESULTS: TEMPORAL ROUTES TO CHAOS

3.1. General Results

We have studied the dynamics of electron-hole (e-h) plasmas in samples cut from five different Ge crystals, as listed in table 2-1. For four of these we observed spontaneous oscillations when parallel electric and magnetic fields were applied along the length of the crystal; in three of these cases we observed a transition to turbulence. As discussed in Chapter II, the e-h plasma may be generated either by double injection or optical excitation, the former requiring electron and hole injecting contacts on opposite ends of the sample. Injecting contacts were formed on samples 1 (except 1C), 2, 3, and 5 (notation from table 2-1). Of these, samples 1 and 3 showed period doublings, quasiperiodicity, and chaos. Sample 5 exhibited spontaneous oscillations which became noise-like in the presence of large applied fields. We were unable to establish whether this noise was of stochastic or chaotic origin. We note that sample 5 was the only sample cut so that its width is comparable to its length. Waves reflected from the ends of the crystal are therefore significant and the standard theory of travelling helical density waves (see Appendix A) is no longer applicable. In sample 2 we observed neither chaos nor spontaneous oscillations. This is not surprising; previous studies[1] failed to observe oscillations in comparably doped crystals (sample 2 has a net

acceptor concentration two orders of magnitude larger than any of our other samples). According to the theory of Hurwitz and McWhorter[1], samples with an impurity concentration greater than approximately 10^{12} cm^{-3} will have an ambipolar drift mobility which is large enough to inhibit the formation of spontaneous oscillations; unstable perturbations in the current flow are swept across the sample before they develop into temporal oscillations.

Ohmic contacts were formed on samples 1C and 4. In both cases, no oscillations or chaotic dynamics were observed in the absence of optical generation of minority carriers, regardless of the magnitude of the applied dc fields. However, when optically pumped with a 10 mWatt He-Ne laser at 6328 Å, both samples developed coherent oscillations, and sample 1C followed a period doubling transition to chaos with increasing voltage V_0. This indicates that the observed behavior is a property of the e-h plasma and not dependent on the specifics of carrier production; this is consistent with oscillistor experiments[2,3] and theory.[1,4,5]

In general, however, we find that double injection results in more stable and reproducible plasma dynamics. Optical access to the dewar is limited and precise alignment of the laser beam onto the sample is difficult. Further, radiation from the He-Ne laser results principally in surface carrier generation, as well as surface heating. These factors may account for the lack of stability and reproducibility which we have encountered with optically generated e-h plasmas.

The detailed studies of temporal chaos presented in the remainder of this chapter were performed with sample 1A. The spatial data of Chapter IV, as well as the studies of externally driven instabilities of Chapter V, were taken with sample 1E. Much of the material in this chapter has been previously published elsewhere.[6,7,8]

3.2. Period Doubling Route to Chaos

In different regions of parameter space we observe different types of transitions to chaos. Two paths through parameter space will be discussed in this chapter; first, in this section a period doubling route to chaos and, in the next section, a quasiperiodic route. The first sequence was taken with $B_0 = 4$ kGauss as V_0 was increased from 0 to 25 volts. The overall behavior of I(t) was found to be as follows: For $V_0 < 6$ volts, I(t) has only a dc component. At $V_0 = 6$ volts, I(t) spontaneously becomes periodic. Regions of chaotic dynamics occur in the intervals $7.0 \leq V_0 \leq 7.4$ volts; $10.0 \leq V_0 \leq 10.7$ volts; and $14.9 \leq V_0 \leq 18$ volts; otherwise, I(t) is periodic.

The clearest of these three chaotic sequences is shown in figures 3.1 and 3.2. Figure 3.1 shows the unfiltered current I(t) and the unfiltered power spectra $| I(\omega) |^2$ for increasing V_0, while figure 3.2 shows the filtered current I(t), unfiltered phase portraits, V(t) vs. I(t), and the filtered power spectra $| I(\omega) |^2$. Starting in figures 3.1(a) and 3.2(a) at $V_0 = 10.0$ volts, I(t) is oscillating at a fundamental frequency $f_0 \approx 118$ kHz, i.e. at period 1. The power spectrum of figure 3.1(a), as well as the phase portrait of figure 3.2(a), shows

that the oscillation has small spectral components at harmonics of f_0. However, there is no subharmonic component, as seen in the power spectrum of figure 3.2(a). As V_0 is increased, I(t) shows a period doubling bifurcation; the data shown in figures 3.1(b) and 3.2(b) display the emergence of a spectral component at $f_0/2$. At larger V_0 another period doubling bifurcation occurs [figures 3.1(c) and 3.2(c)] with new spectral components at $f_0/4$, $3f_0/4$, $5f_0/4$, . . . At slightly larger V_0, I(t) becomes nonperiodic [figures 3.1(d) and 3.2(d)] and its power spectrum enters a region of broadband "noise". For further increases of V_0 there appear noise-free windows of periods 3, 4, 5, . . . , within this region of broadband noise; see figures 3.1(e) and 3.2(e) for period 3. The sequence ends at $V_0 = 10.7$ volts with a return to period 1 oscillations.

Figure 3.3 is a bifurcation diagram, a plot of the local current maxima $\{ I_{max} \}$ vs. V_0. The period doubling route to chaos, as well as the noise-free windows, can be clearly seen. A similar sequence of windows has been observed in chemical oscillators,[9] driven p-n junctions,[10,11] and finite difference equations.[12]

The broadband "noise" of figures 3.1(d) and 3.2(d) is characteristic of chaotic behavior. The fact that this state is approached through a series of period doublings suggests that the spectral broadening is a result of deterministic nonlinear dynamics. However, to firmly establish that it is not due to some stochastic process, a return map of the current is recorded for the same parameters as figure 3.2(d) and is shown in figure 3.4(a). If the

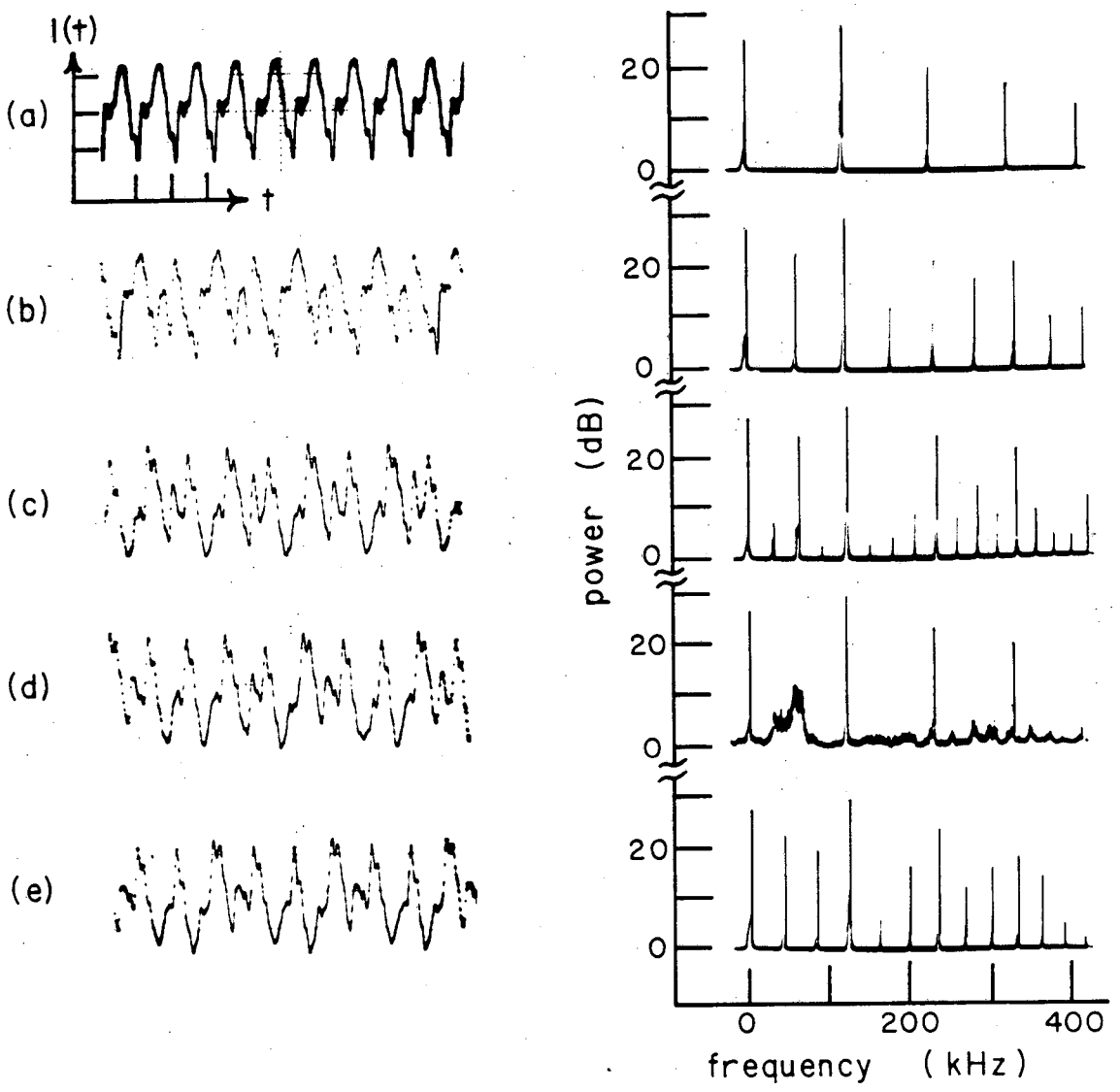

Figure 3.1. Observed period doubling sequence for increasing applied voltage V_0, (a) to (e) [see figure 3.3] for plasma wave in Ge at $B_0 = 4$ kGauss. (a) Unfiltered current I(t) and power spectrum of I(t) show periodic behavior at $f_0 \approx 118$ kHz. (b) Period doubling to $f_0/2$. (c) Period doubling to $f_0/4$. (d) Onset of chaos. (e) Period 3 window. I(t) scales are 8 μs/div and 0.058 mA/div.

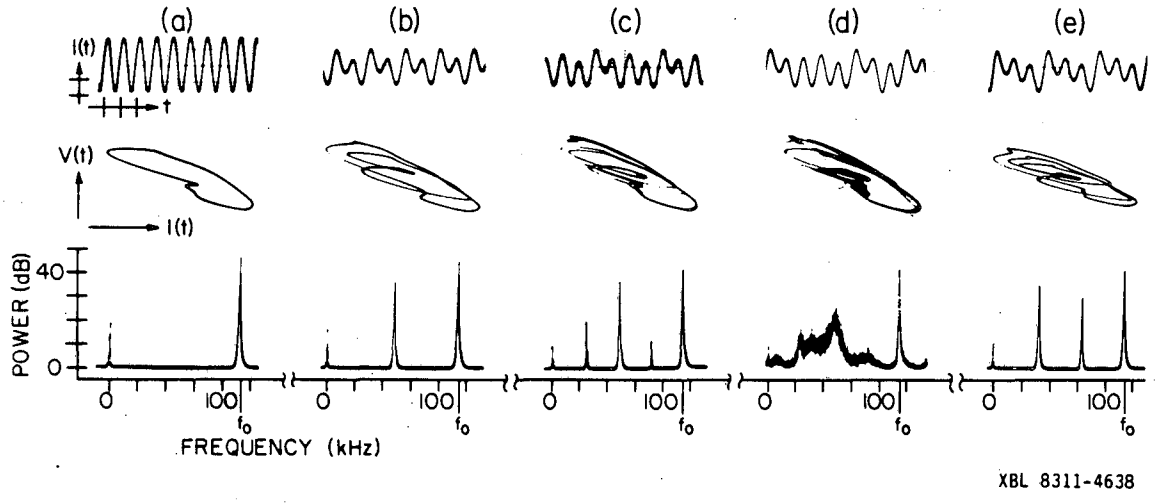

Figure 3.2. Observed period doubling sequence for increasing applied voltage V_0, (a) to (e) [same operating conditions as in figure 3.1] for plasma wave in Ge at $B_0 = 4$ kGauss. (a) Current I(t), phase portrait V(t) vs. I(t), and power spectrum of I(t) show periodic behavior at $f_0 \approx 118$ kHz. (b) Period doubling to $f_0/2$. (c) Period doubling to $f_0/4$. (d) Onset of chaos. (e) Period 3 window. I(t) scales are 8 μs/div and 0.05 mA/div. For time series and power spectra the current was ac coupled and also filtered to remove harmonics of f_0.

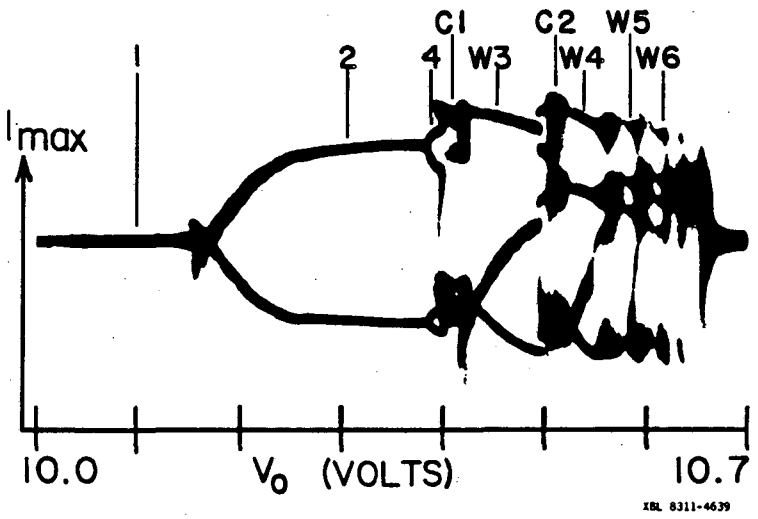

Figure 3.3. Bifurcation diagram of local current maxima I_{max} vs. applied voltage V_0, for same operating conditions as in figure 3.1. Labels (1), (2), (4), (C1) and (W3) refer to regions displayed in figures 3.1(a) to (e), respectively. Labels (W4), (W5) and (W6) refer to noise-free windows of periods 4, 5 and 6, respectively.

broadening of the spectral peaks were due to stochastic noise, then the height of one peak in I(t) would be unrelated to the next, and the return map would be a uniformly filled square area. That this is not the case indicates that the evolution of the system is indeed governed by low-dimensional nonlinear dynamics; i.e., it is chaotic. Return maps of the current recorded for the nonperiodic regimes following the period 3, 4, and 5 noise-free windows are shown in figures 3.4(b), (c) and (d), respectively; we observe from the return maps that all of these states are also chaotic.

3.3. Quasiperiodic Route to Chaos

The second type of transition which we have observed is the quasiperiodic route to chaos: as V_0 is increased, the onset of a quasiperiodic state is followed by a transition to chaos. One such sequence of power spectra, taken at $B_0 = 11.15$ kGauss, is shown starting in figure 3.5(a) with $V_0 = 2.865$ volts: I(t) is spontaneously oscillating at a fundamental frequence $f_1 = 63.4$ kHz. At $V_0 = 2.907$ volts, the system becomes quasiperiodic: a second spectral component appears at $f_2 = 14$ kHz, incommensurate with f_1 [figure 3.5(b)]. At $V_0 = 2.942$ volts, the system is still quasiperiodic; however, the two modes are interacting and the nonlinear mixing gives spectral peaks at the combination frequencies $f = mf_1 + nf_2$, with m,n positive and negative integers.

As V_0 in increased further, we observe a series of frequency lockings[13],

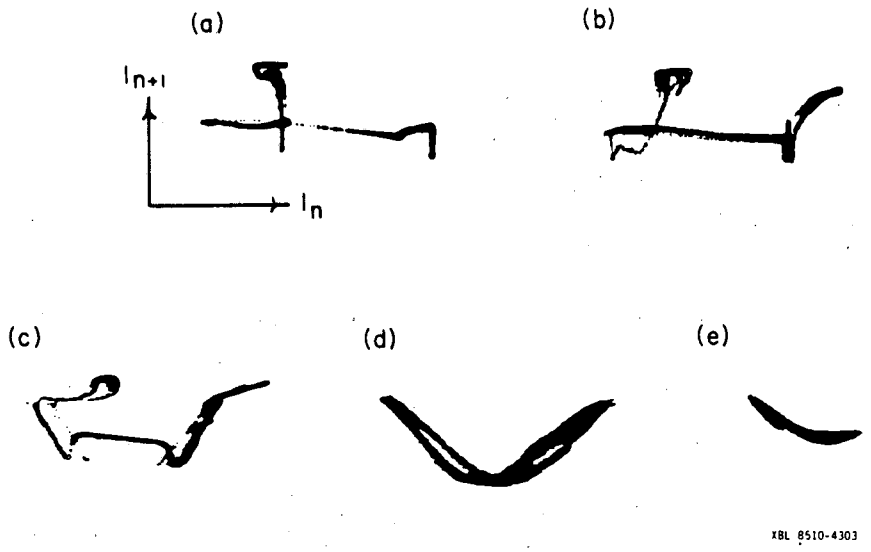

Figure 3.4. Return maps, I_{n+1} vs. I_n, where $\{ I_n \}$ is the set of local current maxima for increasing V_0, (a) to (e), and same operating conditions as in figure 3.1. (a) Chaos following period doubling cascade [region (C1) of figure 3.3]. (b) Chaos following period 3 window [region (C2) of figure 3.3]. (c) Chaos following period 4 window. (d) Chaos following period 5 window. (e) Chaos following period 6 window, just prior to return to period 1.

i.e., (f_1/f_2) = rational number, until the onset of chaos is reached, indicated by a slight broadening of the spectral peaks [figure 3.5(d)]. As V_0 is increased further, the e-h plasma exhibits increasingly turbulent behavior [figures 3.5(e) and (f)]. This is followed by a return to quasiperiodicity at $V_0 = 3.125$ volts and, subsequently, simple periodicity at $V_0 = 3.442$ volts.

Figure 3.5 also shows a sequence of return maps, topologically equivalent to Poincaré sections.[14] Periodic motion corresponds to a closed 1-dimensional orbit in phase space; the Poincaré section in this case is simply a point [figure 3.5(a)]. Similarly, when the system is quasiperiodic, corresponding to motion on a 2-dimensional torus, the Poincaré section is approximately a circle [figures 3.5(b) and (c)]. However, as the system becomes chaotic, we find that the Poincaré section begins to wrinkle and to occupy an extended region. This does not *necessarily* imply that the behavior is stochastic, but rather that the dimension of the strange attractor (which is one greater than the dimension of the Poincaré section) is too large to be determined by visual inspection of the Poincaré section. For these attractors the fractal dimension must be calculated quantitatively, as discussed in the following section.

3.4. Calculations of Fractal Dimensions

The fractal dimension is a measure of the number of "active" degrees of freedom needed to characterize the evolution of a system (see Chapter I). If this evolution is described by trajectories in a G-dimensional phase space,

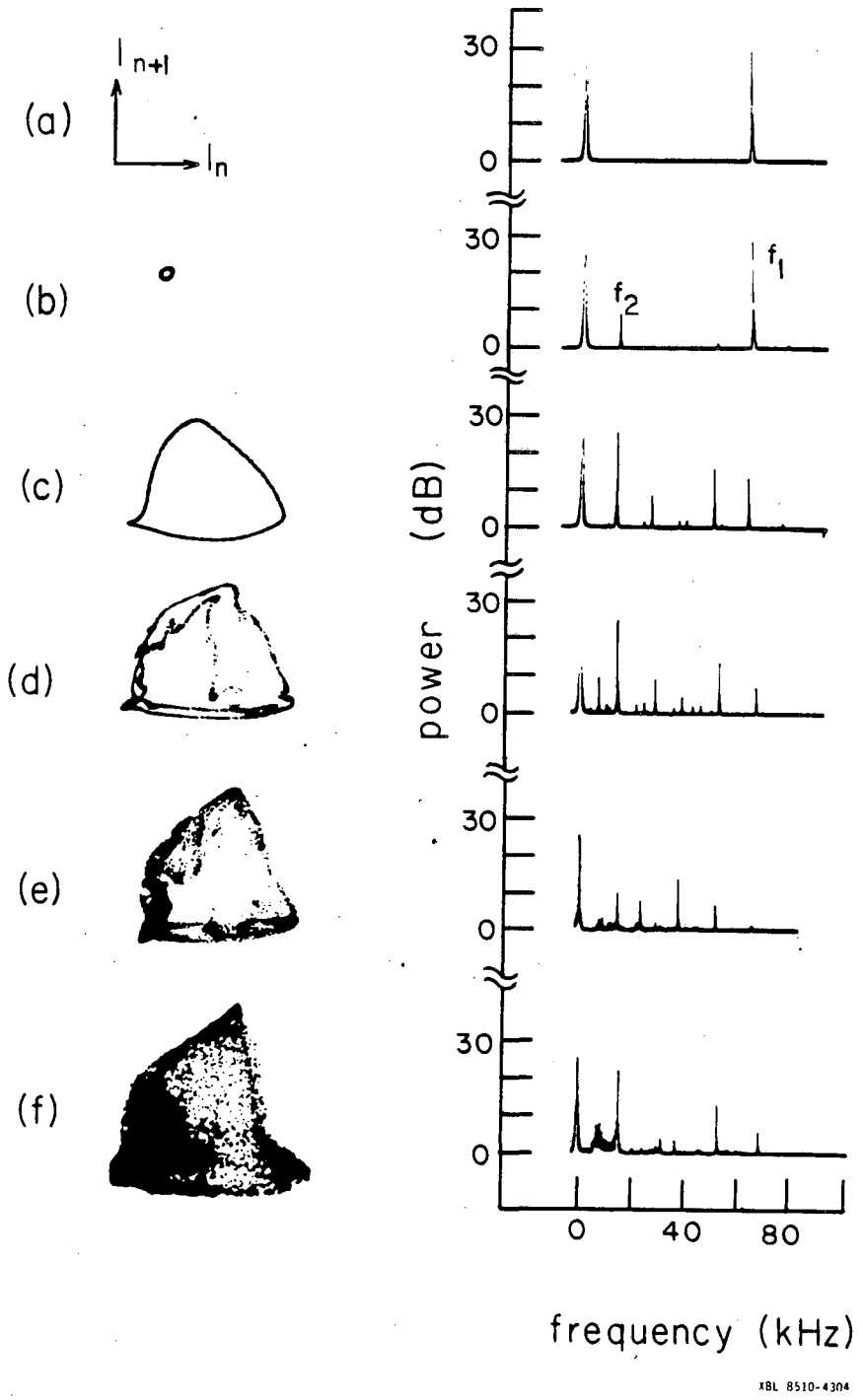

Figure 3.5. Return maps, I_n vs. I_{n+1} (where $\{ I_n \}$ is the set of local current maxima), and power spectra of the plasma current I(t) at $B_0 = 11.15$ kGauss with increasing V_0: (a) 2.865 volts, periodic at $f_1 = 63.4$ kHz. (b) 2.907 volts, quasiperiodic with second frequency $f_2 = 14$ kHz. (c) 2.942 volts, quasiperiodic with combination frequency components. (d) 3.016 volts, onset of chaos. (e) 3.033 volts, chaotic. (f) 3.058 volts, more chaotic; the fractal dimension of this attractor, $d = 2.7$, is measured in figure 3.7.

then the fractal dimension d_F is defined as follows:[15]

$$d_F = \lim_{\delta \to 0} \frac{\log M(\delta)}{\log (1/\delta)} \tag{3.1}$$

where the phase space has been partitioned into cubes of volume δ^G and $M(\delta)$ is the number of these cubes visited by the attractor.[16] This measure is known variously as the capacity, Hausdorff dimension, and fractal dimension. Other, alternative, dimensions which characterize strange attractors have also been devised. These include the information dimension d_I,[15] and the correlation dimension d_C.[17] It has been proven[18] that generally $d_F > d_I > d_C$. However, in most cases where these dimensions have been calculated, all three have yielded almost identical results.[17,19,20,21]

Equation (3.1) assumes an attractor contained within a G-dimensional phase space. The coordinates of the phase space may be any set of variables which, when taken together, uniquely identify the state of the system. For our experiments, these variables could be the plasma density and momentum measured at many different points within the crystal (provided of course that the number of independent probes G were greater than the fractal dimension d). Experimentally, this method of characterizing the system is difficult to realize. It is not always feasible to have an arbitrary number of probes for a given system and, further, it is not known how many probes will be required. One cannot know this until the fractal dimension d_F has already been determined.

Fortunately, there is a method of reconstructing phase space from a single dynamical variable using a technique based on the embedding theorem.[17,19,22,23] If $\{ V_1(t), V_2(t), \ldots, V_G(t) \}$ is a phase space constructed from G independent variables, then the reconstructed phase space $\{ V_1(t), V_1(t+\tau), \ldots, V_1(t+(D-1)\tau) \}$ is conjectured to be topologically equivalent to the original phase space, for almost all τ, provided $D > 2G+1$.[22] Attractors in both the original and reconstructed phase spaces will be characterized by the same Lyapunov exponents and fractal dimensions. In our experiments, we use a reconstructed phase space derived from the measured current I(t). The coordinates of our phase space are thus $\{ I(t), I(t+\tau), \ldots, I(t+(D-1)\tau) \}$, where, typically, $5\ \mu s < \tau < 15\ \mu s$; we find that the calculated fractal dimensions are independent of τ. In practice, one calculates the fractal dimension d for increasing embedding dimension D until d converges with respect to D.

Calculations of fractal dimensions using the box-counting algorithm of equation (3.1) tend to be computationally inefficient.[24] Large regions of phase space are visited only rarely. Thus large numbers of data points and, consequently, large amounts of computer time are often required. Calculations on systems with $d \approx 3$ can require more than a million data points. However, it is possible to calculate the "pointwise" fractal dimension[25] (which is conjectured[15] to be equal to the information dimension) using the following, more efficient algorithm.[26] A D-dimensional phase space is reconstructed from a single dynamical variable. Next one computes the number of points on an

attractor, N(ϵ), which are contained within a D-dimensional hypershpere of radius ϵ centered on a randomly selected point on the attractor. One expects scaling of the form:

$$N(\epsilon) \propto \epsilon^{d} \tag{3.2}$$

where d is the fractal dimension of the attractor. Thus a plot of log$N(\epsilon)$ vs. logϵ is expected to have slope d (for sufficiently small ϵ). This procedure is carried out for consecutive values of D = 2, 3, 4, . . . , until the slope has converged. This is done to insure that the embedding dimension chosen is sufficiently large (important if the dimension of the phase space is not known) and to discriminate against high dimensional stochastic noise, not of known deterministic origin.

A comparison of equations (3.1) and (3.2) illustrates the difference between the fractal and pointwise dimensions. The calculation of the fractal dimension involves determining the fraction of phase space occupied by the entire attractor. On the other hand, the pointwise dimension is defined as the scaling of N(ϵ) with ϵ, for N(ϵ) centered around a *single* point on the attractor. The conjecture that the pointwise dimension is equal to the information dimension (which, like the fractal dimension, is measured globally over the attractor[15]) implies that the scaling laws which govern the fractal structure are constant throughout the attractor. It is therefore sufficient to determine the scaling exponent at a single point on the attractor. We note that the pointwise dimension is conjectured to be equal to the information dimension,

not the fractal dimension, but, as mentioned earlier, the two are found to be experimentally indistinguishable.

We have computed the pointwise dimension d for our plasma instabilities at various points along the quasiperiodic transition to chaos described in section 3.3. For each of eleven values of V_0 between 2.865 volts and 3.125 volts ($B_0 = 11.15$ kGauss) we recorded N (≈ 98000) successive values of the current at 5 μs intervals [i.e., $I_n = I(t+n\tau)$, $n = 1, \ldots, 98000$; $\tau = 5\ \mu s$]. From each data set $\{I_1, \ldots, I_N\}$ we constructed $N - D + 1$ vectors $\mathbf{G}_n \equiv (I_n, I_{n+1}, \ldots, I_{n-D+1})$ in a D-dimensional phase space. In principle, one should be able to calculate the fractal dimension with equation (3.2) using data centered around a single point on the attractor $\mathbf{G}_n$; that is, calculations of $N(\epsilon)$ centered around different vectors $\mathbf{G}_i$ should all yield the same value of d.[19] Experimentally this is not actually observed, as discussed below.

For $V_0 = 3.058$ volts we constructed plots of $\log N(\epsilon)$ vs. $\log\epsilon$ for $N(\epsilon)$ centered on 27 randomly selected vectors $\mathbf{G}_i$. The slopes of these 27 plots comprise 27 measurements of the fractal dimension d. A histogram of these values of d is shown in figure 3.6(a); the result is a distribution centered around $d = 2.4 - 2.6$. However, a careful examination of the 27 plots of $\log N(\epsilon)$ vs. $\log\epsilon$ indicates that several of these plots yield unreliable values of d, for reasons discussed below. Upon elimination of these suspect points, the width of the histogram narrows appreciably, as shown in figure 3.6(b). For an experimental system, there are at least two conditions under which one will not expect scaling of the form of equation (3.2) for $N(\epsilon)$ centered around

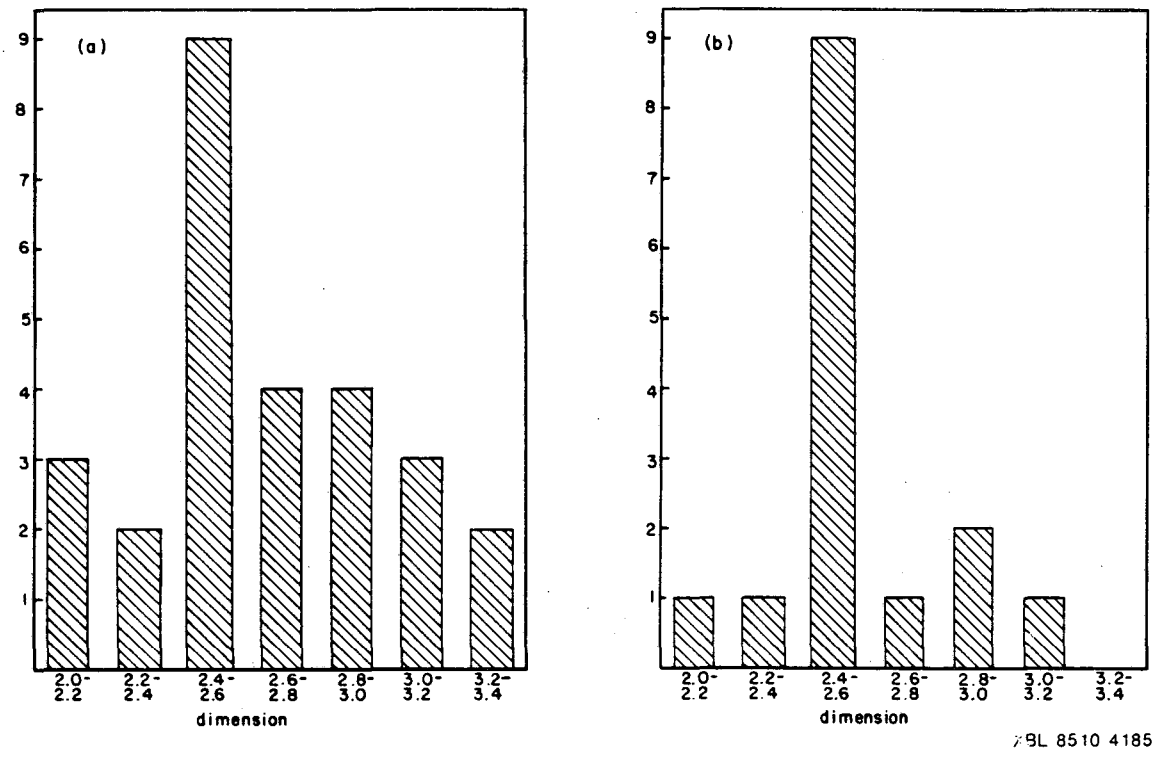

Figure 3.6. Histogram of fractal dimension calculations for $V_0 = 3.058$ volts and $B_0 = 11.15$ kGauss [same operating conditions as in figure 3.5(f)]. (a) The fractal dimension is calculated 27 times by observing the scaling of $N(\epsilon)$ [equation (3.2)] around 27 randomly chosen points in reconstructed phase space. The vertical axis refers to the number of these calculations for which the fractal dimension d is found to be in each of the ranges specified on the horizontal axis. The distribution is centered around d = 2.4 - 2.6. (b) The same distribution as (a), except that those calculations yielding unphysical results (see text) have been removed. The distribution is still centered at d = 2.4 - 2.6, but it has narrowed appreciably.

certain random points on the attractor.

First, the random point may be situated in a region of the attractor which is visited only rarely. Thus, even with a large number of data points there are not enough nearby data points to resolve the fractal structure and thus to observe the scaling of equation (3.2). In such a case, the plot of $\log N(\epsilon)$ vs. $\log\epsilon$ will have a gradually increasing slope for small ϵ, in contrast with the break to a steeper, non-convergent slope for small ϵ that is expected for chaotic systems in the presence of thermal noise.[27] This break is expected because the dynamics of all physical systems are characterized by thermal (stochastic) processes at energies below $\sim$kT; these processes are characterized by fractal dimensions on the order of the number of particles in the system.[28] We eliminate all plots which do not show the physically expected break to steeper slope for small ϵ.

A second difficulty arises when $N(\epsilon)$ is centered in a region of the attractor where the length scales over which the structure is fractal are comparable to or less than those corresponding to thermal fluctuations ($\sim$kT). In these cases the fractal structure may be "washed out" by thermal noise, resulting in a plot of $\log N(\epsilon)$ vs. $\log\epsilon$ which does not have a well defined (convergent) slope. We discard these plots as well.

By rejecting those plots of $\log N(\epsilon)$ vs. $\log\epsilon$ which do not exhibit physically reasonable characteristics (i.e., a well defined slope and a break to steeper slope for small ϵ), we obtain a much sharper distribution of values for the fractal dimension d, as seen in figure 3.6(b). However, when we plot

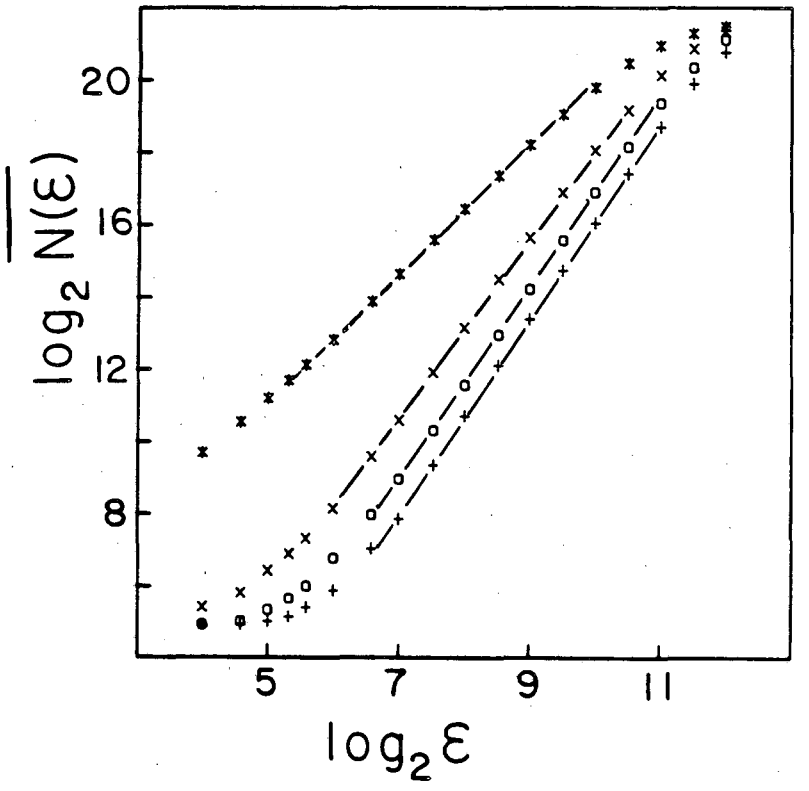

Figure 3.7. Plots of $\log\overline{N(\epsilon)}$ vs. $\log\epsilon$ used to determine the fractal dimension d of the chaotic attractor at $V_0 = 3.058$ volts, $B_0 = 11.15$ kGauss, using method discussed in text and equation (3.2) [averaged over 25 randomly chosen points in reconstructed phase space]. Embedding dimension $D = 2, 4, 6$ and 8 correspond, respectively, to symbols *, x, o and +; for $D \geq 6$, the slope converges to $d = 2.7$.

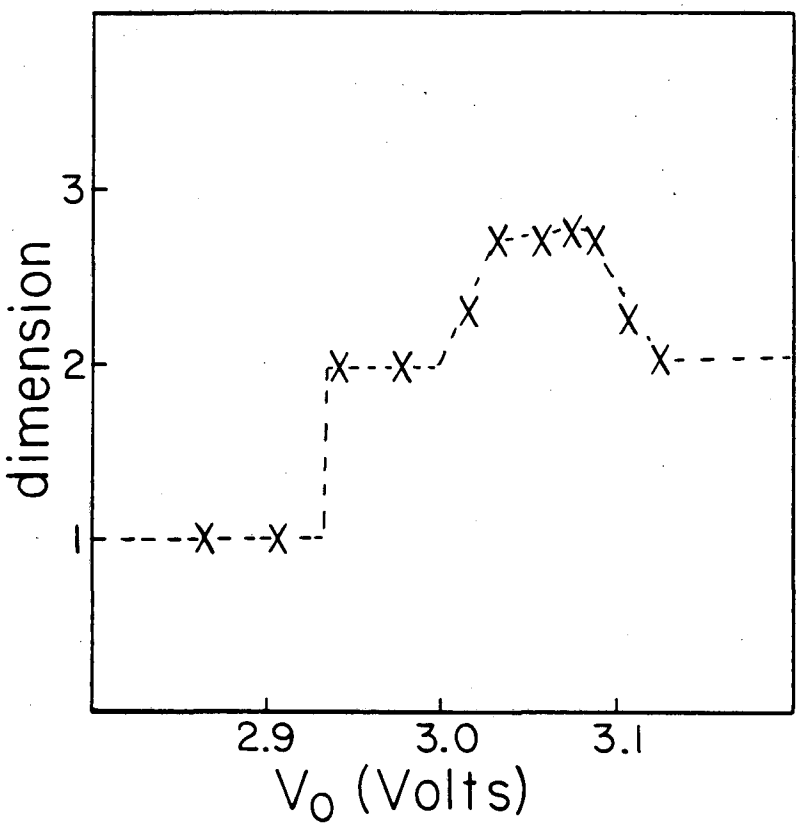

Figure 3.8. Dependence of measured dimension d on applied voltage V_0. $B_0 = 11.15$ kGauss. Values $d = 1$ and $d = 2$ correspond to periodic and quasiperiodic orbits, respectively. All calculations were checked for convergence with respect to embedding dimension D and number of data points sampled N. All values of d represent an average over 25 randomly selected points in reconstructed phase space.

$\log\overline{N(\epsilon)}$ vs. $\log\epsilon$, where $\overline{N(\epsilon)}$ is the average over many hyperspheres, we find that this average slope is unchanged ($\pm 5\%$) by the rejection of the unphysical plots. This was found to be true for several cases. Thus, in most instances we simply plot $\log\overline{N(\epsilon)}$ vs. $\log\epsilon$ for $\overline{N(\epsilon)}$ averaged over many randomly chosen hyperspheres. (This same procedure has also been utilized in studies of free surface modes of a vertically forced fluid layer[29] and Couette-Taylor flows.[19]) Figure 3.7 shows our results for $V_0 = 3.058$ volts with the embedding dimension D = 2,4,6, and 8; for $D \geq 6$ the slope (and thus the fractal dimension) has converged to 2.7. The fractal dimension for all the states shown in figure 3.5, as well as several states not shown, are plotted in figure 3.8.

Within the chaotic regime, the fractal dimension of the attractor varies between 2 and 3. This demonstrates that the observed plasma turbulence shown in figures 3.5(d)-(f) may be described with only a few degrees of freedom; the behavior of the system remains largely deterministic. If the observed turbulence were due to thermal or stochastic processes, then a measurement of the fractal dimension d would not have converged for small embedding dimension D. The dimension of the attractor d could then have been on the order of the number of conduction electrons and holes in the crystal[28] ($\approx 10^{10}$).

References. Chapter III

1. C. E. Hurwitz and A. L. McWhorter, Phys. Rev. **134**, A1033 (1964).

2. R. D. Larrabee and M. C. Steele, J. Appl. Phys. **31**, 1519 (1960).

3. R. D. Larrabee, J. Appl. Phys. **34**, 880 (1963).

4. M. Glicksman, Phys. Rev. **124**, 1655 (1961).

5. M. Shulz, Phys. Status Solidi **25**, 521 (1968).

6. G. A. Held, C. Jeffries and E. E. Haller, Phys. Rev. Lett. **52**, 1037 (1984).

7. G. A. Held, C. Jeffries and E. E. Haller in *Proceedings of the Seventeenth International Conference on the Physics of Semiconductors, San Francisco, 1984,* edited by D. J. Chadi and W. A. Harrison (Springer-Verlag, New York, 1985), p. 1289.

8. G. A. Held and C. D. Jeffries to appear in *Proceedings of the International Symposium on Synergetics at Schloss Elmau, Bavaria, 6-11 May, 1985,* edited by H. Haken (Springer-Verlag).

9. J. S. Turner, J. C. Roux, W. D. McCormick and H. L. Swinney, Phys. Lett. **85A**, 9 (1981).

10. J. Perez, C. Jeffries, and J. Testa, Bull. Am. Phys. Soc. **28**, 383 (1983).

11. S. D. Bronson, D. Dewey and P. S. Linsay, Phys. Rev. **A 28**, 1201 (1983).

12. Jose Perez, Ph.D. Thesis, University of California, Berkeley, 1983; J. Perez, to appear in Phys. Rev. **A**; A. S. Pikovsky, Phys. Lett. **85A**, 13 (1981).

13. for example, J. P. Gollub and S. V. Benson in *Pattern Formation and Pattern Recognition* edited by H. Haken (Springer-Verlag, Berlin, 1979), p. 74.

14. N. H. Packard, J. P. Crutchfield, J. D. Farmer and R. S. Shaw, Phys. Rev. Lett. **45**, 712 (1980).

15. for example, J. D. Farmer, E. Ott, J. A. Yorke, Physica (Utrecht) **7D**, 153 (1983).

16. Unconventional notation is used in equation (3.1) to avoid confusion with the notation of equation (3.2).

17. P. Grassberger and I. Procaccia, Phys. Rev. Lett. **50**, 346 (1983).

18. H. G. E. Hentschel and I. Procaccia, Physica **8D**, 435 (1983).

19. A. Brandstäter *et al.* , Phys. Rev. Lett. **51**, 1442 (1983).

20. H. L. Swinney and J. P. Gollub, to appear in Physica **D**.

21. This has been observed in calculations of fractal, information and correlation dimensions for a system consisting of a driven p-n junction in series with an inductor and a resistor. G. A. Held and C. Jeffries, unpublished.

22. F. Takens in *Lecture Notes in Mathematics 898,* edited by D. A. Rand and L. S. Young (Springer-Verlag, Berlin, 1981), p. 366.

23. for example, H. L. Swinney, Physica (Utrecht) **7D**, 3 (1983).

24. H. S. Greenside, A. Wolf, J. Swift and T. Pignaturo, Phys. Rev. **A 25**, 3453 (1982).

25. The pointwise dimension is defined in reference 15. Similar definitions of dimension have been given in references 11, 20, 21, and 31 therein.

26. This is the method used by A. Brandstäter *et al.* , in reference [19]. See also reference [17].

27. A. Ben-Mizrachi, I. Procaccia and P. Grassberger, Phys. Rev. **A 29**, 975 (1984).

28. A fractal dimension of this magnitude ($\sim 10^{10}$) is experimentally unattainable for two reasons. First, an inordinate number of data points would be required, as discussed in Chapter IV. Second, one would need to measure signals with a very large bandwidth $\Delta f \sim 1/\tau$, where τ is the shortest fluctuation time; typically $\Delta f \sim 10^9 - 10^{14}$ Hz for stochastic noise in conducting media. Thus, fractal dimensions of this magnitude are operationally meaningless.

29. S. Ciliberto and J. P. Gollub, J. Fluid Mech. **158**, 381 (1985).

CHAPTER IV. RESULTS: SPATIAL BEHAVIOR

4.1. Introduction

It is well established that the onset of turbulence in a wide range of physical systems can be characterized by temporal chaos.[1] That is, the evolution of these systems corresponds to motion in phase space along trajectories which are confined to a strange (fractal) attractor.[2] However, the relationship between low-dimensional chaos and spatial complexity is less well understood. Both experimental[3] and theoretical[4] continuum systems have been shown to exhibit temporally chaotic, spatially coherent behavior. However, there is as yet no clear experimental data on a system in which the breakup of spatial order can be characterized by low-dimensional chaotic dynamics. In this chapter we present the results of experiments on the spatial and temporal dynamics of chaotic instabilities in an electron-hole (e-h) plasma in Ge. Much of the material in this chapter has been previously published elsewhere.[5,6]

In Chapter III we established that helical e-h plasma instabilities do indeed exhibit chaos. We now turn out attention to the question of spatial coherence within the instabilities. In particular, we would like to determine whether the observed chaotic states correspond to a temporally chaotic yet still spatially coherent helical plasma density wave or whether the onset of temporal chaos could also correspond to a breakup of spatial order within the

density wave. By placing probe contacts along the length of our sample (see Chapter II), we are able to monitor the local variations in plasma density. We have found two distinct types of behavior: (i) an essentially spatially coherent and temporally chaotic plasma density wave characterized by an attractor of measured fractal dimension $d \sim 3$, and (ii) a spatially incoherent wave with an unmeasurably large fractal dimension $d > 8$. Further, as the applied electric field E_0 is increased, we observe a transition between these two states – characterized by a partial loss of spatial order and a jump in fractal dimension. While the increase in fractal dimension from $d \sim 3$ to $d > 8$ is somewhat abrupt ($\Delta E_0/E_0 \sim 0.05$), the breakup of spatial order occurs gradually. It is physically reasonable that the onset of spatial incoherence (which increases the number of available degrees of freedom) would result in an increased fractal dimension. However, we cannot firmly establish that the onset of spatial disorder is *coincident* with the observed jump in fractal dimension: the possibility that these two events occur at comparable applied fields and yet are not directly related cannot be competely excluded.

4.2. Transitions to "Weak" Turbulence

In different regions of parameter space (V_0, B_0, θ) different types of transitions to turbulence are observed. For our system we make the operational definition that a transition to "weak" turbulence is one in which the transition from periodicity to chaos is followed by a transition back to periodicity as V_0 is increased further. All such transitions that we have observed occur

over a small range (i.e., $\sim$1 volt) of V_0, and in all such chaotic states there exists at least one fundamental peak which stands out clearly above the broadband "noise" level of the power spectrum. The scenarios reported in Chapter III, period doubling and quasiperiodic transitions to chaos, were in parameter space regions corresponding to transitions to weak turbulence.

The transition to weak turbulence which we consider here (taken with B_0 = 11.15 kGauss) is periodic at V_0 = 5.50 volts, quasiperiodic at V_0 = 5.59 volts, and chaotic at V_0 = 5.71 volts. The power spectra and return maps (which are topologically equivalent to Poincaré sections[7]) for these three states are shown in figure 4.1. The structure within the return map at V_0 = 5.71 volts strongly infers that the system is in a low-dimensional chaotic regime, and calculations of the fractal dimension confirm this. Following the procedures of Chapter III, we find the fractal dimension d of our plasma instability to be 1, 2, and 2.7 for the above periodic, quasiperiodic, and chaotic states, respectively.

To determine whether or not a weakly turbulent state is spatially coherent, we compare fluctuations in plasma density at different points along the sample. We obtain a crude measure of the degree of coherence by using a fast two-channel Tektronix 468 digital storage oscilloscope and comparing the voltages $V_i(t)$ across pairs of contacts located at different positions along the z-axis of the sample. If the temporal behavior of I(t) is periodic, we observe only a phase shift in $V_i(t)$ along z, which indicates a coherent travelling wave.

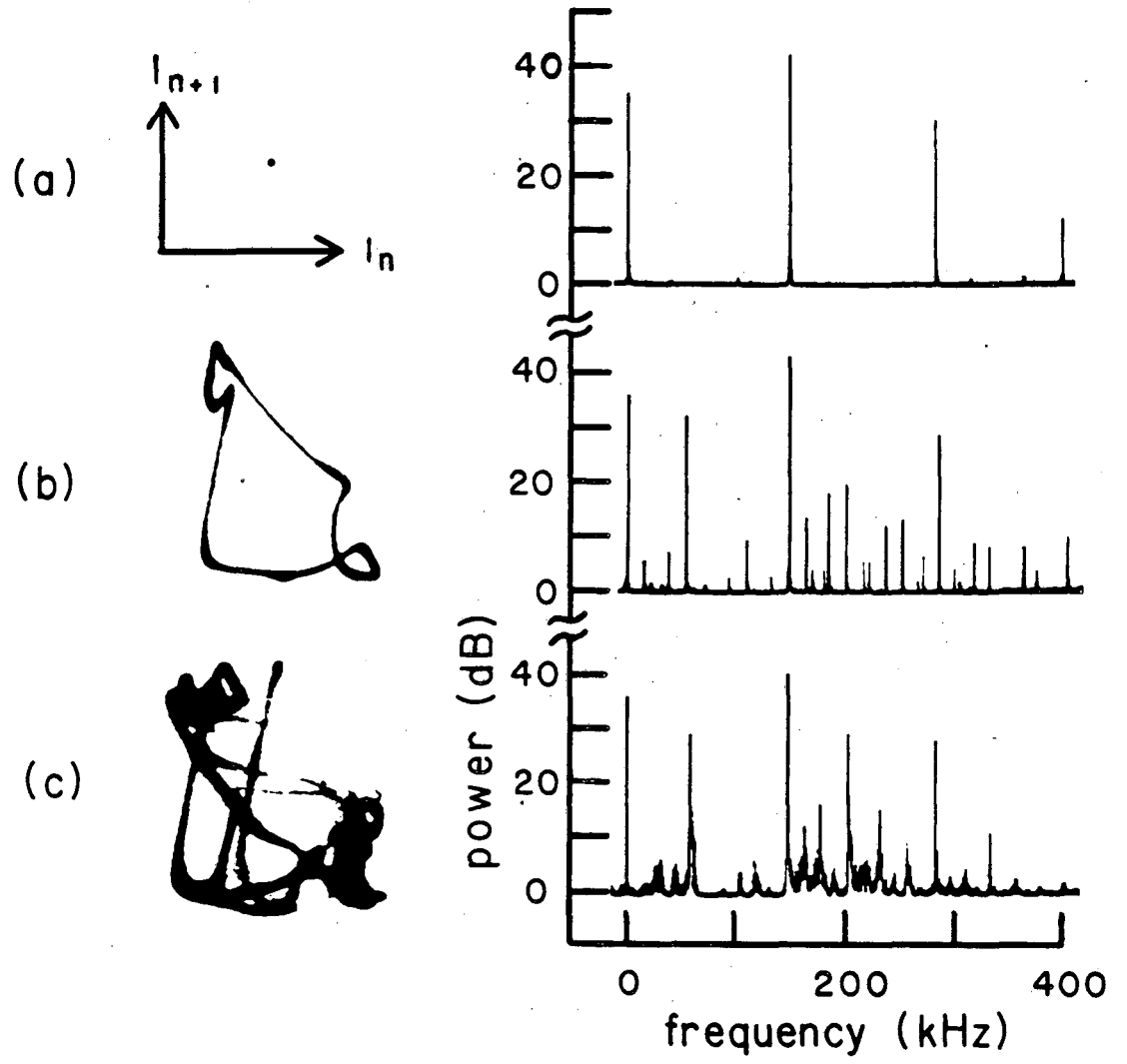

Figure 4.1. Poincaré sections, I_n vs. I_{n+1} (where $\{ I_n \}$ is the set of local current maxima), and power spectra of the total current I(t) at $B_0 = 11.15$ kGauss with increasing V_0: (a) 5.50 volts, periodic at $f_0 = 147$ kHz. (b) 5.59 volts, quasiperiodic. (c) 5.71 volts, chaotic. I(t) is ac coupled and filtered to remove harmonic distortion.

To obtain a more quantitative measure of the degree of spatial coherence, applicable for nonperiodic behavior, we calculate a spatial correlation function, C(r), defined as[8]

$$C(r) = \left| \frac{2}{N} \sum_{n=1}^{N} V_i(n\tau) V_j(n\tau) \right|^{1/2}, \tag{4.1}$$

where $V_i(t)$ and $V_j(t)$ are the voltages across two pairs of contacts separated by a distance r, τ is the sampling interval, and N is a number large enough that C(r) has converged, typically 20000. We find that C(r) is independent of τ.

For the periodic parameters above, the correlation function C(r) for different spacings r between the pairs of probe contacts is plotted in figure 4.2. For each pair of contacts, the voltage difference $V_i(t)$ is periodic. By noting the phase shift between pairs of probes as a function of distance, we estimate that the spatial wavelength is $\lambda \approx 4.9$ mm. The theoretical correlation function for a travelling wave,

$$S(r) = \left[\frac{2}{T} \int_0^T \sin(\omega t) \sin t(\omega t - 2\pi r/\lambda) dt \right]^{1/2}, \tag{4.2}$$

is also shown if figure 4.2; the periodic data points lie close to the theoretical curve. We believe that the observed deviations from theory are due to the harmonic components of the density wave, $2f_0$, $3f_0$, etc. {which are seen experimentally [figure 4.1(a)] but are not included in equation (4.2)} and, possibly, to variations in probe sensitivity as well. Thus we conclude that the periodic

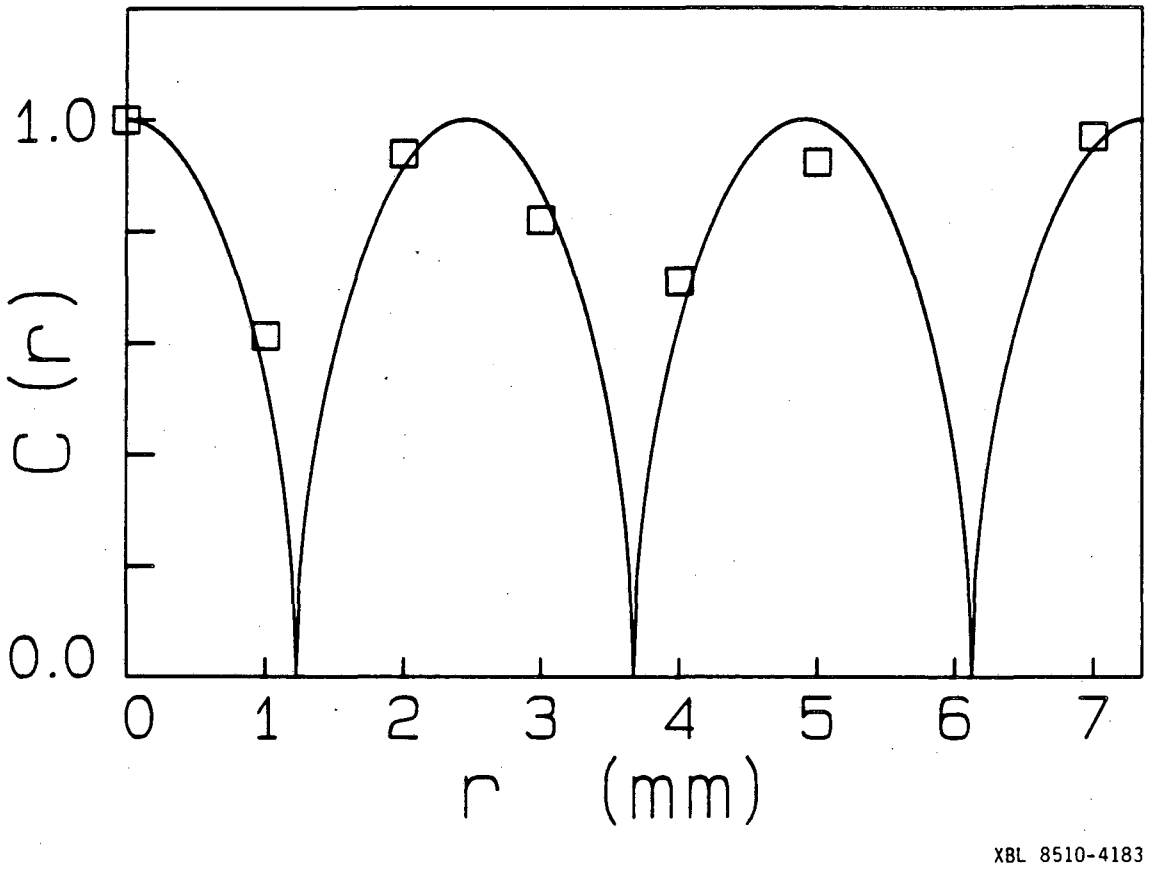

Figure 4.2. Comparison of measured values (□) of spatial correlation function, C(r), equation (4.1), with theoretical correlation function, S(r), equation (4.2), computed for $\lambda = 4.9$ mm (solid line). Data were taken for periodic state at $B_0 = 11.15$ kGauss, $V_0 = 5.50$ volts using voltages from pairs of side probes separated by distance r. C(r) is normalized such that $C(r = 0) = S(r = 0) = 1$.

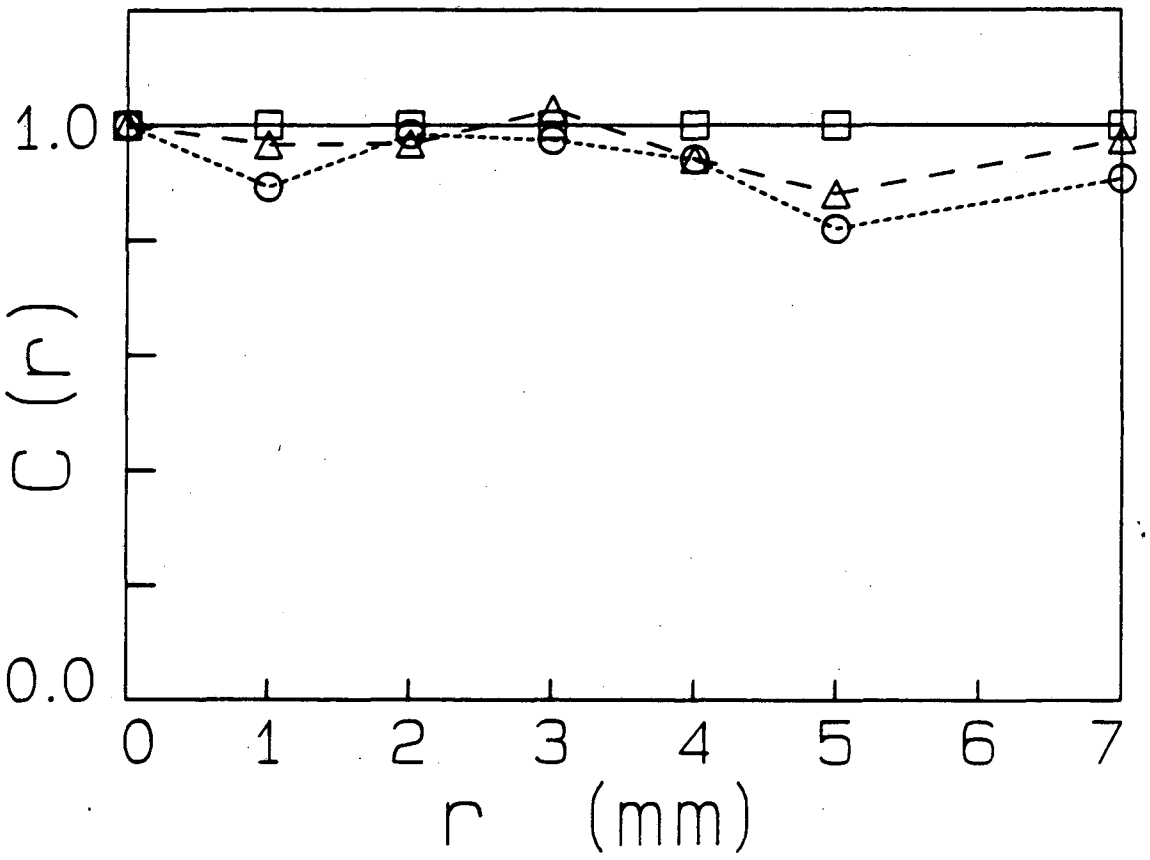

Figure 4.3. Normalized comparison of measured values of spatial correlation function C(r) for three data sets at $B_0 = 11.15$ kGauss: (□) periodic, $V_0 = 5.50$ volts; (Δ) quasiperiodic, $V_0 = 5.59$ volts; (o) chaotic, $V_0 = 5.71$ volts. The periodic, quasiperiodic, and chaotic correlation functions are each normalized such that $C(r = 0) = 1$. For each r, the ratios $C_{quasiperiodic}(r)/C_{periodic}(r)$ and $C_{chaotic}(r)/C_{periodic}(r)$ are then plotted as Δ and o, respectively. The ratio $C_{periodic}(r)/C_{periodic}(r)$ is plotted as □ for reference.

oscillations are spatially coherent -- not surprising and consistent with previous experimental work.[9,10] In figure 4.3 we plot experimental correlation functions C(r) for the quasiperiodic ($V_0 = 5.59$ volts) and chaotic ($V_0 = 5.71$ volts) states. In these plots, C(r) for the periodic data has been normalized to unity at each distance r, and the quasiperiodic and chaotic data have been scaled accordingly (see figure caption). We find that the quasiperiodic and chaotic states both have correlation functions which approximately follow the periodic case. Therefore, we conclude that this weakly turbulent instability exhibits temporal chaotic behavior while remaining essentially a spatially coherent plasma density wave.

4.3. Transitions to "Strong" Turbulence

With sufficiently large applied electric and magnetic fields, we find that we can drive the plasma into a turbulent state from which it will not become periodic again as V_0 is increased further. Instead, all of the frequency peaks in the power spectrum merge into a single, broad, noiselike band. We classify this as a transition to "strong" turbulence. Such a transition is shown in figure 4.4. At $V_0 = 10.4$ volts, I(t) is simply periodic at $f_0 = 321$ kHz, with higher harmonics present as well [figure 4.4(a)]. At $V_0 = 11.6$ volts, I(t) is quasiperiodic and at $V_0 = 12.1$ volts (not shown), the onset of broadband "noise" can be observed. At $V_0 = 13.8$ volts [figure 4.4(b)], only a few of the peaks can be seen above the noise, and when $V_0 = 21.8$ volts [figure 4.4(c)], only a very broad peak remains.

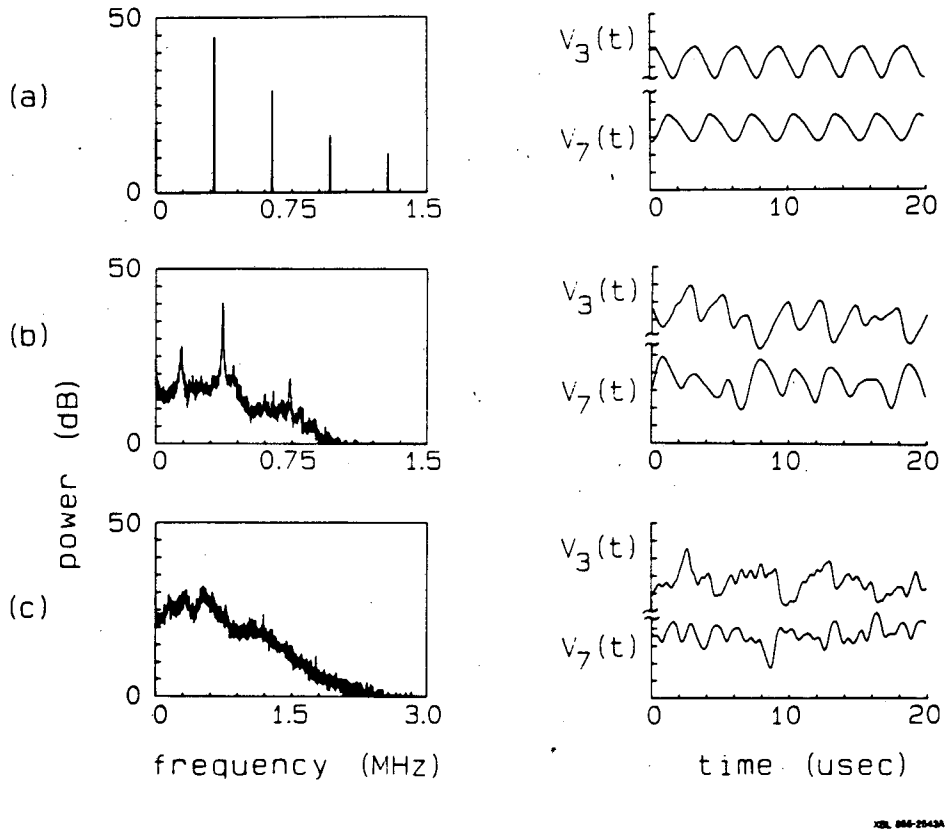

Figure 4.4. Left, measured power spectra of I(t); right, measured voltages for two pairs of probe contacts separated by r = 4 mm: $V_3(t)$ and $V_7(t)$ correspond to probe pairs located 3 and 7 mm away from the p^+ contact, respectively. $B_0 = 11.15$ kGauss. (a) $V_0 = 10.4$ volts, periodic at $f_0 = 321$ kHz. At $V_0 = 12.1$ volts (not shown) temporal chaos has set in, with measured fractal dimension $d \approx 2.5$, figure 4.7(a). (b) $V_0 = 13.8$ volts, power spectrum has broad base and peaks; comparison of $V_3(t)$ and $V_7(t)$ shows beginning of spatial incoherence; measured fractal dimension $d > 8$. (c) $V_0 = 21.8$ volts, power spectra very broad, more marked loss of spatial coherence, measured fractal dimension $d > 8$.

We find that this transition to strong turbulence is characterized by a partial loss of spatial coherence. In the right hand column of figure 4.4, we plot the voltage traces across two pairs of probe contacts which are separated by r = 4 mm, for V_0 = 10.4, 13.8, and 21.8 volts. In the periodic case, the wave is spatially coherent with a wavelength of approximately 8 mm (i.e., a 4 mm separation corresponds to a 180° phase shift). At V_0 = 13.8 volts we are just beyond the onset of the break-up of spatial order -- the basic oscillatory pattern and the 180° phase shift are approximately maintained between the two traces, but changes in the shapes and spacings of the peaks can also be observed. For V_0 = 21.8 volts, the wavelike structure of the traces, as well as the readily observable spatial correlation are no longer present.

In figure 4.5 we plot C(r) for the periodic case V_0 = 10.4 volts; the data points lie close to the theoretical line S(r) for λ = 7.7 mm. However, for data at higher V_0 we have not found a correlation function of analytic form which fits the data, in contrast to the weakly turbulent data of figure 4.3. Nonetheless, we are able to draw some conclusions from the correlation function data at higher voltages.

Plots of C(r = 4 mm) and C(r = 7 mm) are found to decrease monotonically with V_0, as shown in figure 4.6. Further, voltage traces across two pairs of probe contacts which are separated by r = 1 mm are found to have almost identical waveshapes, except for a small (and expected) phase shift, for all values of V_0 studied. Thus, we may *approximately* assume that any observed changes in C(r = 1 mm) with V_0 are due to a shift in the spatial wavelength

λ. The observed variations in C(r = 1 mm) [from a minimum of 0.79±.05 at V_0 = 10.4 volts to a maximum of 0.86±.05 at V_0 = 16.0 volts] account for a change in λ of at most 2 mm. This, in turn, implies that C(r = 4 mm) and C(r = 7 mm) could not fall below 0.95±.05 and 0.82±.08, respectively, *if the wave were spatially coherent for all* V_0. Therefore, the fact that C(r = 4 mm) and C(r = 7 mm) have dropped to 0.71±.05 and 0.45±.05, respectively, at V_0 = 21.7 volts provides quantitative evidence that we are indeed observing a (partial) loss of spatial coherence with increasing voltage V_0.

We would like to determine whether this breakup of spatial order can be characterized by chaotic dynamics: Do the spatially uncorrelated states still correspond to motion in phase space along a low-dimensional strange attractor? We have as yet been unable to answer this question definitively. Just prior to the breakup of spatial coherence, V_0 = 12.1 volts, the total current I(t) of the system is characterized by a low-dimensional attractor; measurements of the fractal dimension yield d = 2.5 [figure 4.7(a)]. However, just after the onset of spatial disordering, V_0 = 12.9 volts, the fractal dimension has increased to the point where we cannot calculate its value -- we can only set a lower limit: $d \geq 8$. This is shown in figure 4.7(b) where the slope has not converged with respect to either embedding dimension D or number of data points N. Figure 4.7(b) was taken with N = 884000 and required 50 hours of CPU time on a Sun microcomputer. For V_0 = 21.8 volts, N = 884000 points and embedding dimension D = 18, the slope is 14 and has

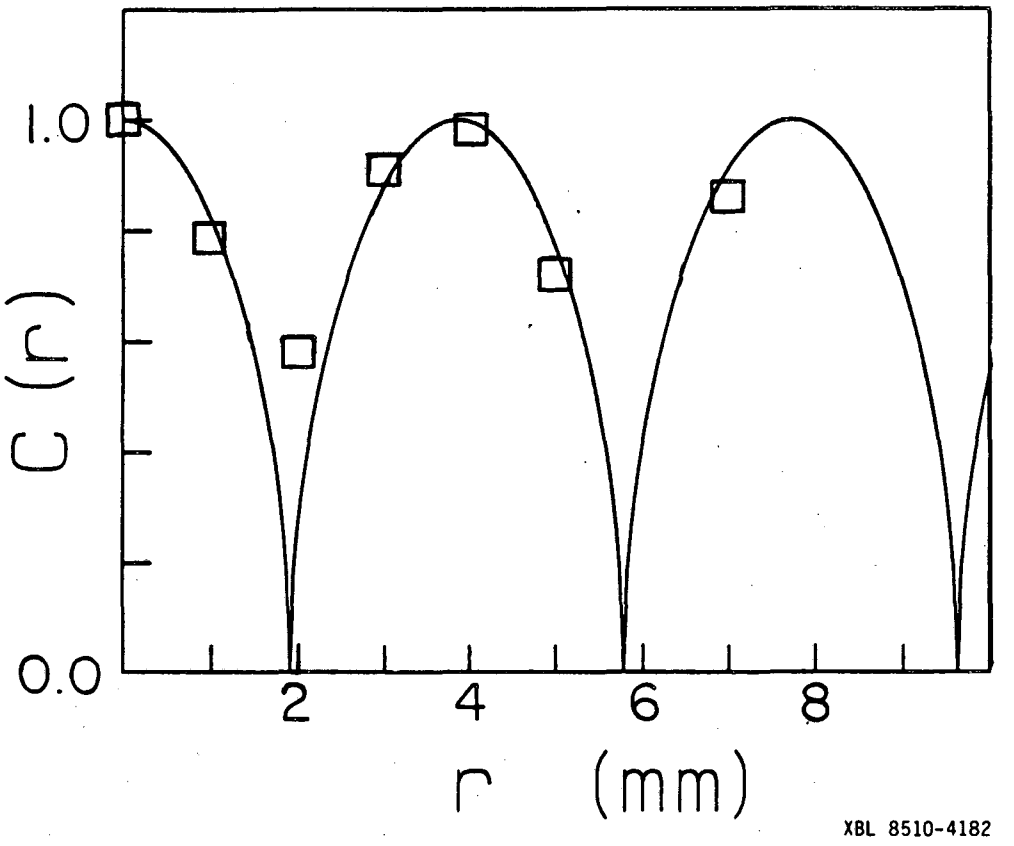

Figure 4.5. Comparison of measured values (□) of spatial correlation function, C(r), equation (4.1), with theoretical correlation function, S(r), equation (4.2), computed for $\lambda = 7.7$ mm (solid line). Data were taken for periodic state at $B_0 = 11.15$ kGauss, $V_0 = 10.4$ volts using voltages from pairs of side probes separated by distance r. C(r) is normalized such that $C(r = 0) = S(r = 0) = 1$.

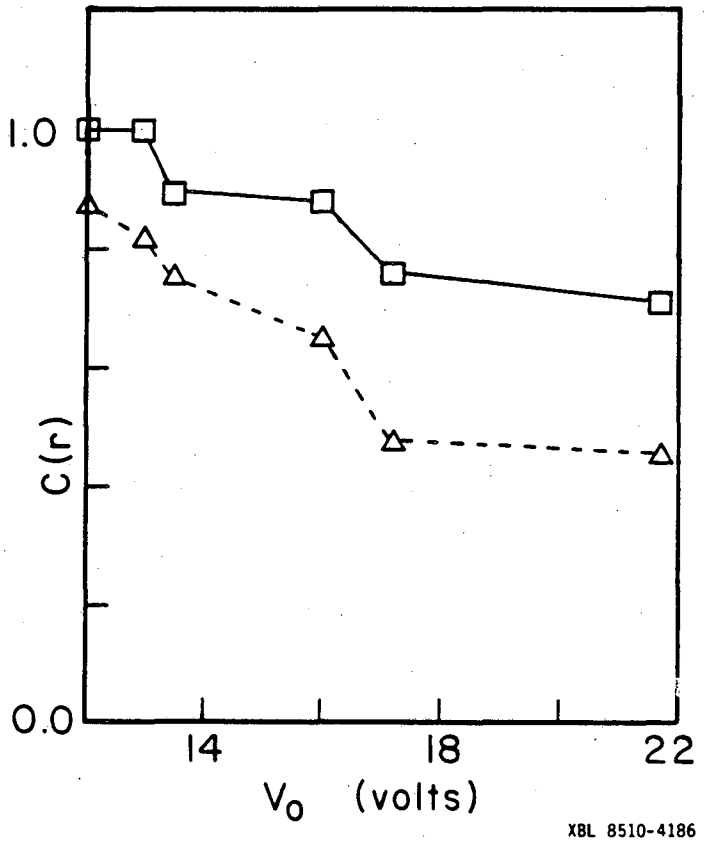

Figure 4.6. Plots of measured correlation functions C(r = 4 mm) [□] and C(r = 7 mm) [Δ] for increasing V_0. B_0 = 11.15 kGauss. At each voltage C(r) is normalized such that C(r = 0) = 1.

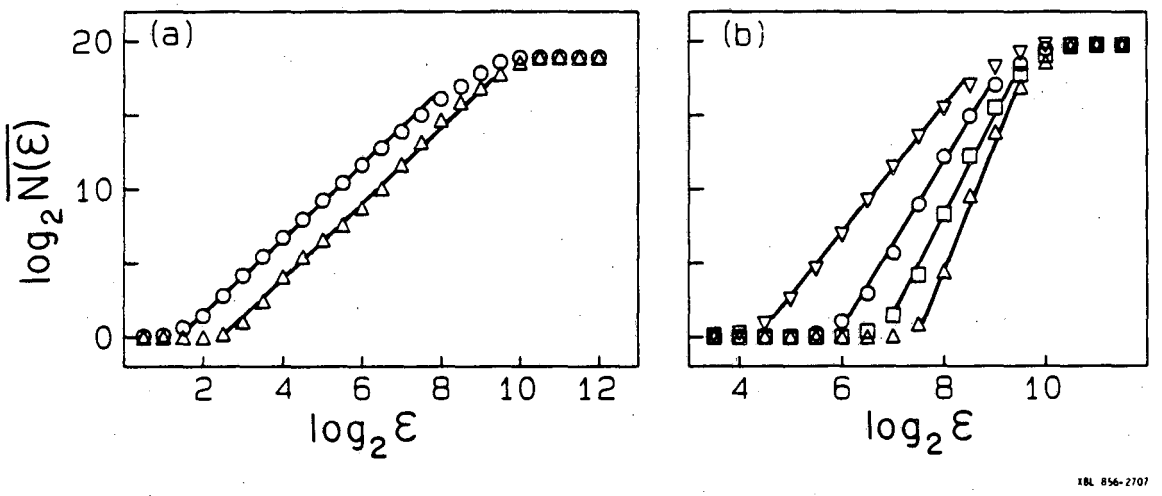

Figure 4.7. Plots of $\log\overline{N(\epsilon)}$ vs. $\log\epsilon$ used to determine fractal dimension d at $B_0 = 11.15$ kGauss. (a) $V_0 = 12.1$ volts, N = 490000 data points; the symbols o and Δ refer to embedding dimensions D of 4 and 8, respectively. Slopes have converged to 2.5 with respect to both D and N. (b) $V_0 = 12.9$ volts, N = 884000; ∇, o, $\square$ and Δ refer to D = 6, 10, 14 and 18, respectively. Slopes have not converged with respect to either D or N. For D = 18 slope is 8.7.

definitely not converged.

For our fractal dimension plots of figure 4.7 we note that the curves become horizontal (saturate) for (i) $\epsilon > \epsilon_1$, a hypershpere large enough to include all points on the attractor and for (ii) $\epsilon < \epsilon_2$, a hypershere so small that only the single point at its center is within it. This behavior is to be expected for all fractal dimension plots, provided ϵ is varied sufficiently; it is important to do this to ensure that all experimental data are examined.

Calculations based on time series taken across different pairs of probe contacts $V_i(t)$ yield the same fractal dimensions d as those based on total current I(t), for both spatially coherent and incoherent states. Further, we find that for fixed values of our applied fields, the power spectrum measured across a pair of probe contacts $| V_i(\omega) |^2$ is essentially identical to the power spectrum of the total current $| I(\omega) |^2$. This suggests that the spatial incoherence may be due to the dispersive nature of the e-h plasma.

This difficulty in calculating large fractal dimensions is a problem incurred with very chaotic systems. The number of data points required for convergence increases exponentially with the fractal dimension of the system.[11,12] At present, although we know that our system experiences a large jump in dimensionality at the onset of spatial incoherence, we have not yet determined whether this onset is characterized by chaotic dynamics of an attractor of fractal dimension may orders of magnitude smaller than the number of degrees of freedom of the particles in the system ($\sim 10^{10}$). Other approaches for quantitatively characterizing very chaotic states (say, $d > 10$)

will need to be developed before this intriguing question can be answered.

References. Chapter IV

1. for example, H. L. Swinney, Physica (Utrecht) **7D**, 3 (1983); see also *The Physics of Chaos and Related Problems,* edited by S. Lundqvist, Phys. Scr. **T9** (1985).

2. D. Ruelle and F. Takens, Comm. Math. Phys. **20**, 167 (1971); E. Ott, Rev. Mod. Phys. **53**, 655 (1981).

3. S. Ciliberto and J. P. Gollub, Phys. Rev. Lett. **52**, 922 (1984).

4. O. H. Olsen, P. S. Lomdahl, A. R. Bishop and J. C. Eilbeck, J. Phys. C **18**, L511 (1985).

5. G. A. Held and C. D. Jeffries to appear in *Proceedings of the International Symposium on Synergetics at Schloss Elmau, Bavaria, 6-11 May, 1985,* edited by H. Haken (Springer-Verlag).

6. G. A. Held and C. Jeffries, Phys. Rev. Lett. **55**, 887 (1985).

7. N. H. Packard, J. P. Crutchfield, J. D. Farmer and R. S. Shaw, Phys. Rev. Lett. **45**, 712 (1980).

8. The standard definition of a correlation function is actually the square of the right hand side of equation (4.1).

9. C. E. Hurwitz and A. L. McWhorter, Phys. Rev. **134**, A1033 (1964).

10. T. Misawa and T. Yamada, Jpn. J. Appl. Phys. **2**, 19 (1963).

11. H. Froehling, J. P. Crutchfield, J. D. Farmer, N. H. Packard, and R. Shaw, Physica **3D**, 605 (1981).

12. H. S. Greenside, A. Wolf, J. Swift and T. Pignaturo, Phys. Rev. **A 25**, 3453 (1982).

CHAPTER V. EXTERNALLY DRIVEN INSTABILITIES

5.1. Introduction

Quasiperiodic transitions to chaos have been reported in Chapters III and IV. In these cases, the only control parameters were the dc electric field E_0, the magnetic field B_0, and the angle between the applied fields θ. Increasing E_0, we were able to clearly observe the transition from periodicity to quasiperiodicity to chaos. However, we have found that varying E_0, B_0, and θ provides little control over the ratio of the two frequencies of the quasiperiodic state f_2/f_1. On the other hand, most detailed theoretical studies of the quasiperiodic route to chaos[1,2,3] assume that this ratio is a readily tunable control parameter. In particular, the only quantitative predictions of a universal quasiperiodic transition to chaos[1,2] assume that f_2/f_1 may be fixed at a given irrational ratio, usually the inverse of the golden mean, $\sigma_g \equiv (\sqrt{5}-1)/2 = 0.618\ldots$

We would like to determine the extent to which these universal predictions are applicable to our experimental system. To this end we have designed the following experiment. The control parameters E_0, B_0, and θ are fixed at values such that the plasma instability is simply periodic at frequency f_1. An ac voltage $V_1 \sin 2\pi f_2 t$ is then applied across a pair of spatial probe contacts (as described in Chapter II). This ac perturbation interacts non-linearly

with the unstable periodic density wave and, by varying f_2 and V_1, we are able to control both the ratio f_2/f_1 and the degree of non-linear mixing.

The second section of this chapter is a review of the existing theoretical predictions concerning the quasiperiodic transition to chaos and the third section describes our experimental results.

5.2. Theoretical Predictions

Quasiperiodic behavior (simultaneous oscillations at two incommensurate frequencies) corresponds to motion in phase space along an invariant two-dimensional torus. A Poincaré section of this torus is topologically equivalent to a circle. As each point on this curve is mapped to another point on the same curve, it is known as an invariant circle. The transition to chaos corresponds to the destruction of the invariant torus, and this is reflected in the breakup of the invariant circle, i.e., it becomes no longer smooth. It is therefore reasonable to consider a non-linear mapping of the circle onto itself as a model for experimentally observed quasiperiodic transitions to chaos.[4]

Mappings of the invariant circle (so-called "circle maps") have been studied extensively. Perhaps the best known is the sine circle map

$$\phi_{n+1} = \phi_n + \omega - \frac{a}{2\pi}\sin 2\pi\phi_n \qquad (5.1)$$

where ϕ_n is the angle on the circle, a specifies the nonlinearity and ω is the frequency ratio (f_2/f_1) in the limit $a = 0$. For $0 < a < 1$ the mapping is either frequency locked ($f_2/f_1 = p/q$; p,q integers) or quasiperiodic

($f_2/f_1 \neq p/q$; p,q integers). For a fixed value of a, the range of ω over which $f_1/f_2 = p/q$ for each p/q is finite (for $a > 0$) and widens as the nonlinear control parameter a is increased. These frequency locked regions form horn-like structures in the (a,ω) plane known as "Arnold tongues."[1,5,6] The ratio f_2/f_1 is known as the winding number ρ. Further, it is found[5,6] that for a fixed value of a and increasing ω, the tongue with winding number (p+p')/(q+q') is always observed between the tongues with winding numbers p/q and p'/q'.

For $a < 1$ the map (5.1) is invertible, whereas for $a > 1$ it is non-invertible. It is only in the unstable region $a > 1$ that chaos may be observed.[5] Thus, for the mapping (5.1) the onset of instability is simply the straight line $a = 1$ in the (a, ω) plane. For more general circle maps, the onset of instability is not necessarily a straight line.[3] Instead, it is often a curve $a_{crit}(\omega)$, where a is again a measure of the non-linear coupling and ω is defined as the ratio f_2/f_1 at $a = 0$. We refer to $a_{crit}(\omega)$ as the critical line. For all such maps, the ordering of the Arnold tongues is identical to that observed for equation (5.1).

For equation (5.1), the widths of the Arnold tongues are found to increase with a. At $a = 1$ these locked regions form a Cantor set,[7] and the fractal dimension d of this Cantor set was found numerically[3] to be 0.868 . . . Numerical results indicate that this result is universal for maps with cubic inflection points.[3,8] That is, the locked regions on the critical line $a_{crit}(\omega)$, for any map of the invariant circle with cubic inflection points, should form a Cantor set of fractal dimension $d = 0.868 \ldots$

Universal quasiperiodic transitions to chaos are predicted to occur in the absence of frequency locking. In particular, detailed renormalization analyses[1] predict that when f_2/f_1 is fixed at $\sigma_g = (\sqrt{5}-1)/2 = 0.618\ldots$ (i.e., the inverse of the golden mean), the transition from quasiperiodicity to chaos will occur in a universal fashion. Figure 5.1 shows part of the power spectrum of equation (5.1) at the onset of chaos ($a = 1$) for $\rho = \sigma_g$. The power spectrum of any circle map at the onset of chaos, for $\rho = \sigma_g$, should have low frequency structure identical to that shown here.

Figure 5.1 is the power spectrum of $\phi_n - n\rho$. The horizontal axis is log f (frequency) and the vertical axis is log $(P(f)/f^2)$, where P(f) is the spectral power density at frequency f. The frequency f_1 has been normalized to unity. The scales of these axes have been chosen so as to accentuate the universal structure of the spectrum. The spectrum is divided into bands (labeled $B_0, B_1, \ldots$) separated by the spectral peaks $f_{jk} \equiv |\, j\sigma_g - k\,|$, where j and k are adjacent elements of the Fibonacci series[9] (1, 1, 2, 3, 5, ...). Peaks labeled 2, 3, and 4 are of the form $f_{jk} \equiv |\, j\sigma_g - k\,|$ where j and k are adjacent elements of the Fibonacci series (2, 2, 4, 6, ...), (1, 3, 4, 7, ...), and (3, 3, 6, 9, ...), respectively. An infinite number of such sequences of peaks are contained in the spectrum. Only the most prominent ones are shown in figure 5.1.

There are two striking features of this power spectrum. First, within each band one may observe a self-similarity in the spacing between peaks. That is, the spacing between peaks within each band B_j is identical to the

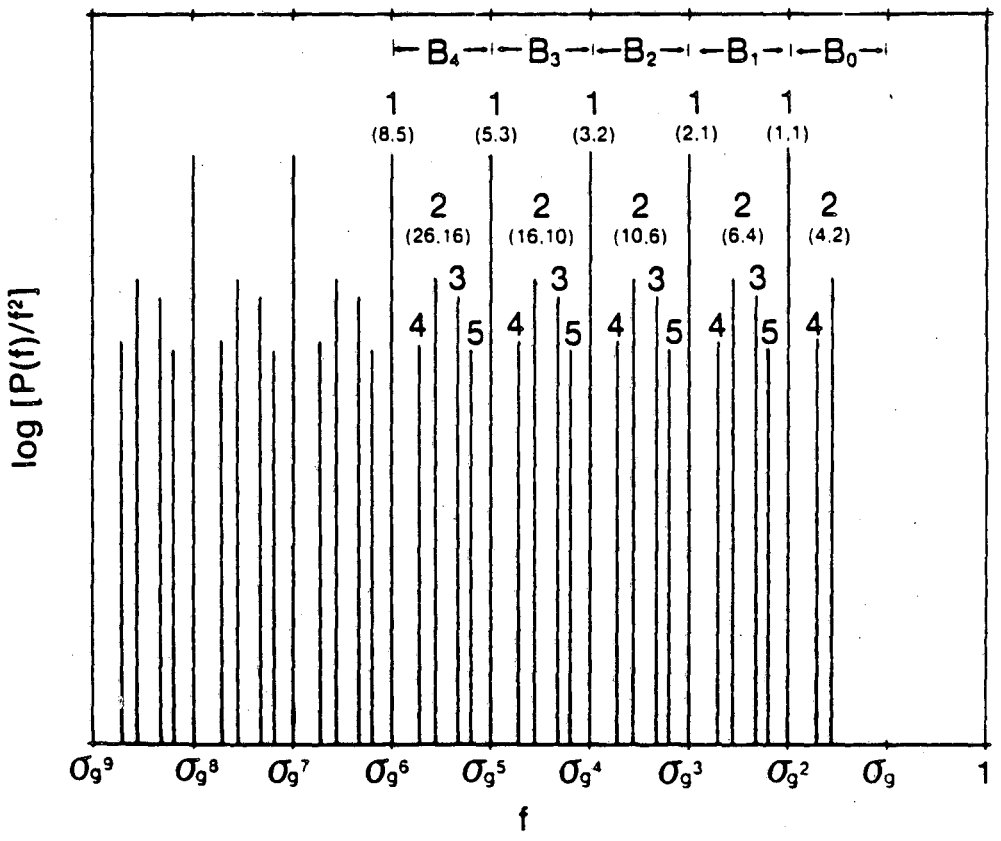

XBL 8510-4244

Figure 5.1. A portion of the power spectrum of the sine circle map [equation (5.1)] for the parameters $\rho = \sigma_g$ and $a = 1$ (the onset of chaos). The spectrum computed is that of $\phi_n - n\rho$; the spectrum of $(\phi_n)_{\text{mod } 1}$ is equivalent.[4] P(f) is the spectral power density. The frequency f_1 has been normalized to unity, and the bands (B_0, B_1, B_2, . . .) are separated by the principal peaks, which are at powers of σ_g. All peaks are of the form $f_{jk} \equiv |\, j\sigma_g - k \,|$ where j and k are adjacent elements of a Fibonacci series. All peaks with pairs (j,k) from a common Fibonacci series are labeled by the same integer (see text). The pair (j,k) for each peak f_{jk} of the first and second Fibonacci series is also shown. The power spectrum consists of an infinite number of such series of peaks, only the most prominent ones are shown here. This figure is from reference 4, adapted from reference 1.

spacing between peaks within every other band -- the lines in each band B_j are in a one-to-one correspondence. This is simply a consequence of the fact that the winding number is equal to σ_g and may therefore be expressed as the continued fraction <1, 1, 1, . . .>. This is not a consequence of the system being at the onset of chaos.

The second striking feature is that all peaks f_{jk} with pairs (j, k) taken from a common Fibonacci series are of the same height [for vertical scale $P(f)/f^2$] in the limit $f \rightarrow 0$. That is, all peaks labeled 1, 2, or 3 are the same height as all other peaks labeled 1, 2, or 3, in the limit of low frequency. This *is* a consequence of the system being at the onset of chaos. Just prior to the onset of chaos this scaling would not be present below some cross-over frequency.[1] Above the threshold of chaos, the spectral peaks should broaden. Further, it has been suggested[2] that the fractal dimension d of the chaotic time series $\{\phi_n\}$ should scale as

$$(d-2) = \kappa(a-a_c)^{\beta} \tag{5.2}$$

where a_c is the critical value of a (at $\rho = \sigma_g$) and $\beta = 0.948\ldots$ is a universal exponent.

5.3. Experimental Results

The operating parameters for this experiment include a dc voltage $V_0 = 7.00$ volts and a dc magnetic field $B_0 = 9.32$ kGauss. For these fields the plasma instability is simply periodic at a fundamental frequency $f_1 = 178$

kHz, with some higher harmonics present as well. As V_0 is increased, the instability becomes quasiperiodic at 7.49 volts and chaotic at 7.79 volts. At $V_0 = 8.04$ volts the instability undergoes an abrupt change; it becomes simply periodic at $f_1 = 295$ kHz. This new mode exhibits hysteresis, i.e., as V_0 is decreased from 8.04 to 7.00 volts, the instability remains periodic and f_1 decreases continuously from 295 to 271.5 kHz. This is in contrast to the 178 kHz mode observed at $V_0 = 7.00$ volts whenever V_0 is increased from 0 to 7.00 volts. In the experiments described below, we always set the operating conditions such that at $V_0 = 7.00$ volts and $B_0 = 9.32$ kGauss the 178 kHz mode is present with $V_1 = 0$ volts. However, as will be shown below, the application of an ac perturbation can cause the system (in some instances) to shift into the 271.5 kHz mode.

We perturb the simply periodic state ($V_0 = 7.00$ volts, $B_0 = 9.32$ kGauss, $f_1 = 178$ kHz) by applying an ac voltage $V_1 \sin 2\pi f_2 t$ across the pair of probe contacts nearest the p^+ end contact. We monitor the response of the system by observing the power spectrum of the total current. For V_1 below $\sim$55 mvolts, chaos is not observed for any values of f_2. However, frequency lockings are observed and the widths of the locked horns are observed to increase with increasing V_1. This behavior is shown in figure 5.2 -- a plot of the frequency-locked horns as a function of V_1 and f_2. Only the widest horns are shown; stable lockings with denominators as large as 21 have been observed.

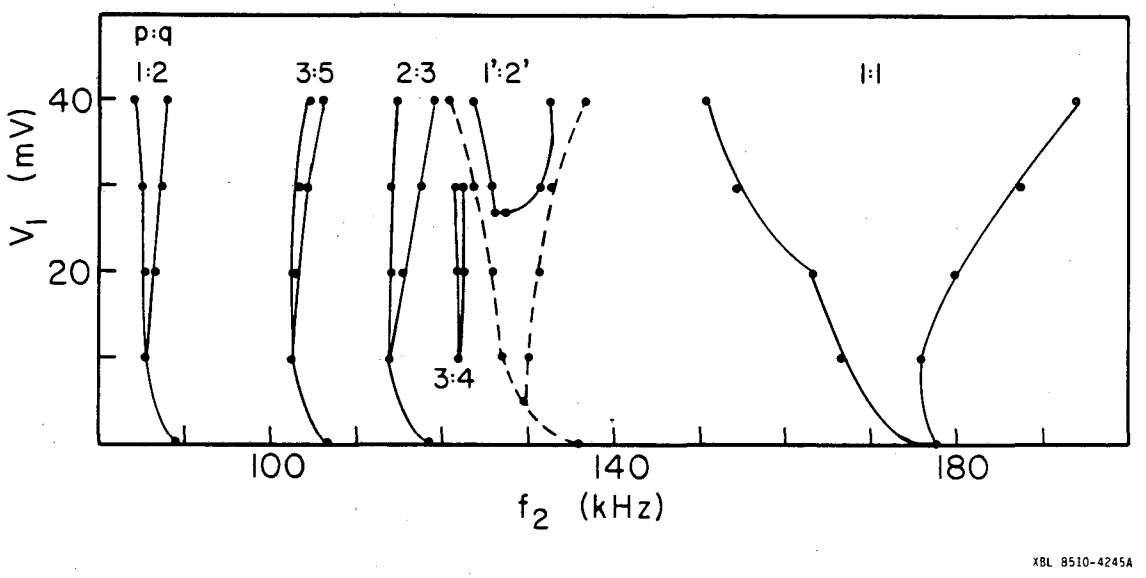

Figure 5.2. Experimental plot of frequency locked regions as a function of f_2 and V_1. Operating conditions are $V_0 = 7.00$ volts, $B_0 = 9.32$ kGauss, and a perturbation $V_1 \sin 2\pi f_2 t$ applied across the pair of spatial probe contacts closest to the p^+ end contact. Only the widest frequency lockings are shown here; stable locked states with denominators as large as 21 have been observed. The notation p:q (p,q integers) identifies the locked state $f_2/f_1 = p/q$. All of the lockings shown in this figure (except the 1':2' locking) are between the external frequency f_2 and the 178 kHz instability (i.e., $f_1 = 178$ kHz at $V_1 = 0$ volts). The notation 1':2' refers to a 1:2 locking between the external frequency f_2 and the 271.5 kHz instability (i.e., $f_1 = 271.5$ kHz at $V_1 = 0$ volts). This locking is hysteretic and thus the locked region must be defined by two boundaries, the solid and dotted lines, as discussed in the text.

The sequence of observed lockings is the same as that predicted theoretically[5,6], with the exception of the 1':2' locking. All of the other tongues result from a locking between the applied excitation f_2 and the 178 kHz instability. However, for $V_1 > 38$ mvolts, the 271.5 kHz oscillations appear, in a 1:2 locking with the perturbing mode f_2. We label this 1':2'. The left side of the solid line defining the 1':2' horn was measured by sweeping from low to high f_2 for fixed values of V_1; the right side was measured by sweeping from high to low f_2 for fixed V_1. In either case, as the external frequency f_2 crossed this solid line, the fundamental frequency f_1 of the instability would abruptly shift from 178 kHz to $2f_2$ ($\approx$271 kHz). The dotted line enveloping the 1':2' horn defines the boundaries of the 1':2' locking as measured from within the locked state. That is, if the system is already locked in the 1':2' state, it will remain locked for all values of V_1 and f_2 contained within the region denoted by the dotted line; the area between the solid and dotted lines is the region of parameter space where the system is hysteretic. As one moves out of the 1':2' horn (as defined by the dotted line), the jump in the fundamental frequency f_1 -- from $2f_2$ ($\approx$271 kHz) to 178 kHz -- is abrupt.

To determine whether these instabilities follow the predicted universal quasiperiodic transition to chaos, we fix the ratio f_2/f_1 at σ_g. As V_1 is increased, it becomes necessary to adjust f_2 so as to maintain the σ_g ratio. We find that experimentally we can maintain the ratio $f_2/f_1 = \sigma_g$ to approximately two parts in 10^4. Power spectra of the total current, recorded at $V_1 = 13.9$, 103.1, 128.4, and 154.9 mvolts are shown in figures 5.3 (a)-(d),

respectively. At $V_1 = 13.9$ mvolts the system is quasiperiodic, and sums and differences of the form $mf_1 + nf_2$ (m, n integers) are observed. At $V_1 = 103.1$ mvolts, at the threshold of chaos, the strength and number of such combination frequencies has increased dramatically and the fundamental peak f_1 has broadened slightly. At $V_1 = 128.4$ mvolts, just above the chaotic threshold, the number of peaks has diminished, and those remaining have been slightly broadened. As V_1 is increased to 154.9 mvolts, a 1:2 locking between the external frequency f_2 and the 271.5 kHz mode (which is pulled to 235 kHz by the external perturbation) is observed [figure 5.3 (d)]. This locking curtails the theoretically expected[2] transition to higher dimensional chaos. In addition to the sharp peaks of the locked modes, a broad peak centered at 190 kHz, presumably due to the initial instability ($f_1 = 178$ kHz at $V_1 = 0$ volts), is also observed. However, this peak is 45 dB weaker than the sharp, frequency locked peaks; we are unable to determine whether it is broadened by stochastic or deterministic processes.

Figure 5.4 shows the power spectrum of the total current at the onset of chaos ($V_1 = 103.1$ mvolts), with log f plotted on the horizontal axis and log $(P(f)/f^2)$ plotted on the vertical axis. The self-similar band structure resulting from the fact that $f_2/f_1 = \sigma_g$ is readily observable. Peaks in this figure are labeled 1, 2, 3, and 4 following the labeling scheme of figure 5.1. At

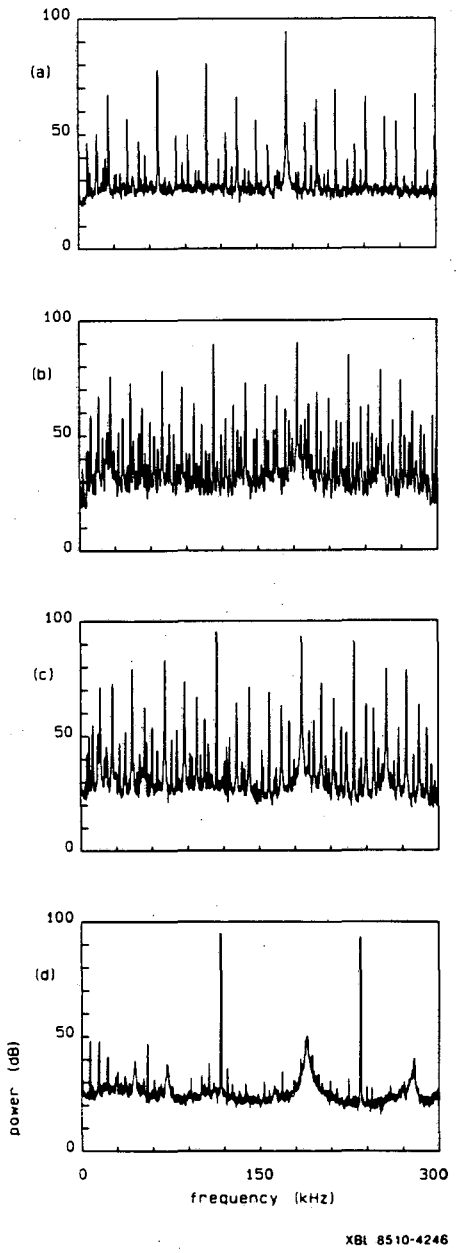

Figure 5.3. Power spectra of the total current I(t) for operating conditions $V_0 = 7.00$ volts, $B_0 = 9.32$ kGauss, and a perturbation $V_1 \sin 2\pi f_2 t$ applied across the pair of spatial probe contacts closest to the p^+ end contact. The frequency f_2 is adjusted so that $f_2/f_1 = \sigma_g$ to approximately 2 parts in 10^4 for all power spectra shown. V_1 is increasing, (a) to (d). For $V_1 = 0$ volts, the frequency $f_1 = 178$ kHz. (a) $V_1 = 13.9$ mvolts, quasiperiodic. (b) $V_1 = 103.1$ mvolts, onset of chaos. (c) $V_1 = 128.4$ mvolts, just beyond the onset of chaos. (d) $V_1 = 154.9$ mvolts, f_2 is frequency locked to a 271.5 kHz unstable mode (see text). The ratio $f_2/f_1 = \sigma_g$ is maintained between the external frequency f_2 and the initial instability f_1, which for this value of V_1 consists of a broadband peak centered at 190 kHz and 45 dB weaker than the frequency locked peaks at 117.5 and 235 kHz.

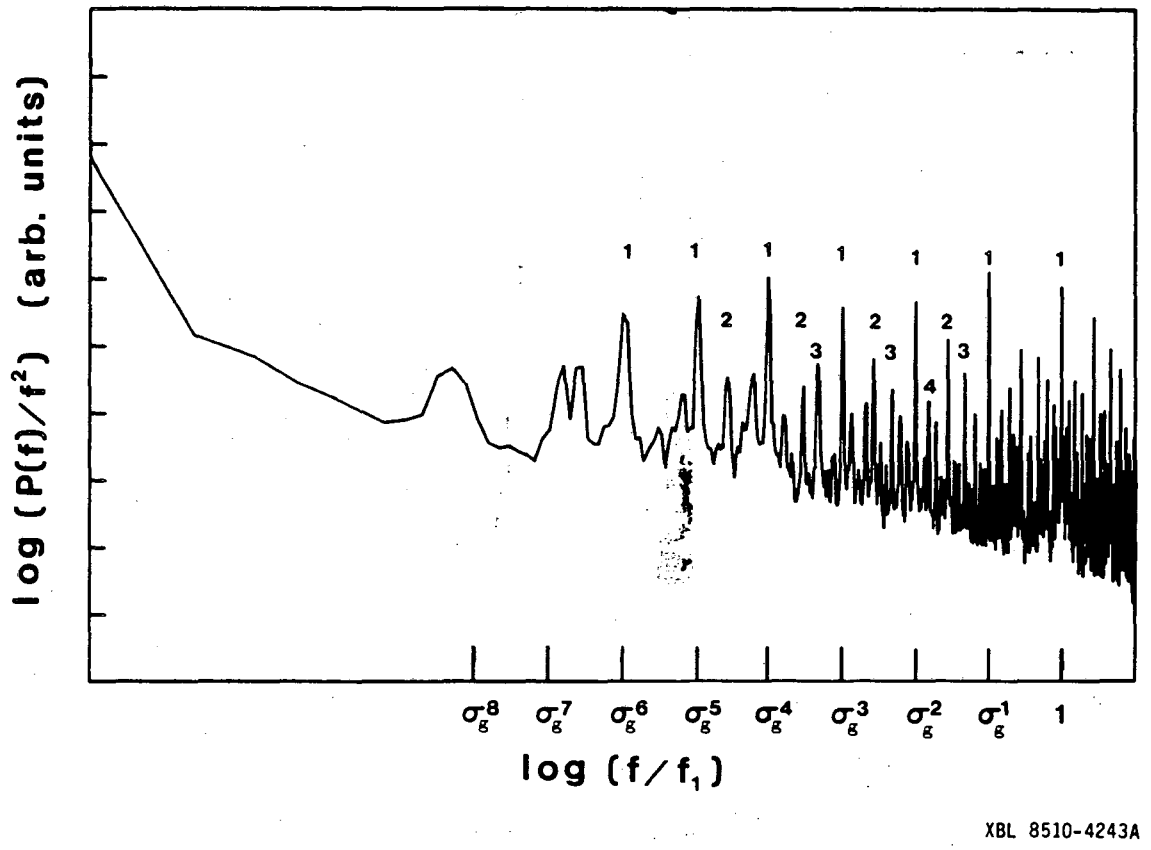

Figure 5.4. Power spectrum of the total current at the onset of chaos. Same spectrum as in figure 5.3(c), with log f (frequency) plotted on the horizontal axis and $\log[P(f)/f^2]$ plotted on the vertical axis, where P(f) is the spectral power density. The peaks are labeled using the same notation as in figure 5.1.

low frequencies, all peaks labeled with the same number are predicted to be of the same height. This is observed only approximately. Several possibilities could account for the deviations from theory. First, we may not be exactly at the onset of chaos. Second, in general, the theory holds only in the limit of low frequencies; we may not be at sufficiently low frequencies to observe the predicted scaling. Finally, the hysteretic nature of our system is clearly responsible for deviations from theory within the chaotic regime [as in figure 5.3(d)]; it is reasonable to suspect that it may also affect the relative peak heights at the onset of chaos. We note that experimental studies of quasi-periodic transitions to chaos in Rayleigh-Bénard convection systems[4,10] have also been unable to clearly observe the predicted scaling of spectral peak heights.

We calculate the fractal dimension d of the Cantor set of locked regions along the critical line $a_{crit}(\omega)$ as follows.[8,11] Let S be the length of the interval between two locked states P_n:P_{n+1} and P_{n+1}:P_{n+2}, where P_n, P_{n+1}, and P_{n+2} are successive elements of the first Fibonacci series. Further, let S_1 and S_2 denote the distance between the locked state (P_n+P_{n+1}):$(P_{n+1}+P_{n+2})$ [located between P_n:P_{n+1} and P_{n+1}:P_{n+2}] and the states P_n:P_{n+1} and P_{n+1}:P_{n+2}, respectively. Then, in the limit of large P_n, one expects that[12]

$$\left(\frac{S_1}{S}\right)^d + \left(\frac{S_2}{S}\right)^d \approx 1. \tag{5.3}$$

The definitions of S_1, S_2, and S (as well as Ω_n, Ω_{n+1}, and Ω_{n+2} – which will be defined shortly) are illustrated in figure 5.5.

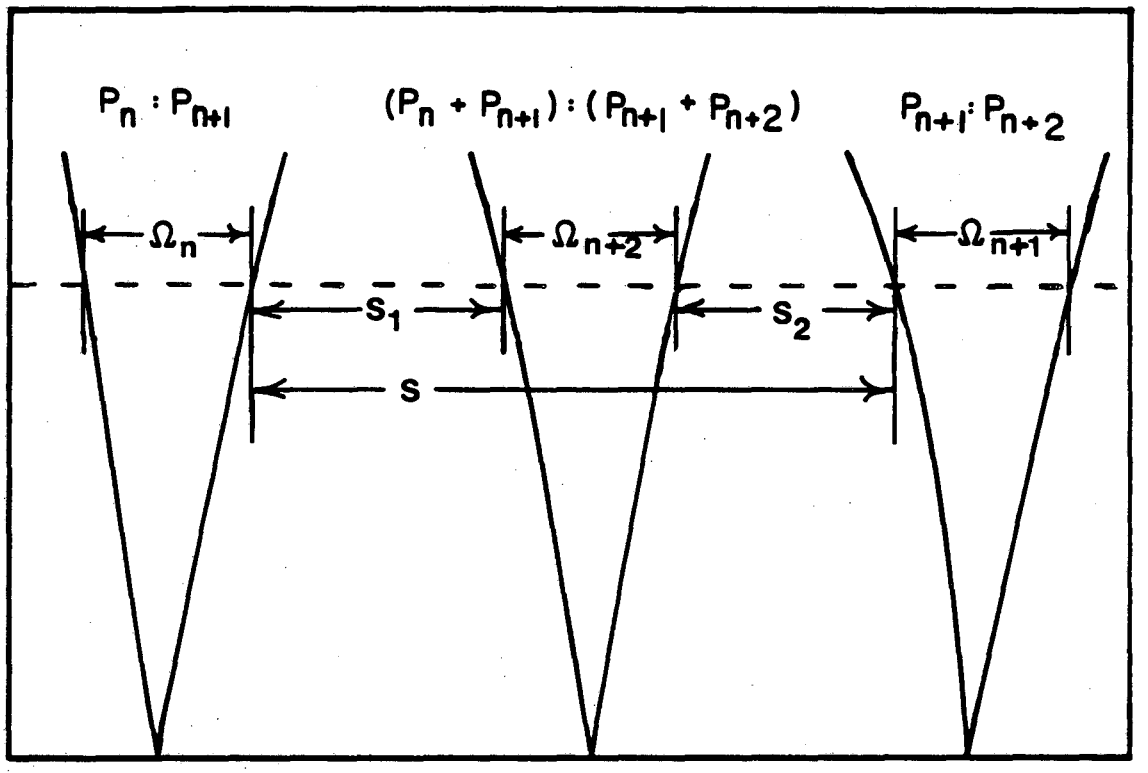

XBL 8510-4494

Figure 5.5. Illustration of the definitions of S_1, S_2, S, Ω_n, Ω_{n+1}, and Ω_{n+2}, as used in equations (5.3) and (5.4). P_n, P_{n+1}, and P_{n+2} are three successive Fibonacci numbers and the frequency locked regions P_n:P_{n+1}, (P_n+P_{n+1}):$(P_{n+1}+P_{n+2})$, and P_{n+1}:P_{n+2} are labeled as such. For our experiments, the vertical axis would be V_1 and the horizontal axis would be f_2, as defined in figure caption 5.2.

Applying relation (5.3) to the locked states 3:5, 5:8, and 8:13 we observe $d \approx 0.86 \pm .04$; as compared to the predicted[3] value of 0.868... The locked states 3:5, 5:8, and 8:13 were observed in the intervals 107.13 – 109.98, 112.62 – 113.48, and 111.50 – 111.76 MHz, respectively. It is also predicted[1] that δ, defined as

$$\delta \equiv \lim_{n\to\infty} \frac{\Omega_n - \Omega_{n+1}}{\Omega_{n+1} - \Omega_{n+2}} \tag{5.4}$$

where Ω_n, Ω_{n+1}, and Ω_{n+2} are the widths of the locked states P_n:P_{n+1}, P_{n+1}:P_{n+2}, and (P_n+P_{n+1}):$(P_{n+1}+P_{n+2})$, respectively, is a universal constant. For $f_2/f_1 = \sigma_g$, δ is predicted[1] to be 2.833... Using the 3:5, 5:8, and 8:13 lockings we measure $\delta \approx 3.3 \pm 1.2$, again, only approximately in agreement with theory.

Serious questions remain as to exactly what effect the observed hysteresis has on the observed transition to chaos. If the operating parameters E_0, B_0, and θ are chosen such that (in the absence of an ac excitation) the system is in a simply periodic, non-hysteretic[13] state, then the subsequent application of an ac perturbation might result in a quasiperiodic transition to chaos which more closely follows the theoretical predictions. However, at least one such non-hysteretic state could not be driven to chaos by a sinusoidal perturbation; as the perturbation became large, it simply overwhelmed the natural frequency of the plasma instability (i.e., the spectral density of the external perturbation became much larger than that of the natural instability). This suggests that perhaps the application of periodic pulses (which allow the plasma

instability more degrees of freedom) would result in a transition to chaos which could be closely modeled by theory.[14] Experiments along these lines are currently in progress.

References. Chapter V

1. M. J. Feigenbaum, L. P. Kadanoff, and S. J. Shenker, Physica (Amsterdam) **5D**, 370 (1982); D. Rand, S. Ostlund, J. Sethna, and E. Siggia, Physica (Amsterdam) **8D**, 303 (1983).

2. M. H. Jensen and I. Procaccia, submitted to Phys. Rev. **A.**

3. M. H. Jensen, P. Bak, and T. Bohr, Phys. Rev. Lett. **50**, 1637 (1983); Phys. Rev. **A 30**, 1960 (1984); T. Bohr, P. Bak, M. H. Jensen, Phys. Rev. **A 30**, 1970 (1984).

4. A. P. Fein, M. S. Heutmaker, and J. P. Gollub, Physica Scripta **T9**, 79 (1985).

5. L. Glass and R. Perez, Phys. Rev. Lett. **48**, 1772 (1982).

6. V. I. Arnold, Trans. Am. Math. Soc., 2nd Ser. **46**, 213 (1965); M. R. Herman, *Geometry and Topology,* Lecture Notes in Mathematics No. 597 (Springer-Verlag, Berlin, 1977) p. 271.

7. for example, J. D. Farmer, *Evolution of Order and Chaos,* H. Haken, ed. (Springer-Verlag, Berlin, 1982) p. 228.

8. P. Cvitanovic, M. H. Jensen, L. P. Kadanoff, and I. Procaccia, submitted to Phys. Rev. Lett.

9. G. H. Hardy and E. M. Wright, *An Introduction to the Theory of Numbers, Fourth Edition* (Clarendon Press, Oxford, 1962), p. 148.

10. J. Stavans, F. Heslot, and A. Libchaber, Phys. Rev. Lett. **55**, 596 (1985).

11. H. G. E. Hentschel and I. Procaccia, Physica (Amsterdam) **8D**, 435 (1983).

12. The approximation in (5.3) may be improved by including additional terms on the left hand side of the equation, as discussed in reference [8]. However, numerical results indicate that values of d estimated from equation (5.3) are typically accurate to within 1%, see reference [8].
The definitions of S, S_1, and S_2 are based on the assumption that $a_{crit}(\omega)$ is a constant. Experimentally, the form of the function $a_{crit}(\omega)$ is typically not known. It is therefore desirable to measure the gaps S, S_1, and

S_2 between closely spaced lockings (i.e., those lockings with large denominators P_{n+1}, P_{n+2}, and $P_{n+1}+P_{n+2}$). This minimizes the width of the interval of ω considered, thus minimizing the variations in $a_{crit}(\omega)$ over this interval.

13. By non-hysteretic we mean that only a single mode is ever observed for the given values of E_0, B_0, and θ, regardless of the path taken through parameter space to reach these operating conditions.

14. This was also found to be the case for the Rayleigh-Bénard convection experiments of reference 10. J. Stavans, private communication.

CHAPTER VI. CONCLUSIONS AND DISCUSSION

6.1. Conclusions

We find that unstable helical density waves in an electron-hole plasma, when excited by parallel dc electric and magnetic fields, will undergo transitions to low-dimensional chaotic turbulence. The observed behavior includes both period doubling and quasiperiodic transitions to chaos. While the possibility that plasmas could exhibit chaos has been discussed theoretically,[1] this work provides the first evidence of a period doubling and a quasiperiodic transition to chaos in any plasma. Further, this is the first successful attempt at understanding the noise-like behavior which often results when a semiconductor plasma instability is strongly excited -- we have shown that seemingly random behavior of helical instabilities in a semiconductor plasma is in fact low-dimensional and deterministic.

Following a quasiperiodic route, we find that the resulting chaotic state of the system is characterized by a strange attractor which has a fractal dimension of between two and three. By measuring the local variations in plasma density, we find that these "weakly" turbulent states correspond to temporally chaotic, yet essentially spatially coherent plasma density waves.

However, when more strongly excited, these plasma density waves undergo a partial loss of spatial coherence. The onset of the loss of spatial

coherence is characterized by a sudden jump in the dimension of the attractor -- from less than three for spatially coherent states to at least eight after the onset of spatial disorder.

When we excite a periodic instability of frequency f_1 with an external ac perturbation $V_1 \sin 2\pi f_2 t$, we find that the external mode couples to the instability, resulting in a quasiperiodic state with a tunable ratio f_2/f_1. As the amplitude of the external excitation V_1 is increased, the instability can undergo a quasiperiodic transition to chaos. Frequency lockings are observed, and these form Arnold tongues in the (V_1, f_2) plane -- as expected theoretically. When we fix $f_2/f_1 = \sigma_g$ (i.e., the inverse of the golden mean) and increase V_1, we observe a transition to chaos somewhat similar to that expected theoretically. However, the unperturbed (periodic) instabilities which we have studied are hysteretic, and this appears to limit the applicability of existing theoretical models[2] to our experimental results.

6.2. Further Experiments

In this section we discuss some experiments which would further elucidate the structure of the chaotic plasma instabilities discussed in this thesis. These fall into two categories -- experiments concerning the spatio-temporal structure of the instabilities and further studies of externally excited instabilities.

To determine whether or not a plasma density wave is spatially coherent,

we have relied on a comparison between experimentally measured and theoretically calculated spatial correlation functions. This approach has two limitations associated with it. First, the correlation function only indicates whether or not the data fit the theoretical model for a spatially coherent wave; there is no obvious method of determining the *degree* of spatial incoherence (see Chapter IV). Second, there is no simple method of including harmonic distortion in the theoretical correlation function. Thus it is difficult to determine the exact onset of spatial incoherence. We cannot conclusively state that the onset of spatial incoherence is *coincident* with the observed jump in fractal dimension.

Spatial Fourier transforms of the plasma density $\rho(\mathbf{x}, t)$ would provide a more precise measure of the degree of spatial incoherence; the broader the peaks in the transform, the greater the degree of spatial incoherence. The number of points in the Fourier transform would be equal to one-half the number of pairs of probe contacts, and the resolution of the transform would be inversely proportional to the distance between the two farthest probe contacts.[3] If one could form contacts along the length of, say, a 300 x 1 x 1 mm^3 sample, then the resulting spatial transforms would have a resolution of 0.033 cm^{-1}, providing a reasonable measure of spatial coherence. A long sample has the further advantage that the effects of reflected waves (which are damped[4]) would be reduced. Ideally, one would like to take long time series of the signals at all of the spatial probes *simultaneously*. One would then be able to calculate the spatial Fourier transform and the fractal dimension of the

attractor from the same data set. In this fashion one could rigorously determine the relationship between fractal dimension and spatial coherence.

This approach has at least two difficulties. First, it would be difficult to prepare such a long sample. (Building a magnetic which produces homogeneous 10 kGauss fields over 30 cm might not be trivial either.) Second, current algorithms for determining quantitative measures of chaos are useful, in practice, only for attractors of fractal dimension d less than, say, 8. Thus, our experiments of Chapter IV suggest that the relationship between spatial and temporal order could still only be quantified just above the onset of spatial incoherence. However, even this would be significant.

Further experiments on helical instabilities coupled to an external perturbation would also be of interest; the experiments along these lines discussed in Chapter V were complicated by the hysteretic nature of the instabilities. If a simply periodic, non-hysteretic instability (i.e., one for which only a single mode is ever observable for some E_0 and B_0) were coupled to a periodic perturbation, then it is possible that a resulting quasiperiodic transition to chaos could be closely modeled by existing theories of the invariant circle (see Chapter V). Power spectra taken at the onset of chaos, as well as measurements of the universal exponents δ and β, and the fractal dimension d (see Chapter V) would indicate the extent to which these theories are experimentally applicable. We note that experiments on Rayleigh-Bénard convection[5] (as well as our preliminary results, see Chapter V) suggest that periodic pulses (as opposed to a sinusoidal perturbation) should be used to excite the

instabilities in these experiments.

Finally, it should be possible to excite a periodic instability at two external incommensurate frequencies. The question as to whether a quasiperiodic state with three or more incommensurate frequencies can undergo a transition to chaos is still a topic of theoretical debate.[6] These experiments would provide interesting experimental observations concerning the stability of three frequency quasiperiodic states and (if these states exist) the routes they follow to chaos.

6.3. Additional Semiconductor Plasma Instabilities

Our decision to study the nonlinear dynamics of helical instabilities in an electron-hole plasma was motivated by earlier work on these instabilities. Spontaneous oscillations were observed experimentally[7] and a linear analysis of the system (see Appendix A) indicated that these oscillations were the result of an unstable helical density wave.[4,8] However, in addition to simple oscillations, the observation of incoherent oscillations and noise-like behavior was also reported.[7] This suggested that quasiperiodicity and chaos had been observed, but were not recognized as such due to the lack of a theoretical framework.

Similarly, indications of possible transitions to chaos are found in early reports of other semiconductor plasma instabilities.[9] These include magnetic pinch instabilities,[10] the Gurvich-Ioffe instability,[4,11,12] and acousto-electric instabilities.[13,14] In each of these cases a transition from simply periodic

behavior to some sort of incoherent oscillations was reported. In the case of a driven acousto-electric instability, the observation of a subharmonic at one one-half the driving frequency was reported,[14] suggesting a possible period doubling transition to chaos. We would not be surprised if, upon reexamination, these instabilities could also be understood in the context of chaotic dynamics.

References. Chapter VI

1. for example, J.-M. Wersinger, J. M. Finn, and E. Ott, Phys. Fluids **23**, 1142 (1980).

2. M. J. Feigenbaum, L. P. Kadanoff, and S. J. Shenker, Physica (Amsterdam) **5D**, 370 (1982); D. Rand, S. Ostlund, J. Sethna, and E. Siggia, Physica (Amsterdam) **8D**, 303 (1983); M. H. Jensen, P. Bak, and T. Bohr, Phys. Rev. Lett. **50**, 1637 (1983); Phys. Rev. 1960 (1984); T. Bohr, P. Bak, and M. H. Jensen, Phys. Rev. **A 30**, 1970 (1984); M. H. Jensen and I. Procaccia, submitted to Phys. Rev. **A.**

3. E. O. Brigham, *The Fast Fourier Transform* (Prentice-Hall, New Jersey, 1974).

4. C. E. Hurwitz and A. L. McWhorter, Phys. Rev. **134**, A1033 (1964).

5. J. Stavans, F. Heslot, and A. Libchaber, Phys. Rev. Lett. **55**, 596 (1985); J. Stavans, private communication.

6. for example,C. Grebogi, E. Ott, and J. A. Yorke, Phys. Rev. Lett. **51**, 339 (1983).

7. R. D. Larrabee and M. C. Steele, J. Appl. Phys. **31**, 1519 (1960).

8. M. Glicksman, Phys. Rev. **124**, 1655 (1961); M. Shulz, Phys. Status Solidi **25**, 521 (1968).

9. for a review of semiconductor plasma instabilities see, H. Hartnagel, *Semiconductor Plasma Instabilities* (American Elsevier, New York, 1969); see also, R. Bowers and M. C. Steele, Proc. of the IEEE **52**, 1105 (1964).

10. for example, B. Ancker-Johnson, *Proceedings of the VIIth Int. Conf. Phys. Semicond., Supplement No. 2: Plasma Effects in Solids* (Dunod, Paris, 1965), p. 165.

11. L. E. Gurevich and I. V. Ioffe, Fiz. Tverdogo Tela, **4**, 2641 (1962) [Soviet Physics – Solid State, **4**, 1938 (1963); Fiz. Tverdogo Tela, **4**, 2964 (1962) [Soviet Physics -- Solid State, **4**, 2173 (1963).

12. S. Nakashima and Y. Noguchi, Japan J. Appl. Phys. **2**, 307 (1963); S. Nakashima and Y. Miyai, J. Phys. Soc. Japan **18**, 1219 (1963).

13. for example, IBM J. of Research and Development, **13**, pp. 485-644 (1969); also, S. A. Zemon, J. Zucker, and J. H. Wasko, Proc. IEEE **56**, 778 (1968).

14. M. Schulz and B. K. Ridley, Phys. Lett. **29A**, 17 (1969).

APPENDIX A. EQUATIONS OF MOTION FOR ELECTRON-HOLE PLASMA

For the times and distances of interest, the following partial differential equations describe the motion of conduction electrons and holes in the crystal:[1,2]

$$\mathbf{J}_{e,h} = n_{e,h} q \mu_{e,h} \mathbf{E} \pm q D_{e,h} \nabla n_{e,h} \mp \mu_{e,h} \mathbf{J}_{e,h} \times \mathbf{B} \tag{A.1a}$$

$$\frac{\partial n_{e,h}}{\partial t} = \pm \frac{1}{q} (\nabla \cdot \mathbf{J}) + \gamma \tag{A.1b}$$

$$\nabla \cdot \mathbf{E} = -q(n_e - n_h)/\epsilon \tag{A.1c}$$

where the subscript e(h) and the upper (lower) signs refer to electrons (holes); n is the carrier density, **J** is the current density, q is the magnitude of the electronic charge, μ is the mobility, D is the diffusion constant, ϵ is the dielectric constant of the sample, γ is the net carrier generation rate (including bulk recombination), and **E** and **B** are the electric and magnetic fields, respectively. At surfaces perpendicular to the applied electric field, these equations are subject to the boundary condition $J_e = J_h = qsn_e$, where s is the surface recombination rate.

By expanding the carrier densities and the electric field about their equilibrium values

$$n_e = n_{e0} + n_{e1}(t) \tag{A.2a}$$

$$n_h = n_{h0} + n_{h1}(t) \tag{A.2b}$$

$$\mathbf{E} = \mathbf{E}_0 - \nabla\psi_1(t) \tag{A.2c}$$

and substituting these expressions into equations (A.1), it has been shown[2] that the first order terms lead to a helical density wave,

$$n_{e1} \approx n_{h1} = N_1(r)\, e^{i\omega t - ikz - im\phi} \tag{A.3a}$$

and

$$\psi_1 = \Psi_1(r)\, e^{i\omega t - ikz - im\phi} \tag{A.3b}$$

where m is an integer. Beyond certain thresholds of the applied electric and magnetic fields, the $m = 1$ helical density wave becomes absolutely unstable [$\mathrm{Im}(\omega) < 0$] and spontaneous oscillations occur, coincident with the onset of nonlinear behavior. An illustration of this unstable helical density wave is shown in figure 1.3 (in Chapter I), adapted from Hoh and Lehnert.[3]

To incorporate nonlinear behavior into a model which explains the observed chaotic dynamics, we consider a *superposition* of waves in which the time dependence is not assumed to be periodic,

$$n_{h1} \approx n_{e1} = \sum_{k,m} C_{km}(t)\, N_{km}(r)\, e^{-ikz - im\phi} + \text{c.c.} \tag{A.4a}$$

$$\psi_1 = \sum_{k,m} C_{km}(t)\, \Psi_{km}(r)\, e^{-ikz - im\phi} + \text{c.c} \tag{A.4b}$$

Substituting (A.4) into equations (A.1), and keeping only terms up to second order, results in a set of coupled ordinary differential equations of the form

$$\frac{\partial C_{km}}{\partial t} = M_{km}C_{km} + \sum_{\substack{k_1,k_2 : k_1+k_2=k \\ m_1,m_2 : m_1+m_2=m}} M'_{\ k_1k_2\,;\,m_1m_2} C_{k_1m_1}C_{k_2m_2} \qquad (A.5)$$

$$+ \sum_{\substack{k_1,k_2 : k_1-k_2=k \\ m_1,m_2 : m_1-m_2=m}} M'_{\ k_1k_2\,;\,m_1m_2} C_{k_1m_1}C^*_{k_2m_2}$$

where M and M' are independent of time. This equation describes a wave-wave interaction[4] in which a wave with wave vector k can couple nonlinearly to many different pairs of waves (k_1,m_1), (k_2,m_2). It turns out that a special case of equation (A.5) has been considered by Wersinger *et al.*[5] who studied numerically the evolution of an undamped wave coupled bilinearly to two damped waves:

$$\frac{\partial C_1}{\partial t} = \gamma_1 C_1 + MC_2C_3e^{-i\delta t} \qquad (A.6a)$$

$$\frac{\partial C_{2,3}}{\partial t} = \gamma_{2,3}C_{2,3} - MC_1C^*_{2,3}e^{i\delta t} \qquad (A.6b)$$

For $\gamma_2 = \gamma_3$ and $\Gamma \equiv |\gamma_2|/\gamma_1$ they found that C_1 undergoes a period doubling cascade to chaos as Γ is increased. They also showed that the computed Poincaré section can be reduced to a unimodal map.

We propose that the chaotic behavior in our system is due to a similar coupling, with the unstable helical density wave coupling to pairs of damped waves. The simplest model is again that of three coupled waves; a possible set of the three "most important"[6] modes follows. The obvious choice for the unstable mode is the traveling helical density wave (A.3) with m = 1. The

relationship between the wave vector of this unstable wave, which we denote k_u, and the applied fields E_0 and B_0 is derived by Hurwitz and McWhorter.[2] The $m = 1$ mode is theoretically the first one to become unstable; it is also the only unstable wave observed experimentally.[2,7] Thus, in the notation (k,m) we label our first mode ($k = k_u$, $m = 1$). For the second mode we choose ($k = 0$, $m = 0$). If equation (A.3) is integrated over r and ϕ for $m \neq 0$, the result is zero, i.e., no net current flow. Since we observe oscillations (and chaos) in the total current, we must assume that an $m = 0$ mode is indeed present. We further assume that the net current flow is constant along the length of the sample, i.e., $k = 0$. Conservation of k and m therefore requires that the third mode be ($k = -k_u$, $m = -1$) – the reflection of the unstable mode. By retaining only three modes, we reduce our model [an infinite set of coupled differential equations of the form (A.5)] to a set of three coupled ordinary differential equations. Following the notation of equation (A.5) these are:

$$\frac{\partial C_{k_u,1}}{\partial t} = M_{k_u,1}C_{k_u,1} + M'_{\ 0,-k_u\ ;\ 0,-1}C_{0,0}C^*_{-k_u,-1} \tag{A.7a}$$

$$\frac{\partial C_{0,0}}{\partial t} = M_{0,0}C_{0,0} + M'_{\ k_u,-k_u\ ;\ 1,-1}C_{k_u,1}C_{-k_u,-1} \tag{A.7b}$$

$$\frac{\partial C_{-k_u,-1}}{\partial t} = M_{-k_u,-1}C_{-k_u,-1} + M'_{\ 0,k_u\ ;\ 0,1}C_{0,0}C^*_{k_u,1} \tag{A.7c}$$

We note that both the ($k = 0$, $m = 0$) and ($k = -k_u$, $m = -1$) modes are damped,[2] consistent with the model of Wersinger, *et al*. However, we also

note that our model is still based on conjecture; numerical solutions of analytic models derived from equations (A.1) are necessary to determine whether or not a nonlinear coupling of these modes will result in transitions to chaos similar to those observed experimentally.

Studying the bilinear coupling of one unstable wave and two damped waves, Wersinger, *et al.* observed a period doubling transition to chaos. However, they did not report any quasiperiodic transitions to chaos. As we have observed such transitions experimentally, we consider here two possible models which could result in a quasiperiodic transition to chaos. First, a second mode could become unstable. However, if we have two unstable modes, and the current carrying ($k = 0$, $m = 0$) mode as well, then conservation of k and m requires that at least five modes[8] be present for all the modes to be nonlinearly coupled (still assuming only bilinear coupling). The linear model of Hurwitz and McWhorter suggests that the initial instability would be the instability of lowest frequency. That is, if an additional mode became unstable at the onset of quasiperiodicity, it would have a higher frequency than the first unstable mode. This is in contrast to experimental observations (see Chapters III and IV).

The second possibility[9] is that the imaginary part of the constant $M'_{k_u,-k_u;\,1,-1}$ of equation (A.7b) becomes negative above some threshold of the applied fields. This would also result in quasiperiodicity. In this case, the second frequency to emerge could be lower than the first, consistent with experimental observations. Again, however, we note that numerical solutions

are necessary to determine which (if any) of these wave-wave interactions will show behavior similar to that observed experimentally.

References. Appendix A

1. M. Glicksman, Phys. Rev. **124**, 1655 (1961).

2. C. E. Hurwitz and A. L. McWhorter, Phys. Rev. **134**, A1033 (1964).

3. F. C. Hoh and B. Lehnert, Phys. Rev. Lett. **7**, 75 (1961).

4. for example, R. Z. Sagdeev and A. A. Galeev, *Nonlinear Plasma Theory* (Benjamin, New York, 1969).

5. J.-M. Wersinger, J. M. Finn, and E. Ott, Phys. Fluids **23**, 1142 (1980).

6. The method of keeping only the most important modes, known as the Galerkin approximation, is also used in deriving the Lorenz equations from the Navier-Stokes equation. See, for example, A. J. Lichtenberg and M. A. Lieberman, *Regular and Stochastic Motion* (Springer Verlag, New York, 1983), p. 443.

7. T. Misawa and T. Yamada, Jpn. J. Appl. Phys. **2**, 19 (1963).

8. The five modes are: $(k_u, 1)$, $(k_{\text{unstable mode \#2}}, m_2)$, $(-k_u, -1)$, $(-k_{\text{unstable mode \#2}}, -m_2)$, and (0,0).

9. Wim van Saarloos, private communication.

APPENDIX B. COMPUTER PROGRAMS

Program 1. Data Collection Program.

This program collects a time series of data from channel 00 of a Data Translation DT3382 A/D module. The data is initially stored in random access memory and subsequently transferred to a Winchester disk. Up to 98044 data points may be collected in a single sweep, with a maximum sampling rate of 240 kHz. This program is written in Fortran IV and runs on an LSI-11/23 computer. It must be linked with Data Translation's CPLIB and ADAC's ADLIB subroutine packages prior to execution.

```
C THIS PROGRAM TAKES A TIME SERIES FROM CHANNEL 00 OF
C THE DT3382 A/D BOARD,
C PLOTS A RETURN MAP OF THE DATA ON A TEK 611 STORAGE SCOPE,
C AND STORES THE DATA ON HARD DISKS USING CPLIB DISK ROUTINES.
C THE SIGNAL TO SAMPLE MUST GO INTO EXT TRIG L INPUT OF THE DT3382
C IT MAY BE SUPPLIED EXTERNALLY OR WITH THE KWV11-C CLOCK BOARD
C THIS PROGRAM DOES NOT PUT THE CPU IN COMA MODE BEFORE TAKING
C DATA AND CAN TAKE UP TO 98044 DATA POINTS
C THE LINE TIME CLOCK MUST BE ON FOR THIS PROGRAM TO WORK
C THIS PROGRAM WAS WRITTEN BY GLENN HELD ** 2/17/84
    DIMENSION ICHAN(256),IDATA(2048),IFILE(3)
    VIRTUAL DATA(24576)
    REAL*8 DATA
    REAL*4 SIZE
    INTEGER*4 NMIN,NMAX
    WRITE (7,103)
103  FORMAT(1X,'SIZE (F12.0)')
    READ (7,105) SIZE
105  FORMAT (F12.0)
    DO 10 I=1,256
 10  ICHAN(I)=0
    IGAIN=-1
```

```
      MODE='EP'
      CALL DFCHZA(256,ICHAN,IGAIN,MODE)
      WRITE (7,15)
      READ (7,25) IU
      IU= -1*IU
      IF (IU.EQ.0) GO TO 20
      CALL CLOCKW(1,1,IU,0,,"170420,"440)
      DO 94 J=1,5000
   94 CONTINUE
   20 CALL RSXVZA(SIZE,DATA)
      CALL WAITZA
      CALL CLOSZA
      CALL CLOCKW(1,0,1,0,,"170420,"440)
      IMIN=2048
      IMAX=-2048
      NMIN=0
      NMAX=0
      IEND=INT((SIZE+2047.)/2048.)
      DO 30 I=1,IEND
      RINDEX=FLOAT(I-1)*2048.+1.
      IGET=2048
      IF (I.EQ.IEND) IGET=INT(SIZE-2048.*FLOAT(I-1))
      CALL GETMXV(IGET,RINDEX,DATA,IDATA)
      DO 30 I1=1,IGET
      IF (IDATA(I1).GT.IMAX) NMAX=0
      IF (IDATA(I1).LT.IMIN) NMIN=0
      IF (IDATA(I1).GT.IMAX) IMAX=IDATA(I1)
      IF (IDATA(I1).LT.IMIN) IMIN=IDATA(I1)
      IF (IDATA(I1).EQ.IMAX) NMAX=NMAX+1
      IF (IDATA(I1).EQ.IMIN) NMIN=NMIN+1
      IF (I1.EQ.IGET) GO TO 30
      CALL DAOUTP(2,IDATA(I1))
      CALL DAOUTP(1,IDATA(I1+1))
      ISL=ISLEEP(0,0,0,1)
   30 CONTINUE
      WRITE (7,35) IMAX,NMAX
      WRITE (7,45) IMIN,NMIN
      WRITE (7,55)
      READ (7,65) IFILE(1),IFILE(2),IFILE(3)
      NBLKS=8*INT((SIZE+2047.)/2048.)
      CALL DFOPEN('DP1',IFILE,NBLKS,IFCHAN,NAVAIL)
      IF (NAVAIL.EQ.NBLKS) GO TO 50
      WRITE (7,17)
   17 FORMAT (1X,'DUPLICATED FILENAME OR INSUFFICIENT SPACE')
      GO TO 999
   50 DO 40 I=1,IEND
      RINDEX=2048.*FLOAT(I-1)+1.
      IGET=2048
      IF (I.EQ.IEND) IGET=INT(SIZE-2048.*FLOAT(I-1))
      CALL GETMXV(IGET,RINDEX,DATA,IDATA)
      IF (IGET.EQ.2048) GO TO 210
      DO 200 IZ=IGET+1,2048
  200 IDATA(IZ)=0
```

```
210 CALL WMBLK(IFCHAN,8*I-7,8,IDATA)
    CALL DFWAIT(IFCHAN)
 40 CONTINUE
    CALL DFCLOS(IFCHAN,1)
999 CALL EXIT
 15 FORMAT(1X,'NUMBER OF US BETWEEN SAMPLES (I6) - 0 FOR EXT TRIG')
 25 FORMAT(I6)
 35 FORMAT(1X,'IMAX= ',I7,3X,'NMAX= ',I7)
 45 FORMAT(1X,'IMIN= ',I7,3X,'NMIN= ',I7)
 55 FORMAT (1X,'NAME OF DATAFILE (6 CHARACTERS)')
 65 FORMAT (3A2)
 75 FORMAT (I7)
    END
```

Program 2. Direct to Disk Data Collection Program.

This program collects a time series of data from channel 00 of a Data Translation DT3382 A/D module. The data is transferred directly from the A/D converter to a Winchester disk. The maximum sampling rate is 67 kHz and the amount of data collected in a single sweep is limited only by available disk space. This program is written in Fortran IV and runs on an LSI-11/23 computer. It must be linked with Data Translation's CPLIB and ADAC's ADLIB subroutine packages prior to execution.

```
C THIS PROGRAM TAKES A TIME SERIES FROM CHANNEL 00
C OF THE DT3382 A/D BOARD,
C TRANSFERS THE DATA DIRECTLY TO A HARD DISK, AND
C THEN PLOTS A RETURN MAP OF THE DATA ON A TEK 611 STORAGE SCOPE.
C THE SIGNAL TO SAMPLE MUST GO INTO EXT TRIG L INPUT OF THE DT3382
C IT MAY BE SUPPLIED EXTERNALLY OR WITH THE KWV11-C CLOCK BOARD
C THIS PROGRAM DOES NOT PUT THE CPU IN COMA MODE BEFORE TAKING
C DATA. THE LINE TIME CLOCK MUST BE ON FOR THIS PROGRAM TO WORK
C THIS PROGRAM WAS WRITTEN BY GLENN HELD ** 2/17/84
    DIMENSION ICHAN(256),IDATA(2048),IFILE(3)
    REAL*4 SIZE
    INTEGER*4 NMIN,NMAX
    WRITE (7,103)
103  FORMAT(1X,'NUMBER OF BLOCKS (256 DATA PTS/BLOCK -- I8)')
    READ (7,105) NBLKS
105  FORMAT (I8)
    DO 10 I=1,256
 10  ICHAN(I)=0
    IGAIN=-1
    MODE='EP'
    CALL DFCHZA(256,ICHAN,IGAIN,MODE)
    WRITE (7,55)
    READ (7,65) IFILE(1),IFILE(2),IFILE(3)
    CALL DFOPEN('DP1',IFILE,NBLKS,IFCHAN,NAVAIL)
    IF (NAVAIL.EQ.NBLKS) GO TO 200
    WRITE(7,205)
205 FORMAT (1X,'DUPLICATED FILENAME OF INSUFFICIENT SPACE ON DISK')
    GO TO 999
200 WRITE (7,15)
```

```
      READ (7,25) IU
      IU= -1*IU
      IF (IU.EQ.0) GO TO 20
      CALL CLOCKW(1,1,IU,0,,"170420,"440)
      DO 94 J=1,5000
   94 CONTINUE
   20 CALL RDSKZA(NBLKS,IFCHAN)
      CALL CLOCKW(1,0,1,0,,"170420,"440)
      CALL DFCLOS(IFCHAN,1)
      CALL DFOPEN('DP1',IFILE,NBLKS,IFCHAN,NAVAIL)
      IMIN=2048
      IMAX=-2048
      NMIN=0
      NMAX=0
      ICNT=1
      IBLKS=8
  310 IF (NBLKS.LE.IBLKS) IBLKS=NBLKS
      CALL RMBLK(IFCHAN,ICNT,IBLKS,IDATA)
      CALL DFWAIT(IFCHAN)
      JBLKS=256*IBLKS
      DO 30 I1=1,JBLKS
      IF (IDATA(I1).GT.IMAX) NMAX=0
      IF (IDATA(I1).LT.IMIN) NMIN=0
      IF (IDATA(I1).GT.IMAX) IMAX=IDATA(I1)
      IF (IDATA(I1).LT.IMIN) IMIN=IDATA(I1)
      IF (IDATA(I1).EQ.IMAX) NMAX=NMAX+1
      IF (IDATA(I1).EQ.IMIN) NMIN=NMIN+1
      IF (I1.EQ.JBLKS) GO TO 30
      CALL DAOUTP(2,IDATA(I1))
      CALL DAOUTP(1,IDATA(I1+1))
      ISL=ISLEEP(0,0,0,1)
   30 CONTINUE
      ICNT=ICNT+8
      NBLKS=NBLKS-8
      IF (NBLKS.LE.0) GO TO 300
      GO TO 310
  300 WRITE (7,35) IMAX,NMAX
      WRITE (7,45) IMIN,NMIN
      WRITE (7,215)
  215 FORMAT (1X,'SAVE DATAFILE? (I8) -- 0 = NO')
      READ (7,225) ISAVE
  225 FORMAT (I8)
      CALL DFCLOS(IFCHAN,ISAVE)
  999 CALL EXIT
   15 FORMAT(1X,'NUMBER OF US BETWEEN SAMPLES (I6) - 0 FOR EXT TRIG')
   25 FORMAT(I6)
   35 FORMAT(1X,'IMAX=  ',I7,3X,'NMAX=  ',I7)
   45 FORMAT(1X,'IMIN=  ',I7,3X,'NMIN=  ',I7)
   55 FORMAT (1X,'NAME OF DATAFILE (6 CHARACTERS)')
   65 FORMAT (3A2)
   75 FORMAT (I7)
      END
```

Program 3. Fractal Dimension Calculation Program.

This program calculates fractal dimensions from a time series using the algorithm discussed in Chapter III. It is written in Fortran-77 and has been run on a Sun computer. Prior to execution it must be linked with the graphics subroutine package included as Program 6 of this appendix.

```
      PROGRAM NEWDIM2
C THIS PROGRAM CALCULATES THE POINTWISE FRACTAL
C DIMENSION AVERAGED OVER MULTIPLE POINTS
C OF DATA TAKEN FROM A DATAFILE
C THIS PROGRAM WAS WRITTEN BY GLENN HELD * 9/20/84
      DIMENSION CORR(24)
      INTEGER*2 IDATA(500000)
      CHARACTER*11 FILENAME,FNAME
      IBIG=0
      DO 120 I=1,24
  120 CORR(I)=0.
   30 WRITE (6,15)
      READ (5,25) ISCALE, N
      WRITE(6,105)
      READ (5,115) IRUD
      WRITE (6,405)
      READ (6,415) IEMIN,IEMAX,IESTEP
      WRITE(6,"(1X,'FILENAME? (10 CHARACTERS)')")
      READ (5,"(A)") FILENAME
      OPEN (UNIT=2,FILE=FILENAME,STATUS='OLD',ACCESS='DIRECT'
     x,RECL=2,FORM='UNFORMATTED')
      REWIND 2
      DO 300 I=1,N+IEMAX
  300 READ (2,REC=I) IDATA(I)
      NMAXX=-5000
      NMINN=5000
      DO 10 I=1,N
      IF (IDATA(I).GT.NMAXX) NMAXX=IDATA(I)
      IF (IDATA(I).LT.NMINN) NMINN=IDATA(I)
   10 CONTINUE
      XSCALE=FLOAT(ISCALE)/FLOAT(NMAXX-NMINN)
      DO 12 I=1,N
   12 IDATA(I)=INT(XSCALE*FLOAT(IDATA(I)))
      FNAME(1:7)=FILENAME(1:7)
      FNAME(8:11)='.PLT'
      CALL FRAME(24,10,FNAME)
```

```
      CALL SCALE(1.,24.,13.,3.)
      CALL PEN(1)
      DO 370 IDIM=IEMIN,IEMAX,IESTEP
      ICHOICE=1
      DO 100 I3=1,IRUD
  350 I1=IABS(IRAND(ICHOICE))/10000
      ICHOICE=ICHOICE+1
      IF (I1.GT.N) GO TO 350
      DO 110 I2=1,N
      RIR=0
      DO 200 IMID=1,IDIM
  200 RIR=RIR+(FLOAT(IDATA(I1+IMID-1)-IDATA(I2+IMID-1)))**2
      IF (RIR.LT.1.42) RIR=1.42
      IR=INT(TLOG(RIR)+.5)
      IF (IR.GT.24) GO TO 130
      CORR(IR)=CORR(IR)+1.
      GO TO 110
  130 IBIG=IBIG+1
  110 CONTINUE
  100 CONTINUE
      DO 150 I=24,2,-1
      DO 160 I1=1,I-1
  160 CORR(I)=CORR(I)+CORR(I1)
  150 CONTINUE
      RMINN=AINT(TLOG(CORR(1)))
      RMAXX=AINT(TLOG(CORR(24))+1)
      DO 180 I=1,24
      CALL PLOT(TLOG(CORR(I)),FLOAT(I)/2)
      CALL PENUP()
  180 CONTINUE
      WRITE(6,45) IBIG
      WRITE(6,55) RMINN,RMAXX
      DO 360 ICLEAR=1,24
  360  CORR(ICLEAR)=0.
      IBIG=0
  370  CONTINUE
   15  FORMAT(1X,'ISCALE, N (2I6)')
   25  FORMAT (2I6)
   35  FORMAT (1X,I5)
   45  FORMAT(1X,'IBIG=',I8)
   55  FORMAT(1X,'MIN=',E10.4,'MAX=',E10.4)
   85  FORMAT(I7)
  105  FORMAT (1X,'NUMBER OF SPHERES (I5)')
  115  FORMAT (I5)
  405  FORMAT (1X,'EMBED DIM:  MIN,MAX,STEP (3I5)')
  415  FORMAT (3I5)
      CLOSE (UNIT=2)
      STOP
      END
      FUNCTION TLOG(X)
      TLOG=ALOG(X)/0.693147
      RETURN
      END
```

Program 4. Correlation Function Calculations of Data Collected with a DT3382 A/D Module.

This program collects data from channels 00 and 01 of a Data Translation A/D module. The maximum sampling rate is 120 kHz. The correlation function of this data, as defined in Chapter IV, is then calculated. This program is written in Fortran IV and runs on an LSI-11/23 computer. It must be linked with Data Translation's CPLIB and ADAC's ADLIB subroutine packages prior to execution.

```
C THIS PROGRAM TAKES DATA FROM TWO CHANNELS
C OF A DT3382 A/D MODULE AND DETERMINES THE
C CORRELATION OF THESE TWO CHANNELS USING A VARIABLE NUMBER
C OF POINTS.
C PRIOR TO EACH CALCULATION OF THE CORRELATION FUNCTION THE TWO
C SETS OF DATA ARE EACH ADJUSTED SO THAT THEY EACH HAVE A MEAN OF
C ZERO AND A DIFFERENCE OF 4096 BETWEEN THEIR MINIMUM AND
C MAXIMUM VALUES
      DIMENSION ICHAN(2),IDATA(2048)
      VIRTUAL DATA(24576)
      REAL*8 DATA
      REAL*4 SIZE,RNUM
      DOUBLE PRECISION CORR,CMEAN1,CMEAN2,D1,D2,RMEAN1,RMEAN2
     X,SCALE1,SCALE2
C TAKE THE DATA
      SIZE=98044.
      ICHAN(1)=0
      ICHAN(2)=1
      IGAIN= -1
      MODE = 'ES'
C MODE='ES' SO BOTH CHANNELS SAMPLED AFTER EACH TRIGGER PULSE
      CALL DFCHZA(2,ICHAN,IGAIN,MODE)
      WRITE(7,25)
      READ (5,35) IU
      IU= -1*IU
      IF (IU.EQ.0) GO TO 20
      CALL CLOCKW(1,1,IU,0,,"170420,"440)
      DO 30 J=1,5000
   30 CONTINUE
```

```
 20  CALL RSXVZA(SIZE,DATA)
     CALL WAITZA
     CALL CLOSZA
     CALL CLOCKW(1,0,1,0,,"170420,"440)
C CALCULATE THE CORRELATION FUNCTION
 40  WRITE(7,45)
     READ (5,55) RNUM
     CORR=0.
     CMEAN1=0.
     CMEAN2=0.
     IF (RNUM.EQ.0.) GO TO 999
     RNUM=2.*RNUM
     CALL RSCALE
    1(DATA,IDATA,1.,RNUM,IMIN1,IMAX1,IMIN2,IMAX2,RMEAN1,RMEAN2)
     WRITE(6,75) IMIN1,IMAX1,IMIN2,IMAX2
     SCALE1=4096./(DBLE(FLOAT(IMAX1-IMIN1)))
     SCALE2=4096./(DBLE(FLOAT(IMAX2-IMIN2)))
     IEND=INT((RNUM+2047.)/2048.)
     DO 50 I=1,IEND
     RINDEX=FLOAT(I-1)*2048.+1.
     IGET=2048
     IF (I.EQ.IEND) IGET=INT(RNUM-2048.*FLOAT(I-1))
     CALL GETMXV(IGET,RINDEX,DATA,IDATA)
     DO 50 I1=1,IGET,2
     D1=(DBLE(FLOAT(IDATA(I1)))-RMEAN1)*SCALE1
     D2=(DBLE(FLOAT(IDATA(I1+1)))-RMEAN2)*SCALE2
     CORR=CORR+(D1*D2)
     CMEAN1=CMEAN1+D1
 50  CMEAN2=CMEAN2+D2
     CORR=DSQRT((2./RNUM)*DABS(CORR))
     CMEAN1=(2./RNUM)*CMEAN1
     CMEAN2=(2./RNUM)*CMEAN2
     WRITE(6,65) RNUM/2.,CORR,CMEAN1,CMEAN2
     GO TO 40
999  CALL EXIT
 25  FORMAT (1X,'NUMBER OF US BETWEEN SAMPLES (I6) -- 0 FOR EXT TRIG')
 35  FORMAT (I6)
 45  FORMAT (1X,'NUMBER OF PAIRS TO BE USED IN CALCULATION (F12.0)')
 55  FORMAT (F12.0)
 65  FORMAT (1X,'RNUM =  ',F12.0 / 1X,'CORR =  ',E15.6/
    11X, 'CMEAN1 =  ',E15.6 / 1X,'CMEAN2 =  ',E15.6)
 75  FORMAT (1X,'IMIN1 =  ',I8,'    IMAX1 =  ',I8/
    11X,'IMIN2 =  ',I8,'    IMAX2 =  ',I8)
     END


C THIS SUBROUTINE DETERMINES THE MEANS, MINIMUM AND MAXIMUM VALUES
C OF TWO INTERLACED STREAMS OF DATA
C CALL RSCALE(SDATA,ISDATA,RI1,RI2,IMIN1,IMAX1,IMIN2,IMAX2,RMEAN1,RMEAN2)
C WHERE SDATA IS A VIRTUAL ARRAY CONTAINING DATA SET #1 IN THE ODD
C INDICES AND DATA SET #2 IN THE EVEN INDICES
C ISDATA IS TRANSFERED ONLY TO SAVE SPACE (IE, AN IDENTICAL ARRAY
C EXISTS IN THE MAIN PROGRAM)
```

```
C RI1 IS THE MINIMUM ENTRY IN SDATA TO BE CONSIDERED
C RI2 IS THE MAXIMUM ENTRY IN SDATA TO BE CONSIDERED
C NOTE THAT RI1-RI2+1 REFERS TO THE TOTAL NUMBER OF POINTS
C CONSIDERED AND NOT THE TOTAL NUMBER OF PAIRS OF POINTS
C ACCORDINGLY RI1 MUST BE ODD AND RI2 MUST BE EVEN
C IMIN1 AND IMIN2 ARE THE MINIMUM VALUES OF THE TWO DATA SETS
C BETWEEN RI1 AND RI2.  IMAX1 AND IMAX2 ARE THE MAXIMUM VALUES
C RMEAN1 AND RMEAN2 ARE THE MEAN VALUES OF THE TWO DATA SETS
      SUBROUTINE RSCALE
     1(SDATA,ISDATA,RI1,RI2,IMIN1,IMAX1,IMIN2,IMAX2,RMEAN1,RMEAN2)
      VIRTUAL SDATA(24576)
      REAL*8 SDATA
      DIMENSION ISDATA(2048)
      REAL*4 RI1,RI2
      INTEGER IMAX1,IMAX2,IMIN1,IMIN2
      DOUBLE PRECISION RMEAN1,RMEAN2
      REAL*4 RNUM
      RNUM=RI2-RI1+1.
      RMEAN1=0.
      RMEAN2=0.
      IMIN1=4096
      IMIN2=4096
      IMAX1=-4096
      IMAX2=-4096
      IEND=INT((RNUM+2047.)/2048.)
      DO 10 I=1,IEND
      RINDEX=FLOAT(I-1)*2048. + RI1
      IGET=2048
      IF (I.EQ.IEND) IGET=INT(RI2-2048.*FLOAT(I-1))
      CALL GETMXV(IGET,RINDEX,SDATA,ISDATA)
      DO 10 I1=1,IGET,2
      IF (ISDATA(I1).GT.IMAX1) IMAX1=ISDATA(I1)
      IF (ISDATA(I1).LT.IMIN1) IMIN1=ISDATA(I1)
      IF (ISDATA(I1+1).GT.IMAX2) IMAX2=ISDATA(I1+1)
      IF (ISDATA(I1+1).LT.IMIN2) IMIN2=ISDATA(I1+1)
      RMEAN1=RMEAN1+DBLE(FLOAT(ISDATA(I1)))
      RMEAN2=RMEAN2+DBLE(FLOAT(ISDATA(I1+1)))
   10 CONTINUE
      RMEAN1=(2./DBLE(RNUM))*RMEAN1
      RMEAN2=(2./DBLE(RNUM))*RMEAN2
      RETURN
      END
```

Program 5. Correlation Function Calculations of Data Collected with a Tek 468 Oscilloscope.

This program collects data from channels 1 and 2 of a Tektronix 468 digital storage oscilloscope. The maximum sampling rate is 12.5 MHz. The correlation function of this data, as defined in Chapter IV, is then calculated. This program is written in Fortran IV and runs on an LSI-11/23 computer. It must be linked with Data Translation's CPLIB and National Instrument's GPIB subroutine packages prior to execution.

```
C THIS PROGRAM TAKES DATA FROM TWO CHANNELS AND DETERMINES THE
C CORRELATION OF THESE TWO CHANNELS USING A VARIABLE NUMBER
C OF POINTS.  DATA IS TAKEN WITH TEK 468 STORAGE OSCILLOSCOPE
C CONNECTED TO THE LSI-11 VIA IEEE-488 CONNECTOR
C WITH ALL VARIABLES REAL (VS. DOUBLE PRECISION) THE PROGRAM WILL
C RUN OK FOR UP TO APPROX. 200 BLOCKS OF 256 PAIRS OF DATA POINTS
C PRIOR TO EACH CALCULATION OF THE CORRELATION FUNCTION THE TWO
C SETS OF DATA ARE EACH ADJUSTED SO THAT THEY EACH HAVE A MEAN OF
C ZERO AND A DIFFERENCE OF 256 BETWEEN THEIR MINIMUM AND
C MAXIMUM VALUES
      DIMENSION IOUT1(256), IOUT2(256)
C TAKE THE DATA
      WRITE(7,5)
      READ (7,15) JNUM
      CALL DFOPEN('DD','GHPR1',JNUM,ICHAN1,NAVAIL)
      IF (JNUM.NE.NAVAIL) GO TO 999
      CALL DFOPEN('DD','GHPR2',JNUM,ICHAN2,NAVAIL)
      IF (JNUM.NE.NAVAIL) GO TO 999
      DO 10 I=1,JNUM
      CALL GDATA(IOUT1,IOUT2)
      CALL WBLK(ICHAN1,I,IOUT1)
      CALL DFWAIT(ICHAN1)
      CALL WBLK(ICHAN2,I,IOUT2)
      CALL DFWAIT(ICHAN2)
 10   CONTINUE
C CALCULATE THE CORRELATION FUNCTION
 40   WRITE(7,45)
      READ (5,55) NMIN,NMAX
      CORR=0.
```

```
      CMEAN1=0.
      CMEAN2=0.
      IF (NMAX.EQ.0) GO TO 999
      CALL RSCALE
     1(NMIN,NMAX,IMIN1,IMAX1,IMIN2,IMAX2,RMEAN1,RMEAN2,ICHAN1,ICHAN2)
      WRITE(6,75) IMIN1,IMAX1,IMIN2,IMAX2
      SCALE1=256./(FLOAT(IMAX1-IMIN1))
      SCALE2=256./(FLOAT(IMAX2-IMIN2))
      DO 50 I1=NMIN,NMAX
      CALL RBLK(ICHAN1,I1,IOUT1)
      CALL DFWAIT(ICHAN1)
      CALL RBLK(ICHAN2,I1,IOUT2)
      CALL DFWAIT(ICHAN2)
      DO 50 I2=1,256
      D1=(FLOAT(IOUT1(I2))-RMEAN1)*SCALE1
      D2=(FLOAT(IOUT2(I2))-RMEAN2)*SCALE2
      CORR=CORR+(D1*D2)
      CMEAN1=CMEAN1+D1
   50 CMEAN2=CMEAN2+D2
      RNUM=FLOAT(NMAX-NMIN+1)*256.
      CORR=SQRT((1./RNUM)*ABS(CORR))
      CMEAN1=(1./RNUM)*CMEAN1
      CMEAN2=(1./RNUM)*CMEAN2
      WRITE(6,65) RNUM,CORR,CMEAN1,CMEAN2
      GO TO 40
  999 CALL DFCLOS(ICHAN1,0)
      CALL DFCLOS(ICHAN2,0)
      CALL EXIT
    5 FORMAT (1X,'NUMBER OF BLOCKS OF DATA (256 PAIRS/BLOCK (I6)')
   15 FORMAT (I6)
   45 FORMAT (1X,'NMIN,NMAX (2I6)')
   55 FORMAT (2I6)
   65 FORMAT (1X,'RNUM =  ',F12.0 / 1X,'CORR =  ',E15.6/
     11X, 'CMEAN1 =  ',E15.6 / 1X,'CMEAN2 =  ',E15.6)
   75 FORMAT (1X,'IMIN1 =  ',I8,'    IMAX1 =  ',I8/
     11X,'IMIN2 =  ',I8,'    IMAX2 =  ',I8)
      END

C THIS SUBROUTINE DETERMINES THE MEANS, MINIMUM AND MAXIMUM VALUES
C CALL RSCALE(ISDATA,I1,I2,IMIN1,IMAX1,IMIN2,IMAX2,RMEAN1,RMEAN2)
C WHERE ISDATA IS A VIRTUAL (NX2) ARRAY CONTAINING DATA SET #1
C IN ROW #1 AND DATA SET #2 IN ROW #2
C I1 IS THE MINIMUM ENTRY IN ISDATA TO BE CONSIDERED
C I2 IS THE MAXIMUM ENTRY IN ISDATA TO BE CONSIDERED
C IMIN1 AND IMIN2 ARE THE MINIMUM VALUES OF THE TWO DATA SETS
C BETWEEN RI1 AND RI2.  IMAX1 AND IMAX2 ARE THE MAXIMUM VALUES
C RMEAN1 AND RMEAN2 ARE THE MEAN VALUES OF THE TWO DATA SETS
      SUBROUTINE RSCALE
     1(I1,I2,IMIN1,IMAX1,IMIN2,IMAX2,RMEAN1,RMEAN2,ICHAN1,ICHAN2)
      DIMENSION IDATA1(256),IDATA2(256)
      RNUM=FLOAT(I2-I1+1)*256.
      RMEAN1=0.
      RMEAN2=0.
```

```
      IMIN1=4096
      IMIN2=4096
      IMAX1=-4096
      IMAX2=-4096
      DO 10 I=I1,I2
      CALL RBLK(ICHAN1,I,IDATA1)
      CALL DFWAIT(ICHAN1)
      CALL RBLK(ICHAN2,I,IDATA2)
      CALL DFWAIT(ICHAN2)
      DO 10 IT=1,256
      IF (IDATA1(IT).GT.IMAX1) IMAX1=IDATA1(IT)
      IF (IDATA1(IT).LT.IMIN1) IMIN1=IDATA1(IT)
      IF (IDATA2(IT).GT.IMAX2) IMAX2=IDATA2(IT)
      IF (IDATA2(IT).LT.IMIN2) IMIN2=IDATA2(IT)
      RMEAN1=RMEAN1+FLOAT(IDATA1(IT))
      RMEAN2=RMEAN2+FLOAT(IDATA2(IT))
   10 CONTINUE
      RMEAN1=RMEAN1/RNUM
      RMEAN2=RMEAN2/RNUM
      RETURN
      END

      SUBROUTINE GDATA(IOUT1,IOUT2)
      DIMENSION IOUT1(256),IOUT2(256)
      DIMENSION IOUT(256,2)
      LOGICAL*1 INPUT(2048)
      J=GPIB(12,0)
      J=IBUP(1,2,INPUT,2000)
      T1=SECNDS(0.)
  400 DELTA=SECNDS(T1)
      IF (DELTA.LT.1.) GO TO 400
      IND=1
      DO 210 IT=1,J
      IF (INPUT(IT).NE.'%') GO TO 210
      DO 230 IT1=3,258
      IO=INPUT(IT1+IT)
      IF (IO.LT.0) IO=256+IO
      IOUT(IT1-2,IND)=IO
  230 CONTINUE
      IND=IND+1
      IT=IT+259
  210 CONTINUE
      J=GPIB(12,10)
      DO 250 I=1,256
      IOUT1(I)=IOUT(I,1)
      IOUT2(I)=IOUT(I,2)
  250 CONTINUE
      RETURN
      END
```

Program 6. Graphics Subroutine Package

This is a collection of Fortran callable subroutines which convert simple scaling and plotting commands into HP Graphics Language (HPGL). These subroutines are called by Program 3 of this appendix (which calculates fractal dimensions). These subroutines are written in C and have been run on a Sun computer.

```
#include <stdio.h>
/* this is a collection of fortran callable graphics routines for use with */
/* HP 7475A plotter using HPGL */
/*these routines are written in C*/
/* call these routines using the fortran "call" command*/
/* these routines were written by Glenn Held  4/9/84  */

/* frame (x,y,fname) */
/* int x,y;  */
/* draw a frame with x tickmarks on the x-axis & y tickmarks on the y-axis */
/* char fname[50] */
/* fname is the name of the file that all HPGL commands are stored in */
/* until another frame command is issued */
/* this command also issues an xon/xoff protocol command to the plotter*/

/* scale (xmin,xmax,ymin,ymax)  */
/* float xmin,xmax,ymin,ymax;  */
/* sets the minimum and maximum values for each axis of the graph  */
/* this subroutine must be called prior to calling the plot subroutine */

/* plot(x,y)  */
/* float x,y;  */
/* moves the pen over to point (x,y) and lowers the pen (if it isn't */
/* already lowered) */
/* the x & y scales must be set by the scale subroutine prior to calling plot */

/* penup() */
/* raise the plotter pen */
```

```
/* pen(number) */
/* int number; */
/* selects the pen in bin "number" (for number = 1 to 6) */
/* number=0 replaces the pen in use  */


static char filename[50];


frame_(px,py,tempname,length)
int *px,*py,length;
char tempname[];
  {
    double xt,yt,xi,yi;
    int x,y;
    FILE *fp,*fopen();
    x= *px;
    y= *py;
    strcpy(filename,tempname);
    fp=fopen(filename,"a");
    if (fp === NULL)  {
         printf ("can't open file0);
         return (-1);
         }
    fprintf(fp,".I81;;17:0N;19:0);
    fprintf(fp,"in; ip 210,596,10290,7796;0);
    fprintf(fp,"sc 0,100,0,100; sp 1; pu; pa 0,0;0);
    fprintf(fp,"pd; pa 0,100; pa 100,100; pa 100,0; pa 0,0; pu;0);
    fprintf (fp,"tl 1;0);
    xi = 100./(double) x;
    yi = 100./(double) y;
    for (xt=xi; xt<100.; xt += xi)
       fprintf(fp,"pa %16.4f, 0; xt;0,xt);
    for (yt=yi; yt<100.; yt += yi)
       fprintf(fp,"pa 0, %16.4f; yt;0,yt);
    fclose(fp);
    return(0);
  }
scale_(pxmin,pxmax,pymin,pymax)
float *pxmin,*pxmax,*pymin,*pymax;
  {
    float xmin,xmax,ymin,ymax;
    FILE *fp, *fopen();
    xmin= *pxmin;
    xmax= *pxmax;
```

```
    ymin= *pymin;
    ymax= *pymax;
    fp=fopen(filename,"a");
    if (fp == NULL)  {
        printf ("can't open file 0);
        return (-1);
        }
    fprintf(fp,"sc %12.0f,%12.0f,%12.0f,%12.0f;0,xmin,xmax,ymin,ymax);
    fclose(fp);
  }
pen_(pnum)
int *pnum;
  {
    FILE *fp,*fopen();
    int num;
    num= *pnum;
    fp=fopen (filename,"a");
    if (fp == NULL)  {
        printf ("can't open file 0);
        return (-1);
        }
    fprintf(fp,"sp %d;0,num);
    fclose(fp);
  }
penup_() {
    FILE *fp,*fopen();
    fp=fopen (filename,"a");
    if (fp == NULL)  {
        printf ("can't open file 0);
        return (-1);
        }
    fprintf (fp,"pu;0);
    fclose(fp);
  }
plot_(px,py)
float *px,*py;
  {
    FILE *fp,*fopen();
    float x,y;
    x= *px;
    y= *py;
    fp=fopen (filename,"a");
    if (fp == NULL)  {
        printf ("can't open file 0);
        return (-1);
```

```
        }
    fprintf(fp,"pa %16.4f,%16.4f; pd;0,x,y);
    fclose(fp);
}
```

ACKNOWLEDGEMENTS

I am grateful to Professor Carson Jeffries for his advice, support, and encouragement throughout the course of this work. His experimental expertise and physical insight have been a source of inspiration for me.

I would like to thank William Hansen and Professor Eugene Haller for providing me with the Germanium crystals used in these experiments. I would also like to thank Professor Haller for helpful discussions on the physics of Germanium. I am grateful to Paul Luke and Nancy Haegel for their extensive advice and assistance in preparing the samples used in this work.

I have benefited from many helpful discussions with past and present members of Professor Jeffries research group, including Paul Bryant, Dr. James Crutchfield, Dr. James Culbertson, Dr. John Furneaux, Dr. Elga Pakulis, Dr. Jose Perez, Dr. James Testa, Robert van Buskirk, and last, but certainly not least, Professor Robert Westervelt. I also wish to thank Dr. J. Doyne Farmer, Dr. James Hanson, Professor Allan Kaufman, Professor Michael Lieberman, Dr. Robert McMurray, Roger Tobin, Dr. Wim van Saarloos, and Dr. Priya Vashishta for many helpful suggestions and discussions.

Finally, I am grateful to the Materials Science Division of the U. S. Department of Energy for supporting this research under Contract No. DE-AC03-76SF00098.

LAWRENCE BERKELEY LABORATORY
TECHNICAL INFORMATION DEPARTMENT
UNIVERSITY OF CALIFORNIA
BERKELEY, CALIFORNIA 94720